The Pennsylvania State University

The J. Jeffrey and Ann Marie Fox Graduate School

LARGE-EDDY SIMULATION OF JET NOISE USING THE ENERGY CASCADE

A Thesis in

Aerospace Engineering

by

Dana Mikkelsen

Submitted in Partial Fulfillment
of the Requirements
for the Degree of

Master of Science

December 2024

The thesis of Dana Mikkelsen was reviewed and approved by the following:

Philip J. Morris
Boeing/A.D. Welliver Professor Emeritus of Aerospace Engineering
Thesis Advisor

Daning Huang
Assistant Professor of Aerospace Engineering

Eric Greenwood
Assistant Professor of Aerospace Engineering

Amy R. Pritchett
Professor of Aerospace Engineering
Head of the Department of Aerospace Engineering

ABSTRACT

The use of large-eddy simulation (LES) techniques for jet noise problems has been a subject of discussion for many years due to their ability to capture the turbulent structures necessary for acoustic analysis. Historically, LES has been prohibitively computationally expensive for use beyond simple configurations; however, recent strides made in the area as well as the introduction of GPU-accelerated solvers, which improve the turn-around for these intensive calculations, are bringing the use of LES into the realm of studies in industry.

This thesis investigates a method of grounding LES grid generation in the turbulent energy spectrum to eliminate the trial-and-error approach to the construction of a high-fidelity model. In this method, the mixing, Taylor microscale, and Kolmogorov microscale lengths are extracted from a Reynolds-averaged Navier Stokes (RANS) simulation conducted on an arbitrarily fine grid. These length scales are then used to calculate the grid size necessary to resolve 80% of the total kinetic energy of a LES. The velocity and turbulence statistics obtained from the LES developed using this method show good agreement with experimental data. The acoustic data shows good agreement with experimental data as well, validating the grid developed using the energy spectrum.

This thesis then suggests a method of normalizing acoustic data from two nozzles to an equal thrust basis to make such comparisons more practical for industry application. Using the same grid, a second RANS and LES calculation are run at a slightly lower nozzle pressure ratio (NPR) to simulate losses in the nozzle that could result from a change in geometry. The thrust values for both the original nozzle and the second nozzle are calculated from the RANS runs. Then, it is determined at which velocity the second simulation should be run to match the thrust value of the first simulation. Acoustic data are obtained from the second LES and adjusted using an acoustic scaling law to recover the decrease in noise levels due to the 'losses' in the nozzle. The adjusted acoustic data shows good agreement with the original acoustic data from the first LES, suggesting the validity of this method.

TABLE OF CONTENTS

LIST OF FIGURES

LIST OF TABLES

ACKNOWLEDGEMENTS

The completion of this work would not have been possible without the help, assistance, and support of those around me. First and foremost, I'd like to thank my advisor, Dr. Philip Morris, for introducing me to the world of aeroacoustics. Having known nothing about it before beginning this project, his advice and knowledge was indispensable. I would also like to acknowledge the other faculty and staff here at Penn State who supported this project: Dr. Daning Huang, who provided critical assistance with coding; Kirk Heller, who was so incredibly patient with my endless need for IT support; and Dr. Eric Greenwood, who agreed to be part of my committee.

I would also like to extend my sincere gratitude to the assistance I received from those at Gulfstream Aerospace Corporation. Dr. Joe Gavin and Sandra Gavin were under no obligation to help me but went above and beyond and took time out of their busy schedules to do so anyway. This thesis would not have been completed without the critical resources and assistance they provided. I would also like to thank Nicholas Ward and the rest of the Acoustics & Vibrations Group at Gulfstream for taking me on and giving me a place in which to begin my career in industry.

I would be remiss if I did not thank my friends from the University of Central Florida who have supported me throughout this endeavor, as well as the new friends I made here in State College through the Penn State Swing Dance Club and Centre Social Dance.

Finally, I am so incredibly grateful for the support of my parents, Robert and Diane Mikkelsen, and my sibling, Sevan Mikkelsen, who listened to me complain about this project every step of the way. And, of course, my cat: Mr. Ghost, who kept me company through remote work and classes.

This material is based upon work supported by the Federal Aviation Administration under Award No. 59E. Any opinions, findings, and conclusions or recommendations expressed in this publication are those of the author and do not necessarily reflect the views of the Federal Aviation Administration.

Chapter 1

Jet Noise Survey

In recent years, numerical studies have risen to stand on equal footing with experimental and analytical studies in the field of jet aeroacoustics. Large-Eddy Simulation (LES), which has historically been prohibitively computationally expensive for use beyond simple configurations, has undergone development in the last decade that has brought it into the realm of studies in industry, but some challenges remain. Developing a high-fidelity grid for an LES can be a time-consuming trial-and-error process. Commercially licensed computational fluid dynamics (CFD) software is easier to implement than the use of in-house codes but is more limited in its application to specific problems such as jet noise. Furthermore, most jet noise studies conducted using Large-Eddy Simulation look only at noise prediction and do not consider the effect on thrust. The aim of this thesis is to eliminate the trial-and-error method of grid generation, investigate the viability of the commercial software package STAR-CCM+ for jet noise predictions, and develop a method of thrust normalization for use in industry applications.

This first chapter reviews the history of the discipline of jet noise, from the earliest studies in the 1950s to the most recent studies. Section 1.1 gives a background on jet noise and why its reduction is important. Section 1.2 discusses Lighthill's acoustic analogy, which is foundational to the study of aerodynamically generated sound. Section 1.3 reviews experimental studies, while Section 1.4 does the same for analytical noise predictions. Section 1.5 gives a brief introduction to numerical studies, which are discussed further in Chapter 2. Section 1.6 explains the objectives of this study, and Section 1.7 provides an overview of the remainder of this thesis.

1.1 Jet Noise Background

Most commercial aircraft today are powered by jet engines, which can operate safely at high speeds and generate enough thrust to lift a large-capacity cabin. The predecessor to the modern turbofan engine, the turbojet, was invented in the 1930s independently by Frank Whittle in England and Hans von Ohain in Germany. The German fighter jet Heinkel He 178 was the first turbojet-powered aircraft to fly in 1939 but was quickly followed by the Italian Caproni Campini N.1, the British Gloster E.28/39, and the American Bell XP-59A. The first production turbojet aircraft flew in 1944.

Ten years after the first flight of the Heinkel He 178, the first commercial jet airliner, the British de Havilland Comet, flew in 1949 and entered service with the BOAC in 1952. By this time, experimental studies were already being conducted to investigate the properties of jet noise [1,2] and how it could be reduced [3]. The first mathematical prediction of jet noise was also published in 1952 by Lighthill [4], which became the foundational theoretical approach for the work that followed. Due to its significance, Lighthill's approach is discussed in section 1.1.

Noise reduction of jet engines continues to be an important area of research today in both military and civilian capacities. On the military side, the noise levels on the decks of aircraft carriers are so high as to cause hearing loss to the personnel who work there, even with hearing protection [5,6]. Work is being done to mitigate the noise from military aircraft jets using technologies such as chevrons, corrugated seals, and fluid injection [7]. On the civilian side, aircraft must meet the noise limit requirements set by the International Civil Aviation Organization. These limits, or 'stages,' have been in effect since the early 1970s. In 2006, stage 4 limits were introduced that required a 10 decibel (dB) decrease from stage 3 limits [8]. These noise limits were updated again in 2017, with stage 5 limits requiring a reduction of an additional 7 dB.

Aircraft manufacturers are constantly seeking new methods of noise reduction to meet these increasingly stringent standards. This is complicated by the fact that noise prediction is difficult and has historically been too computationally intensive to achieve any degree of accuracy in simulations,

especially not on the scale required for industry. Recent innovations in large eddy simulation (LES), discussed in chapter 2, are making it more possible to use these tools than ever before. This work focuses primarily on the use of LES to model jet exhaust noise.

1.2 Lighthill's Acoustic Analogy

Until Lighthill's 1952 work, most studies on sound generation focused on that generated by vibrating bodies [9], in which boundary conditions could be matched using the linearized momentum equation. The studies performed on aerodynamically generated sound were concerned with frequencies in the flow rather than the intensity of the sound produced.

Lighthill found that aerodynamically generated sound is caused by turbulence which is, by definition, nonlinear. Therefore, the previously developed concepts of linear acoustics cannot be applied to free-flowing fluid at high Reynolds' numbers. Lighthill's analogy does not make any assumptions about compressibility effects in the region of turbulence and couples the acoustic wave motion outside of the flow to the large velocity fluctuations inside the flow as shown in Figure 1.1.

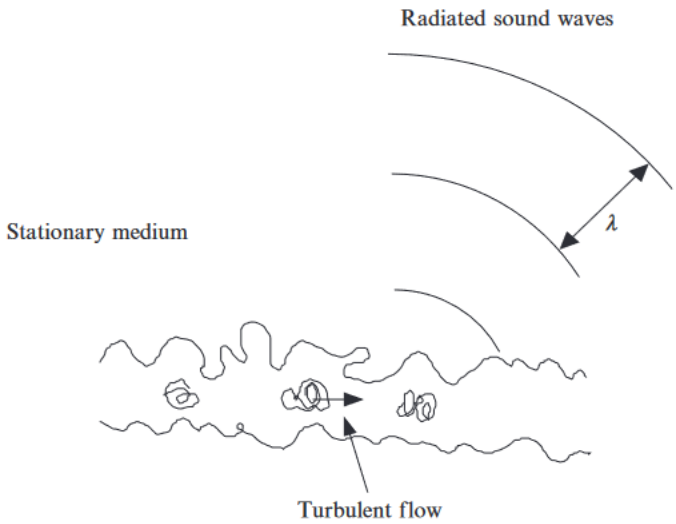

Figure 1.1: Sound radiation from a region of turbulent flow [10]

Lighthill placed a region of turbulence in an expanse of still, quiescent air with density ρ_∞ and ambient sound speed a_∞. Taking the time derivative of the continuity equation

$$\frac{\partial}{\partial t}\left(\frac{\partial \rho}{\partial t}+\frac{\partial(\rho u_i)}{\partial x_i}\right)=0 \tag{1.1}$$

and subtracting the divergence of the momentum equation

$$\frac{\partial}{\partial x_i}\left(\frac{\partial(\rho u_i)}{\partial t}+\frac{\partial(\rho u_i u_j+p_{ij})}{\partial x_j}\right)=0 \tag{1.2}$$

gives

$$\frac{\partial^2 \rho}{\partial t^2}=\frac{\partial^2\left(\rho u_i u_j+p_{ij}\right)}{\partial x_i\,\partial x_j} \tag{1.3}$$

where $p_{ij}=(p-p_\infty)\delta_{ij}-\sigma_{ij}$. The continuity and momentum equations are further discussed in chapter 3: equations (3.1) and (3.2), respectively.

Defining ρ' as the density perturbation $(\rho-\rho_\infty)$ and subtracting $\partial^2(\rho' a_\infty^2)/\partial x_i^2$ from both sides of Eqn. (1.3) gives a wave equation in the form

$$\frac{\partial^2 \rho'}{\partial t^2}-a_\infty^2\frac{\partial^2 \rho'}{\partial x_i^2}=\frac{\partial^2 T_{ij}}{\partial x_i \partial x_j} \tag{1.4}$$

where T_{ij} is the Lighthill stress tensor

$$T_{ij}=\rho u_i u_j+(p-p_\infty)-(\rho-\rho_\infty)a_\infty^2\delta_{ij}-\sigma_{ij} \tag{1.5}$$

with δ_{ij} being the Kroneker delta and σ_{ij} the viscous stress tensor.

Equation (1.4) is known as Lighthill's wave equation, or simply Lighthill's equation [4]. It is an exact rearrangement of the conservation of mass and momentum equations. The left side describes the propagation of an acoustic wave in a uniform medium, while the right side contains the equivalent

source terms that generate acoustic waves. This source term is called a quadrupole due to the double-divergence $\left(\partial^2/\,\partial x_i\,\partial x_j\right)$, and T_{ij} is the quadrupole strength. The formal solution to Eqn. (1.4) is obtained using a free space Green's function and can be written as

$$\rho'(\boldsymbol{x},t) = \frac{1}{4\pi a_\infty^2}\int_{jet}\frac{\partial^2 T_{ij}}{\partial y_i\,\partial y_j}(\boldsymbol{y}, t-|\boldsymbol{x}-\boldsymbol{y}|/a_\infty)d\boldsymbol{y} \tag{1.6}$$

where $\boldsymbol{x}$ and $\boldsymbol{y}$ are vectors and $t-|\boldsymbol{x}-\boldsymbol{y}|/a_\infty$ is the retarded time.

Equation (1.6) is an integral equation solving for the density perturbation ρ'. It states that the noise generated by free-flowing fluid is analogous to the stress generated by the motion of the fluid in a medium with properties ρ_∞ and a_∞.

1.2.1 Acoustic Intensity

After the exact equation (1.4) has been derived, one can make some assumptions about Lighthill's stress tensor T_{ij}, which Crighton [11] lays out in his 1975 work. The first assumption is that viscous contributions to T_{ij} within the flow region are small and can be neglected. Second, if temperatures in the flow are similar to those outside the flow, then the sound speed in the flow (a) will not be much different than that of the surrounding medium (a_∞). If these two things are true, then the only significant contribution to T_{ij} is due to the fluctuating Reynolds stresses $\left(\rho u_i u_j\right)$. Furthermore, if the flow Mach number is low, then ρ can be replaced by the mean density ρ_∞ with a relative error of order M^2. Therefore, for subsonic cold air jets, T_{ij} can be approximated by

$$T_{ij} \approx \rho_\infty u_i u_j. \tag{1.7}$$

The radiated density field for a single eddy can then be found for a nearly incompressible turbulent flow. For the case of a compact eddy with eddy length l and eddy Mach number $M \ll 1$, and taking Eqn. (1.7) to be approximately equivalent to $\rho_\infty u^2$, the radiated density field is

$$\rho(x,t) \sim a_\infty^{-4} x^{-1} \left(\frac{u}{l}\right)^2 \rho_\infty u^2 l^3 \sim \rho_\infty \left(\frac{l}{x}\right) M^4 \tag{1.8}$$

and the predicted total sound radiated by the eddy is

$$P \sim \rho_\infty u^3 l^2 M^5. \tag{1.9}$$

This theory can be applied directly to jet flow. Substituting the mean exit velocity U_j for eddy velocity u, the nozzle diameter D_j for eddy length l, and using $M = U_j/a_\infty$, Eqn. (1.9) becomes

$$P \sim \frac{\rho_\infty U_j^8 D_j^2}{a_\infty}, \tag{1.10}$$

which is the Lighthill eighth power law for total radiated power. The U_j^8 relation provided a path to designing quieter engines by focusing on reducing U_j using methods such as different nozzle configurations, mixed flow nozzles, and turbofan engines, some of which will be discussed in the following section.

1.3 Experimental Studies

The first experimental studies conducted in the 1950s were focused on the noise radiated from a cold, single-stream jet analogous to the turbojet popular at the time. These early studies confirmed Lighthill's theory that high-frequency sound radiation was caused by a lateral acoustic quadrupole and established that the radiated noise was a function of polar angle θ, jet velocity U_j, and temperature T. Westley and Lilley [1] showed the axial jet velocity had its major decrease in the region 4-25 diameters (D) downstream and that the velocity gradient $\partial U/\partial r$ also decreased with the axial distance downstream of the nozzle exit. Lassiter and Hubbard [2] found that high-frequency noise sources existed near the nozzle exit and low-frequency components emanated from further downstream. It was determined that the distribution of intensity and frequency in the sound was highly directional,

with minimum intensity along the jet axis and maximum intensity between 15^0 and 45^0 from the jet downstream axis. Low-frequency noise was dominant along the jet axis, while higher-frequency noise became more dominant at observers closer to 90^0. Lassiter and Hubbard also found that an increase in turbulence resulted in a higher overall sound pressure level (OASPL) and suggested that the mixing region of the turbojet was the main source of noise.

Further investigation into jet turbulence was conducted by Laurence [12] and Davies *et al.* [13] in the late 1950s and early 1960s. Using hot wire anemometry, they took measurements of turbulence parameters such as intensity, scale, correlation, and spectra. Laurence found that near the jet nozzle, the turbulence intensity was highest at the nozzle lip line $\left(R_j/D_j = 0.5\right)$ and that for $x/D < 4$, this turbulence had a high wavenumber. The lateral and longitudinal scales of turbulence did not depend significantly on Mach number. The longitudinal scale was found to be at a maximum around 0.7 to $0.8R_j$ and increased linearly with downstream distance from the nozzle. The lateral scale was consistently less than the longitudinal scale and increased with distance from the nozzle but did not vary with radial distance from the centerline. The nature of these scales suggested the existence of streamwise-elongated "eddies" [8] that were likely induced by the nozzle geometry.

Davies *et al.* [13] aimed in their 1963 study to determine the distribution through the jet of shear, length scales, turbulence intensity, and convection velocity. In doing so, they replicated several of Laurence's tests and confirmed many of his results. Davies *et al.* determined that the integral timescale was inversely proportional to the local shear, and that the local turbulence intensity was equal to a fraction of $(\sim 1/5)$ the shear velocity U_S, where U_S was the product of the axial length scale L_x and the local shear velocity gradient $\partial u/\partial r$. They also established that kinematic similarity existed for intensity, space-scales, timescales, and spectra, which they expressed in terms of the distance from the nozzle exit and the integral timescale. These similarity relationships were well-defined for the first 6-8 diameters downstream but broke down close to the nozzle exit where the shear layer was thin.

Both Laurence and Davies *et al.* focused their efforts on axial relationships due to their more significant contribution, but in 1964, Bradshaw *et al.* [14] examined azimuthal velocity fluctuations. They found that up to an $x/D_j = 7$, the root mean square (rms) axial velocity was greater than the rms radial velocity along the centerline $(u_{rms} > v_{rms})$. Beyond $x/D_j = 7$, the radial velocity was greater than the axial velocity $(u_{rms} > v_{rms})$.

In the late 1960s and early 1970s, attention turned to the directivity of radiated sound. Lighthill initially commented on directivity in his 1954 work [15], making note of the fact almost all the sound from a jet radiated downstream and measurements taken upstream of the jet were liable to be erroneous due to the relatively small intensity. Directivity did not receive much further attention until Ffowcs Williams further described it in 1963 [16]. He extended his studies to high-speed jets, noting that an 'extremely directional field' was radiated at $\cos\theta = M^{-1}$. He claimed this directionality was due in part to waves attached to eddies which moved at half the jet exit velocity, and that acoustic power increased with velocity cubed. With an increase in velocity, the direction of peak emission was found to move toward the normal to the jet axis. Ffowcs Williams modified the far-field intensity equation to apply to the noise radiated by a high speed jet and his formula was summarized by Lush [17] as

$$I \sim \frac{\rho_m^2 U_j^8 D_j^2}{\rho_\infty a_\infty^5 R^2} \frac{D(\theta)}{(1 - M_c \cos\theta)^5} \tag{1.11}$$

where ρ_m is the density in the mixing region, ρ_∞ is the ambient density, U_j is the jet velocity, a_∞ is the ambient speed of sound, D_j is the jet diameter, and R_j is the distance from the jet to the observer. θ is the angle between the direction of emission of sound and the downstream jet axis, while the function $D(\theta)$ is the directivity of the unconvected quadrupoles and M_c is the axial velocity of convection of the quadrupoles divided by a_∞. Ffowcs Williams [16] also established that when the convection Mach number approaches unity, the $(1 - M_c \cos\theta)^{-5}$ term should be modified to $\{(1 - M_c \cos\theta)^2 + \alpha^2 M_c^2\}^{-\frac{5}{2}}$. The sound power P can be obtained from the intensity I using

$$P = 2\pi R^2 \int_0^{\pi} I(\theta) \sin\theta \, d\theta. \tag{1.12}$$

Lush [17] further investigated the effect of directivity on radiated sound, extending analysis to the velocity dependence and directivity of the intensity in one-third octave frequency bands. From this analysis, he found that for lower frequencies, the theoretical velocity dependence fit the experimental results at all observation angles. The predicted directivity matched the results at larger angles from the jet axis but fell short of the measurements along the jet axis. For higher frequencies, there was good agreement away from the jet axis but an overestimation of levels near the jet axis, especially for the velocity dependence. Lush determined that directivity became more marked as velocity increased; while the sound intensity was almost uniform at low jet velocities, at high velocities, a peak became evident around 22.5 degrees as shown in Figure 1.2. Lush also confirmed the eighth power rule at right angles to the jet and noted that the scaling of the peak frequency of radiated noise was dependent on angle: for small angles, the peak frequency stayed constant with respect to U_j, but for larger angles, the peak frequency scaled with U_j.

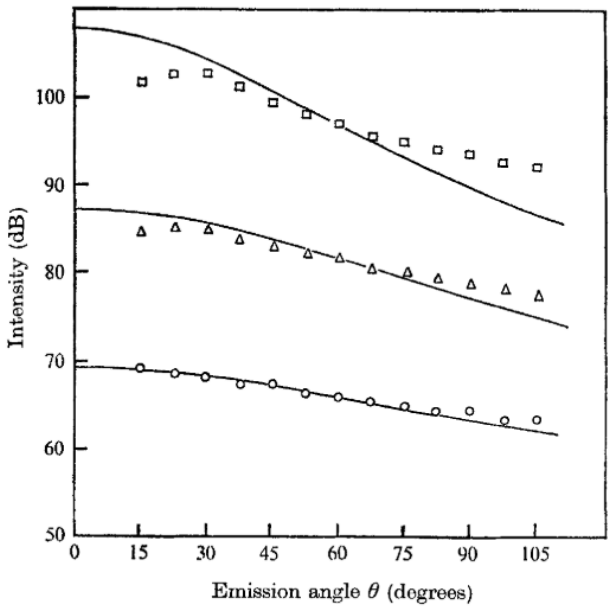

Figure 1.2: Directivities compared with theory. Jet velocities: ○, 125 m/s; Δ, 195 m/s; □, 300 m/s; —, theory [17]

Jet noise scaling was further investigated by Ahuja [18], who developed an empirical scheme used to collapse one-third octave sound pressure level (SPL) data for multiple angles and frequencies onto one curve. As shown in Figure 1.3, he found that for angles greater than 45 degrees to the jet axis, Lighthill's theory showed good agreement at all angles, especially for low frequencies. For high frequencies at small angles to the jet axis, the peaks of these spectra were found not to depend on the jet velocity at all, but could rather be predicted by Helmholtz scaling

$$f_p = \frac{0.2a_\infty}{D_j}. \tag{1.13}$$

This further confirmed Lush's findings that low angle, high frequency noise was over predicted.

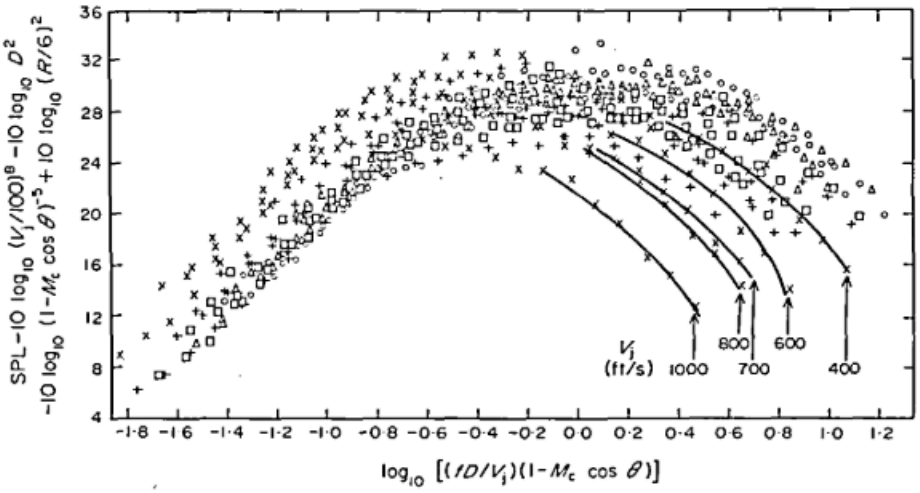

Figure 1.3: Normalized 1/3 octave SPL's against Doppler corrected Strouhal number [18]

Ahuja, like most other early experimentalists, worked with clean, unheated (cold) jets. In 1977, Tanna [19], though not the first to study heated jets, identified the effects of heating on jet noise. Systematically taking measurements from a wide range of operating conditions, he confirmed Hoch *et al.*'s 1973 observation [20] that heating the jet produced an increase in noise at low jet velocities while at high jet velocities heating the jet decreased the overall noise level. Furthermore, he found that the acoustic Mach number $Ma = U_j/a_\infty$ was the defining parameter, where heating increased sound levels below $Ma = 0.7$ and decreased sound levels above $Ma = 0.7$. The overall change in sound level was

obtained by integrating over all frequencies; lower-frequency sound, more dominant at low jet velocities, increased with heating and higher-frequency sound, more dominant at high jet velocities, decreased with heating, resulting in the observed net change.

Though supersonic aircraft have existed in some capacity since the American Bell X-1 research plane in 1947 and the Convair B-58 Hustler strategic bomber in 1956, the development of the supersonic airliner Concorde, which first flew in 1969, ignited investigation into the sound produced by these aircraft. It was a topic of high interest through the 1970s and 1980s and, with the renewed interest in commercial supersonic flight, continues to be an important area of research It was found that supersonic jet noise was comprised of three different components as shown in Figure 1.4: turbulent mixing noise [21–24], broadband shock-associated noise [25–29] and screech tones [30–35]. The turbulent mixing noise involves the same noise generation mechanism found in subsonic jets, while the broadband shock-associated noise and the screech tones both result from the shocks in the jet plume. The screech tones had discrete frequencies, while the broadband shock-associated noise was, as the name suggests, broadband. The addition of the shock noise components differentiated supersonic jet noise from subsonic jet noise. Tam [36] conducted a full review of supersonic jet noise.

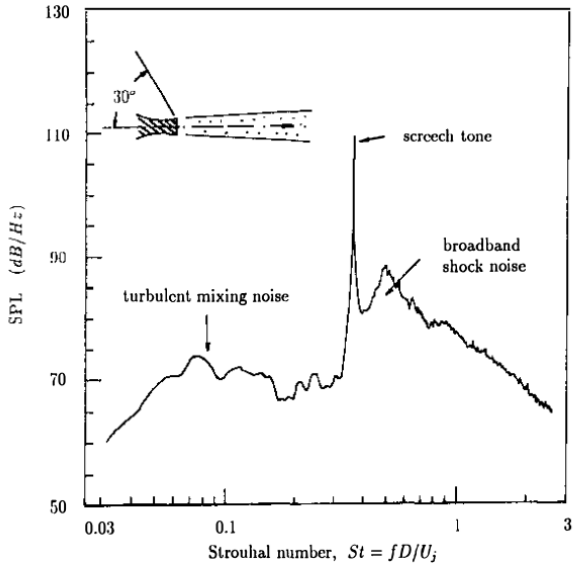

Figure 1.4: Typical far-field narrow-band supersonic jet noise spectrum [36]

In the early 2000s, improvements made in particle image velocimetry (PIV) technologies allowed researchers to take measurements over a wider range of velocities and temperatures than was possible with hot-wire anemometry. Bridges and Wernet [37] and Bridges and Brown [38] took advantage of this to provide near-field turbulence measurements. Viswanathan [39] revisited Tanna's work with heated jets in 2004 with the goal of obtaining cleaner data, as well as investigating the effect of Reynold's number and jet density. It had previously been theorized that dipole sources contributed to the jet noise, especially at high jet temperatures and low Mach numbers [40]. Viswanathan found that this 'extra hump' effect found in small nozzles, shown in Figure 1.5, was due to Reynold's number effects instead of the presence of dipoles. He estimated the critical value of Reynold's number needed to avoid these effects associated with low Reynold's number was about Re = 400,000.

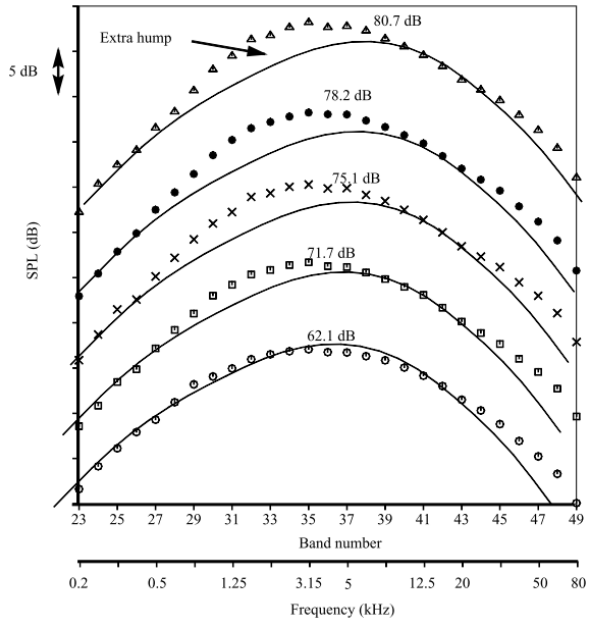

Figure 1.5: Comparison of measured spectra with fine-scale similarity spectrum. M=0.5, angle=90°, D=1.5in; ○, Tt/Ta =1.0; □,1.8; ×, 2.2; ●, 2.7; ▲, 3.2 [39]

Bridges and Wernet extended their work with turbulence measurements of hot subsonic jets in 2010 [41], when they created a catalog of both hot and cold subsonic turbulent jet flows with statistics ranging from mean velocity to space-time correlations of Reynolds stresses. After creating the PIV datasets, they compared their data with data published in the open literature and compared it to

different datasets acquired at the same flow conditions to establish uncertainties. They weighted each dataset using a data quality metric, then averaged and smoothed the data for all test entries to obtain a 'consensus' dataset for each flow case with the intention of providing data for CFD validation. Their work also demonstrated a universal scaling for the jet flow fields within the first 20 diameters, the region most relevant to aeroacoustics.

1.3.1 Jet Noise Reduction

With a firm, though ever-changing understanding of the mechanisms integral to jet noise generation, interest has always had noise reduction as its focus. Efforts have been made to reduce noise by adding chevrons [42], corrugated seals [43], and fluid injection [44] inside the nozzle with varying degrees of success. Researchers have also investigated the effect of adjusting the thickness of the nozzle lip [45] as well as noise reduction methods that don't require a change in the nozzle geometry or additional hardware [46]. Beyond the noise generated from the jet itself, the acoustic interaction between the jet flow and aircraft body [47] is also an important consideration.

1.4 Analytical Noise Prediction

From its development in 1952 until the 1970s, Lighthill's *acoustic analogy* approach dominated the analytical work surrounding jet noise. Further analytical work performed through the 1960s focused mainly on augmenting Lighthill's approach. Curle [48] extended Lighthill's theory to account for surface effects, while Ffowcs Williams [16] extended it to consider transonic and supersonic ranges of eddy convection speed. It was found that Lighthill's approach could be applied to flows beyond the initial jet noise problem, such as underwater flows relevant to ships and submarines. Crighton [11] provides a summary of these further applications as they stood in 1975.

As discussed in the previous section, it was then found in the 1970s that Lighthill's predictions were not uniformly valid. Lush [17] and Ahuja [18] found that Lighthill's theory overpredicted low-

angle, high-frequency noise spectra. This led others to consider alternate theories of sound generation and propagation. In 1960, Phillips [49] had developed a theory to describe the generation of sound by turbulence at high Mach numbers. In doing so, he expressed the governing mass and momentum equations as a moving medium wave equation with a specified source term, which is given in Eqn. (1.14).

$$\frac{D^2}{Dt^2}\log\left(\frac{p}{p_0}\right) - \frac{\partial}{\partial x_i}\left[a^2\frac{\partial}{\partial x_i}\log\left(\frac{p}{p_0}\right)\right] = \\ = \gamma\frac{\partial u_i}{\partial x_j}\frac{\partial u_j}{\partial x_i} + \gamma\frac{D}{Dt}\left(\frac{1}{c_p}\frac{DS}{Dt}\right) - \gamma\frac{\partial}{\partial x_i}\left[\frac{1}{\rho}\frac{\partial}{\partial x_j}\left(\mu\left(e_{ij} - \frac{2}{3}\theta\delta_{ij}\right)\right)\right] \tag{1.14}$$

Here, p_0 is a convenient reference pressure, a is the local speed of sound, γ is the specific heat ratio, c_p is the specific heat at constant pressure, S is entropy, μ is viscosity, e_{ij} is the rate of strain tensor, $\theta = \partial u_i / \partial x_i$ is the fluid dilation, and δ_{ij} is the Kronecker delta. Unlike Lighthill's equation, the effects of convection and variation in the local speed of sound were included in the left-hand side of the equation. Though theoretically valid, the presence of other propagation terms in the source was undesirable.

Lilley [50] also derived an inhomogeneous moving media wave equation, but his was a third-order convective wave equation for transversely sheared flow that eliminated all linear terms from the equivalent sources on the right-hand side of the equation, leaving only terms that were at least second order in the fluctuations around the mean flow. Terms that were linear in the fluctuations were retained in the propagator on the left-hand side of the equation. To simplify the algebra, he wrote the solution in terms of the log of the pressure, shown in Eqn. (1.15). Considering a parallel mean flow, $\bar{u}_i = U(x_2)\delta_{i1}$, Lilley then obtained Eqn. (1.16).

$$\Pi = \frac{1}{\gamma} ln \frac{p}{p_0} \tag{1.15}$$

$$\frac{D}{Dt}\left(\frac{D^2\Pi}{Dt^2}-\frac{\partial}{\partial x_i}a^2\frac{\partial\Pi}{\partial x_i}\right)+2\frac{\partial v_j}{\partial x_i}\frac{\partial}{\partial x_j}a^2\frac{\partial\Pi}{\partial x_i}=-\frac{\partial v_j}{\partial x_i}\frac{\partial v_k}{\partial x_j}\frac{\partial v_i}{\partial x_k}+\Psi \tag{1.16}$$

In Eqn. (1.16), Ψ represents the effects of entropy fluctuations and fluid viscosity. Lilley also derived an alternative form of Lighthill's equation (Eqn. (1.4)) that added dipoles, the result of enthalpy fluctuations due to heating, to the quadrupoles from Lighthill's original equation [50].

Morfey [51,52] then developed a semi-empirical jet noise model that took account of acoustic-mean flow interaction. This geometric acoustics model was based on Lilley's equation and showed good agreement with numerical results for both high and low frequencies but used acoustic dipoles to explain the changes in noise due to heating found by Tanna [19]. The presence of these dipoles has since been disputed by Viswanathan [39], as discussed in the previous section.

Tam and Chen [36,53] proposed a two-source noise model in the mid-1990s. Though not the first to do so, as Laufer *et al.* [54] proposed a two-source noise model in 1976. Tam and Chen's model was quite different from Laufer's model. Where Laufer suggested the two noise sources were an upstream region associated with Mach wave radiation and a zone downstream of the potential core that radiated similarly to a subsonic jet, Tam proposed that the two noise sources were associated with the fine-scale turbulence and the large turbulence structures of the jet flow as shown in Figure 1.6.

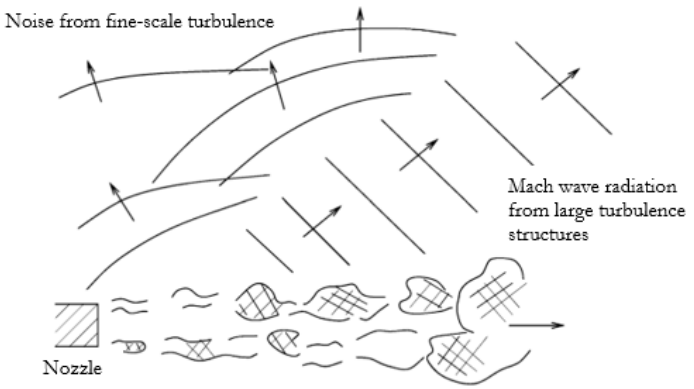

Figure 1.6: Diagram showing the large turbulence structures of a high-speed jet, the sound fields from the fine-scale turbulence, and the Mach wave radiation from the large turbulence structures [55]

Indeed, by the late 1990s, Tam *et al.* [56] found empirically two universal spectra that fit all the jet noise spectra in their database, regardless of Mach number or temperature. They labeled these two spectra the F-spectrum, or the 'peaky spectrum' and the G-spectrum, or the 'broad spectrum.' The peaky spectrum (large turbulence structure noise) fit the noise spectra measured in the downstream direction, while the broad peak spectrum (fine-scale turbulence noise) fit the noise spectra measured in the upstream and sideline directions. These two spectra are shown in Figure 1.7. A study conducted in 2008 by Tam *et al.* [55] that analyzed these spectra against four sets of experimental data concluded that the two distinct sources of jet noise were the fine-scale turbulence and the large turbulence structures of the jet flow and that, of the two, the large turbulence structures were the dominant sources of jet noise in the peak noise radiation direction. Jordan and Colonius [57] later re-framed the large turbulence structures as a dynamic model based on a wavepacket theory, which identified coherent structures in the jet and could be related directly to the far-field sound by using a Green's function or Kirchhoff's method.

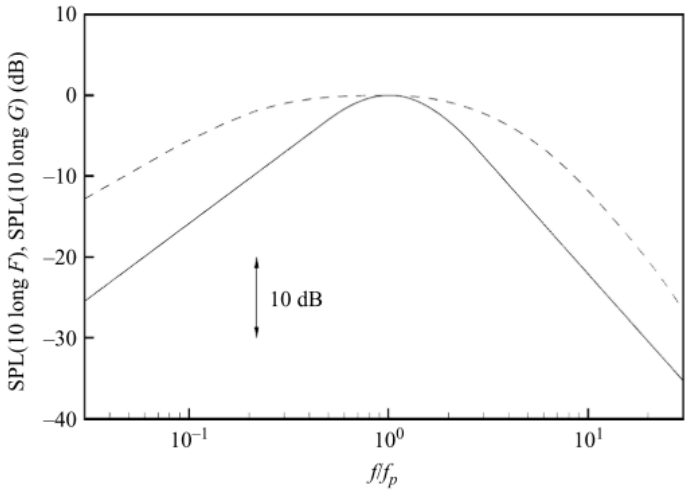

Figure 1.7: Similarity spectra for the two components of turbulent mixing noise: ———, large turbulence structure noise; – – –, fine-scale turbulence noise [55]

Tam and Auriault [58] modeled one of these two jet noise mechanisms statistically, developing a semi-empirical theory for the prediction of the spectrum, intensity, and directivity of the fine-scale turbulence noise in the sideline and upstream directions. This theory was found to be accurate over a

broad range of jet velocities and temperatures. Morris and Farassat [59] showed it to be equivalent to an acoustic analogy if one was careful about representing the source and Green's function. Goldstein [60,61] and Goldstein and Leib [62] developed a generalized acoustic analogy method that was able to predict the complete directivity of jet noise at all polar angles relative to the downstream jet axis when the true evolving mean flow was used. These acoustic analogies have been used alongside numerical methods to predict the noise produced by both cold [63,64] and hot [65] jets.

1.5 Numerical Prediction Methods

Computational approaches to jet noise prediction have been of interest to researchers since the late 1970s, when they first became viable. Numerical prediction methods are often used to augment both experimental and analytical approaches and can be loosely categorized as Reynolds-averaged Navier Stokes (RANS) methods and first-principles methods.

1.5.1 RANS-Based Noise Prediction

One of the first numerical methods, used by both industry and NASA, was the Mani, Gliebe, Balsa (MGB) jet prediction tool, introduced by Balsa *et al.* [66] in the late 1970s. It used a simplified turbulence model, based on Reichardt's theory [67], which models the flows from nozzles with arbitrary geometry by superposition of elemental round jet flows, to define length scale, time scale, and source strength parameters for a semi-empirical source model. Khavaran was the first to use a Reynolds-averaged Navier Stokes (RANS) solution to predict the mean flow in the early 1990s [68], and later reformulated the propagation and noise source models [69,70] in the late 1990s and early 2000s.

RANS calculations use an averaged mean flow to provide values for model constants, allowing for faster computation times. More detail about the formulation of RANS-based solutions can be

found in chapter 3. However, because sound is generated by the behavior of individual turbulent eddies, RANS models are limited in their ability to make accurate predictions of the radiated noise.

1.5.2 First-Principles Based Noise Prediction

First-principles based methods aim to calculate the radiated sound from flows directly. These calculations, while more accurate, are far more computationally intensive than RANS-based calculations. Before studies using this method were feasible, techniques for accurate wave capturing and the use of appropriate boundary conditions needed to be developed.

The first studies of this method didn't exist until the mid-1990s, one of which was conducted by Colonius *et al.* [71]. Colonius compared the direct calculations of the Navier-Stokes equations to the sound predicted by Lilley's analogy for two-dimensional flows. In doing so, he found the detailed form of the source term was important for accurate predictions. The first studies of a three-dimensional turbulent jet were conducted by Freund [72,73] in the early 2000s, in which the radiated sound of a Mach 0.9 jet compared well to experimental data.

Studies of first-principles methods have continued, but direct numerical calculation of three-dimensional turbulent flows remains prohibitively expensive for use beyond government and academic settings despite recent improvements in computing power. Instead, both research and industry have turned to a method that compromises between the averaging necessary for RANS and the accuracy of first-principles methods: Large-Eddy Simulation (LES), which is discussed at length in chapter 2.

1.6 Thesis Objectives

This thesis has three objectives. The first objective of this study is to ground the grid generation for Large-Eddy Simulations in the turbulent energy spectrum, thereby reducing the amount of trial-and-error inherent in the process. The second objective is to determine whether a commercial CFD package such as STAR-CCM+ by Siemens is a viable option for conducting jet noise studies by

analyzing flow data and acoustic output and comparing them to experimental studies. The third objective is to develop a process for thrust normalization so acoustic data for different nozzle configurations can be compared on an equal thrust basis.

1.7 Thesis Outline

Chapter 2 discusses the challenges of LES, the improvements that have been made in the last ten years, and some problems that still exist. The numerical methods for Reynolds-Averaged Navier Stokes and Large-Eddy Simulation are described in Chapter 3, along with the models used in STAR-CCM+ for this study. Chapter 4 describes the methods for choosing space- and time discretization based on the energy spectrum, while Chapter 5 discusses the results of a simulation conducted in STAR-CCM+. A method for normalization of acoustic data to an equal thrust basis is described in Chapter 6. Finally, Chapter 7 provides a conclusion and discusses further research that still needs to be conducted.

Chapter 2

Large-Eddy Simulation and its Challenges

The use of large-eddy simulation (LES) for jet noise predictions has been studied as a computational cost-saving alternative to first-principles methods since the late 1990s [74,75]. Unlike first-principles methods, which resolve all the scales in a flow field, or Reynolds-Averaged Navier Stokes (RANS) calculations, which model all the scales in a flow field, large-eddy simulation calculates only the large-scale components directly and models the smaller, unresolved scales. The numerical methods of LES and RANS calculations are discussed further in chapter 3.

LES is an attractive method to those studying jet noise problems due to its ability to capture the turbulent structures necessary for acoustic analysis. RANS computations are widely used in industry as a cost-effective alternative to laboratory testing but cannot resolve acoustics problems due to the inherent averaging in their formulation. Historically, despite being less computationally intensive than first-principles methods, LES simulations have been prohibitively computationally expensive for use beyond academic settings [76]; however, studies performed in the last ten years (along with improvements in high-performance computing) are bringing the use of LES into the realm of industry studies.

2.1 Recent Progress in LES Modeling

Bodony and Lele [77] conducted a survey of applications of LES for the prediction of noise from turbulent jets in 2008. At the time, they concluded the limiting factor for LES was that the initial shear layer was an order of magnitude thicker than that found experimentally. Additionally, there was no consensus on which subgrid model to use or what its effect was, and there were some questions regarding the implementation of noise prediction methods. In 2019, Brès and Lele [78] performed an additional review of the work published since the 2008 survey. They identified major improvements in

areas such as: nozzle geometry and Reynold's number; meshing and discretization; and boundary layer modeling at the nozzle exit. This chapter discusses the challenges and improvements made in LES modeling of jet noise over the last ten years including nozzle geometry, Reynold's number, spatial discretization methods, turbulence modeling, noise prediction methods, and GPU-accelerated solvers, before addressing applications of LES and some remaining challenges.

2.1.1 Nozzle Geometry and Reynolds Number

In the jet LES studies surveyed in 2008, the nozzle geometry was not simulated directly in the LES, but rather generated using a RANS calculation of the flow in the nozzle to obtain a mean flow profile [79–82]. This mean flow profile was then seeded with perturbations to initialize turbulent flow. It was argued that the differences in the turbulence caused by initializing the flow with seeded perturbations rather than modeling the nozzle geometry would minimize as the flow developed, but this was not always the case. In order to compare these simulations with measurements, arbitrary adjustments had to be made to the axial coordinate, and even then, the turbulence development and radiated noise were markedly different.

Another limitation that early LES work faced was that of reduced Reynolds number [77]. Since independence from Reynolds number in jets is reached for $Re \geq$ 100,000 or 400,000 [39,83], defined by characteristic length D_j, researchers limited Reynolds numbers to the range of 0.1 to 5×10^5. At these values, the Reynolds number largely affects the flow and radiated noise only through early shear layer development and changes in the nozzle-exit boundary layer state [78]; applications that are not as relevant when there is no geometry modeled.

Due to the importance of the nozzle-exit boundary layer, most contemporary simulations include the nozzle at the domain inlet and are performed at diameter-based Reynolds numbers of over $Re = 10^6$ [78]. Inclusion of physical geometry, however, leads to additional challenges in meshing and modeling that will be discussed in the following sections.

2.1.2 Spatial Discretization

The spatial discretization of an LES directly affects the dispersion and dissipation errors in the solution, to which aeroacoustics problems are particularly sensitive due to the need for the radiation of sound to the far field [78]. There are traditionally four different approaches to mesh generation for computational fluid dynamics: structured Cartesian, overset, multi-block structured, and generalized unstructured grids.

Hexagonal cells are most commonly used for structured Cartesian meshes, shown in Figure 2.1, in which elements are uniform and connect at the same nodes [84]. At geometrical boundaries, the cells are divided evenly into smaller cells where the boundary intersects its surfaces [85] while maintaining their hexagonal shape. Structured Cartesian meshes lend themselves to improved stability and smaller discretization errors, but they are also inflexible and it is difficult to handle complex geometries [78,84].

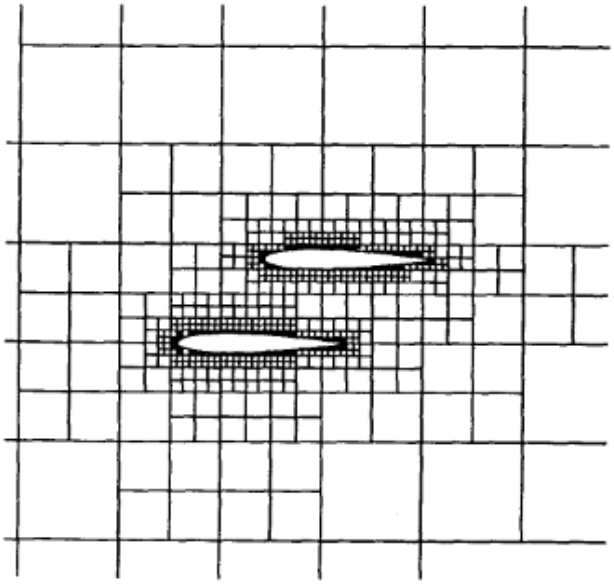

Figure 2.1: Structured Cartesian grid around an airfoil [85]

Overset grids, developed primarily by NASA and shown in Figure 2.2, resolve the problem of complex geometries by using a collection of overlapping structured grids, in which neighboring grids

are generated independently and allowed to overlap arbitrarily [86]. The surface grids around a body are developed so one or more of their boundaries are conformal to the geometry, while the far-field domain is structured with a Cartesian grid that overlaps the surface grid but does not come into contact with the surface. The overset grid method effectively deals with complex geometries and provides better accuracy and speed over unstructured grid methods but is time-consuming and expertise-dependent due to the scripting necessary to implement it.

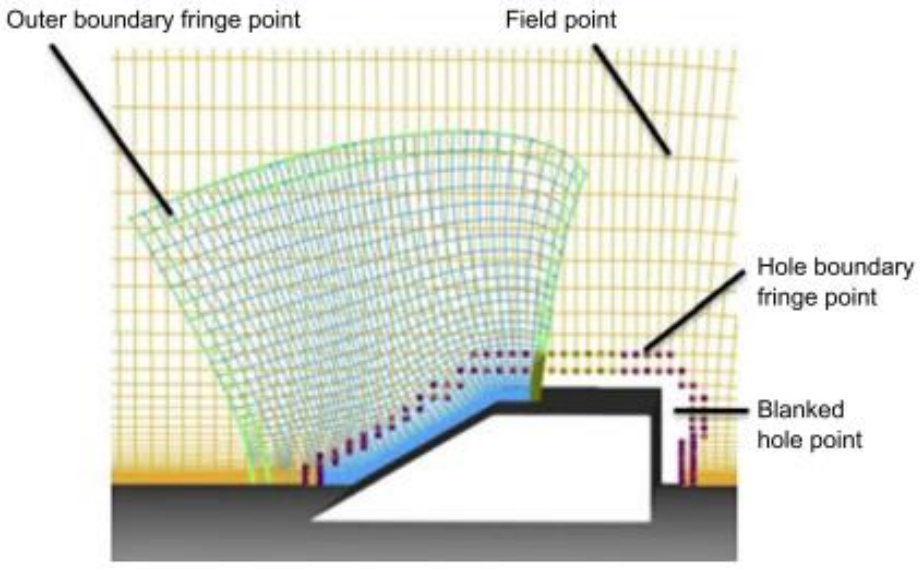

Figure 2.2: Overset volume grids [86]

Multi-block structured meshes, shown in Figure 2.3, straddle the line between strictly Cartesian structured meshes, overset grids, and fully unstructured meshes. They divide the domain into sub-regions, or blocks, in which each block contains a structured grid. These grids do not overlap like the overset grids but meet the adjacent blocks using unstructured elements such as nodes or edges of irregular connectivity, known as singularities [84]. Although multi-block structured grids provide better boundary conformity than traditional Cartesian meshes and do not require the extra post-processing necessary for overset grids, the challenge lies in where to place these singularities to best obtain multi-block decompositions that are well-suited to the problem at hand.

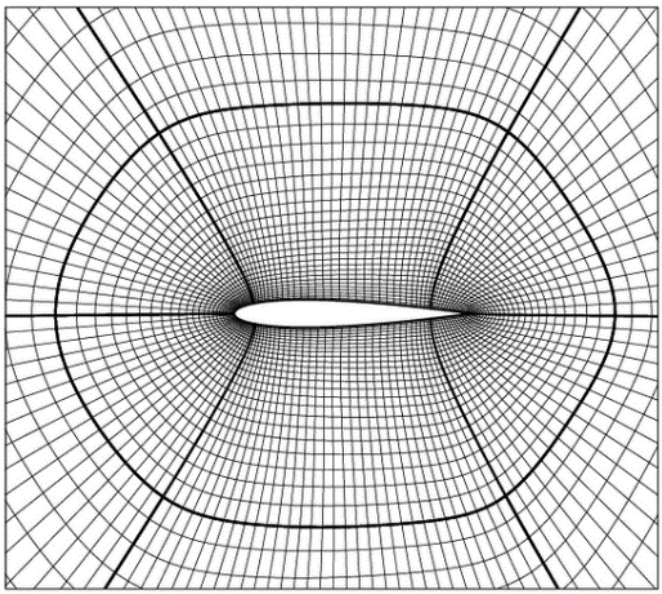

Figure 2.3: Multi-block grid around an airfoil [87]

Generalized unstructured grids, shown in Figure 2.4, can be hexahedral, tetrahedral or prismatic in nature, but the connectivity between the nodes and elements is arbitrary. This arbitrary connectivity makes it more flexible than structured grids and thus better suited to handle complex geometries within the flow domain [88]. Unstructured grids carry the inherent risk of larger discretization errors due to the increased potential for skewness, but have provided accurate jet noise predictions for simple geometries [89]. The present work proceeds with a generalized unstructured grid approach.

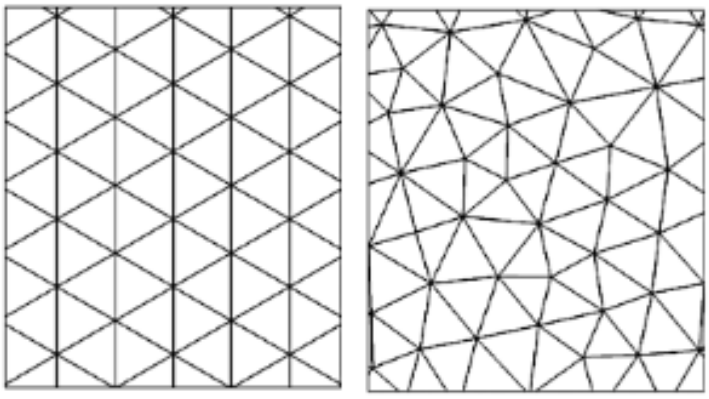

Figure 2.4: Symmetric (left) and unstructured (right) mesh fragments [88]

2.1.3 Turbulence

To obtain a well-developed LES solution, accurately capturing the thin boundary layers at the nozzle exit is crucial. Bodony and Lele [77] identified this area as one in need of improvement in their 2008 review of LES studies. The challenge in doing so with LES lies in the difficulty of resolving boundary layer turbulence for high Reynolds numbers due to the number of flow scales present and the significant cost of simulating their full range. In DES and hybrid RANS/LES methods, the flow inside the nozzle is solved using a RANS calculation. The flow then becomes turbulent in the free shear layer close to the nozzle lip [90].

Older LES studies also assumed the nozzle boundary layers to be laminar. Using a reduced Reynolds number, flows were tripped inside the nozzle boundary layer or at the nozzle inlet to induce turbulence. The initial method of tripping the flow was to impose low-level disturbances in the flow to create numerical forcing of the turbulence [91–93]. More recently, studies have tripped flows using geometrical tripping [94], in which a step or serration is added to the inside of the nozzle wall geometry; and non-geometrical tripping [95], in which prism layers are removed from the mesh at the nozzle wall without affecting the geometry itself.

Efforts are being made to improve the prediction of the turbulent flow inside the nozzle at full Reynolds numbers. Using the CharLES solver, Brès *et al.* [96] developed a method using localized adaptive mesh refinement, the application of synthetic turbulence, and wall modeling. Of these, the near-wall grid refinement had the most significant effect while the synthetic turbulence had the least. Used together, the far-field noise spectra obtained from the initially turbulent jet matched measurements within 0.5 dB where the initially laminar jets over-predicted the far-field radiated sound by as much as 3-4 dB [78].

The use of wall-modeled jet LES has only been the subject of significant research for the last decade, arising from the inclusion of the physical nozzle geometry in the domain as discussed previously. There are several different methods of wall modeling, but the wall model by Bodart and

Larsson [97] and implemented in CharLES is a wall-stress model [98] approach. It requires two grids, as shown in Figure 2.5: the unstructured LES grid that extends to the wall, and a separate structured grid at the wall that solves the RANS equations. The RANS solver takes information about the shear stress τ_w and the heat transfer q_w from the LES grid a few points away from the wall and uses them as boundary conditions for the structured grid.

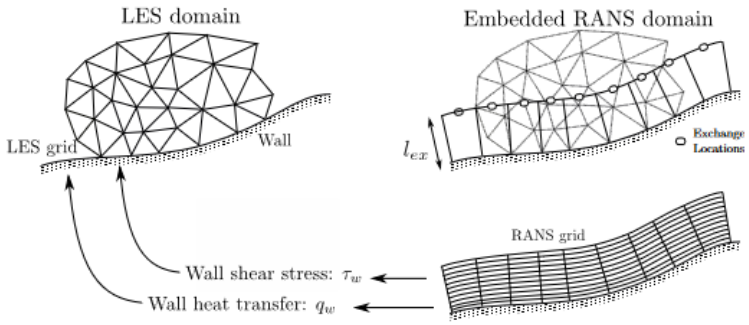

Figure 2.5: Wall-modeling procedure by Bodart and Larsson [97]

It is important to capture the boundary layer inside the nozzle because it directly affects the near-lip free shear layer. In an LES, the initial free shear layer drives the production of turbulent kinetic energy (TKE) and characterizes the flow potential core. If the boundary layer and exit flow are laminar, the shear layer quickly becomes turbulent but results in an overshoot of the streamwise root mean square (rms) velocity u' along the lipline as the flow transitions from laminar to turbulent [78]. If the exit flow is already turbulent, then TKE and u' increase steadily with distance as the shear layer grows.

The over-prediction of the far-field radiated sound for initially laminar jets occurs at high frequencies corresponding to the free shear layer dynamics and is related to the growth rate of the Kelvin-Helmholtz mode [96] which results from the velocity difference across the interface between the jet plume and the ambient medium. Proper resolution of the shear layer is therefore crucial to the fidelity of the LES model turbulence statistics and radiated noise.

2.1.4 Noise Prediction

Directly resolving the far-field radiated noise by allowing a LES to run long enough for the density fluctuations to propagate out to the far-field observers is prohibitively time- and computationally expensive, so a hybrid approach to noise prediction is generally used. The noise-producing jet turbulence is adequately resolved and the propagation of the acoustic fluctuations between the source region and the far-field observers is determined analytically. There are several different hybrid methods for acoustic wave propagation, including the Ffowcs Williams - Hawkings (FW-H) equation [99], the linearized [93] or non-linear [100] Euler equations, or the Kirchhoff method [101]. Of these, the FW-H method is the most commonly implemented and will be the method discussed going forward.

In the FW-H method, the time-varying primitive data (velocity, density, and pressure) is saved on a surface that surrounds the noise-producing turbulent flow. The far-field radiated sound is then calculated using the Green's function for a stationary or uniformly-moving ambient medium. The placement of the surface, as well as the resolution of the saved data (both temporal and spatial), must be chosen carefully. The FW-H surface cannot lie inside the unsteady flow, as the flow crossing over the surface creates spurious noise sources. At the same time, it cannot be placed too far away due to the risk of numerical error in the data by the time it reaches the surface. The full numerical formulation of the FW-H equations can be found in Chapter 3.

One problem Bodony and Lele [77] identified in their 2008 review of LES for jet noise was in how to deal with the outflow surface of a FW-H surface. If an outflow surface is included, it lies perpendicular to the flow, and thus flow crossing the surface is unavoidable. If it is not included, one risks not capturing important noise source data. The most common method of resolving this issue has been using 'endcaps,' first introduced by Shur *et al.* in 2005 [79]. In this method, the far-field pressure prediction is obtained from several different FW-H surfaces with outflow surfaces at different streamwise locations and then phase-averaged. This reduces the spurious noise effects from the

crossing of the turbulent flow over the FW-H boundary and improves far-field noise predictions [89,101] while affecting computational efficiency minimally.

2.2 GPU-Accelerated Solvers

More than any other recent development in the field of LES, the introduction of GPU-accelerated solvers makes the use of LES in industry more affordable. Where a CPU has just a few cores that can only handle a few processes at a time, a GPU is composed of hundreds of smaller, more specialized, cores that break problems into separate tasks and calculate them simultaneously. This makes it ideal for computations that can be completed in parallel processes. In one study of external aerodynamic applications, a grid sequence using the CharLES solver that took 180 hours wall-clock time on 2,000 CPUs took only 7 hours when processed on 96 GPUs [102]. The GPU-accelerated version of CharLES has since been used successfully for the large-eddy simulation of a supersonic jet [103].

2.3 Application of LES

Efficient, accurate LES is highly sought after due to its wide range of applications. LES is often used in conjunction with experiments [104,105], but is posited that a well-developed simulation could provide accurate data on a level with experimental data, eliminating the need for some expensive laboratory testing. Large eddy simulation can also provide some insights that experimental testing cannot, such as the visualization of the full three-dimensional time-resolved flow and obtaining data in places that are difficult to reach with experimental probes. Due to the improvements in LES discussed in this chapter, it is moving out of the realm of academic study and is beginning to be used for more practical industry applications.

2.4 Remaining Challenges

Of the issues Bodony and Lele [77] cited in their 2008 review, two have not been fully addressed: sub-grid scale (SGS) modeling and a limited frequency bandwidth for noise predictions.

2.4.1 Sub-Grid Scale Modeling

Sub-grid scale models such as those developed by Smagorinsky [106] and Nicoud and Ducros [107] are used to close the filtered Navier-Stokes equations used in LES and model the smallest scales of motion. These specific models are discussed in more detail in chapter 3. The combination of the treatment of these smallest scales and the numerical discretization schemes used in the simulation directly affects the amount of information that can be obtained from the results [78]. It has been found that for minimally dissipative numerical schemes, SGS modeling is required to preserve turbulence statistics [96], and that turning off the SGS model creates erroneous turbulent fluctuations and inaccurate boundary layer profiles [108]. Meanwhile, for highly dissipative numerical schemes, application of SGS modeling increases the dissipation of the smallest scales [109].

A full assessment of the pros and cons of sub-grid scale modeling has yet to be conducted, and the effect on numerical dissipation of the grid resolution in different flow regions of the simulation must also be given a closer look. This thesis concerns itself in part with the latter in chapters 4 and 5.

2.4.2 Frequency Bandwidth

Fifteen years ago, the frequency bandwidth for acoustic predictions was limited to upper Strouhal numbers of 1.5-3. This was enough to support some modeling efforts [96,110,111], but if LES is to be used for full-scale industrial applications, a larger bandwidth will be required. Progress in this area has been made with the inclusion of nozzle geometry in the domain and increased grid resolution in the shear layers and near-nozzle region [96]; however, the increased grid resolution creates a significant increase in computational cost. This increase is now being offset with the advancements in high-performance computing and GPU-accelerated solvers.

Another method of seeking a larger frequency bandwidth under consideration is to estimate the noise from unresolved scales using the information from resolved scales. As an initial step, Bodony and Lele [77] applied the general acoustic analogy approach [61] to subgrid scales [112,113]. Brès and Lele [78] suggest that these models can now be developed further with the databases of resolved LES jet noise simulations that have been created since their initial investigation in 2008. They also suggest that subfilter scale enrichment [114] and stochastic source modeling [115,116] could be used to increase the predicted noise bandwidth.

In the next chapter, the numerical methods for both RANS and LES are discussed. The models that are used in the current study, such as those for turbulence, spatial discretization, and temporal discretization, are described in detail. The full numerical formulation of the FW-H acoustic analogy for use in noise prediction is also included.

.

Chapter 3

Numerical Methods

The terms 'numerical methods' and 'computational fluid dynamics' (CFD) can be used almost interchangeably, as CFD is a subset or application of numerical methods. In its early days, CFD was viewed skeptically as it made approximations of the coupled, nonlinear partial differential equations that govern fluid motion. With the leaps and bounds made in computer power and solution accuracy over the last few decades, numerical methods now stand alongside theoretical and experimental methods in the study of fluid motion, including that of a free jet in a quiescent medium which is the current topic of study. This chapter discusses the governing Navier-Stokes equations and their discretization for both RANS (Reynolds-Averaged Navier-Stokes) and LES (Large-Eddy Simulation) methods of CFD.

3.1 Governing Equations

The computational work in the present study was conducted using STAR-CCM+, a commercial CFD package published by Siemens. Using a finite volume method, it solves the system of continuity, momentum, and energy equations

$$\frac{\partial \rho}{\partial t} + \frac{\partial \rho u_i}{\partial x_i} = 0, \tag{3.1}$$

$$\frac{\partial \rho u_i}{\partial t} + \frac{\partial \rho u_i u_j}{\partial x_j} = -\frac{\partial p}{\partial x_i} + \frac{\partial \tau_{ij}}{\partial x_j}, \tag{3.2}$$

$$\frac{\partial pe}{\partial t} + \frac{\partial (pe + p) u_i}{\partial x_i} = -\frac{\partial q_i}{\partial x_i} + \frac{\partial u_j \tau_{ij}}{\partial x_i}, \tag{3.3}$$

respectively, in conjunction with the ideal gas law

$$p = \rho RT \tag{3.4}$$

to calculate a flow field constructed from user-chosen models and their boundary conditions. Here, ρ indicates the density, u_i denotes the velocity component, p is the static pressure, q_i is the heat flux (the flow of energy per unit area per unit time), R is the specific gas constant, and T is the temperature. τ_{ij} is the viscous stress tensor, defined as

$$\tau_{ij} = 2\mu\left[\frac{1}{2}\left(\frac{\partial u_i}{\partial x_j} + \frac{\partial u_j}{\partial x_i}\right) - \frac{1}{3}\frac{\partial u_k}{\partial x_k}\delta_{ij}\right] \tag{3.5}$$

and e is the energy per unit mass, which is defined as

$$e = \frac{p}{\rho(\gamma - 1)}\frac{1}{2} + (u_i u_i). \tag{3.6}$$

3.2 RANS Numerical Methods

The mean flow field can be calculated with a RANS (Reynolds-Averaged Navier Stokes) computation. The Reynolds-Averaged Navier Stokes equations may use Favre averaging, a density-weighted averaging method, to decompose the flow variables into Favre-averaged and fluctuating parts [117,118] before substituting them into the Navier-Stokes equations [119]. These decomposed variables, with the Favre-averaged part denoted by a tilde and the fluctuating part denoted by a double prime, are as follows:

$$u_i = \widetilde{u_\iota} + u_i'' \tag{3.7}$$

$$T = \tilde{T} + T'' \tag{3.8}$$

$$e = \tilde{e} + e'' \tag{3.9}$$

$$\rho = \bar{\rho} + \rho' \tag{3.10}$$

$$p = \bar{p} + p' \tag{3.11}$$

where

$$\tilde{\phi} = \frac{1}{\Delta T}\int_{t}^{t+\Delta T} \phi dt \tag{3.12}$$

$$\bar{\phi} = \frac{1}{\bar{\rho}\Delta T}\int_{t}^{t+\Delta T} \rho\phi dt. \tag{3.13}$$

When these variables are substituted into equations (3.1)–(3.4), the following unsteady RANS equations are obtained:

$$\frac{\partial \bar{\rho}}{\partial t} + \frac{\partial \overline{\rho \widetilde{u_i}}}{\partial x_i} = 0, \tag{3.14}$$

$$\frac{\partial \bar{\rho}\widetilde{u_i}}{\partial t} + \frac{\partial \bar{\rho}\widetilde{u_i}\widetilde{u_j}}{\partial x_j} = -\frac{\partial \bar{p}}{\partial x_i} + \frac{\partial\left(\tilde{\tau}_{ij} - \overline{\rho u_i'' u_j''}\right)}{\partial x_j}, \tag{3.15}$$

$$\frac{\partial \overline{p\tilde{e}}}{\partial t} + \frac{\partial(\overline{p\tilde{e}} + \bar{p})\widetilde{u_i}}{\partial x_i} = -\frac{\partial\left(\widetilde{q_i} + \overline{\rho e'' u_i''}\right)}{\partial x_i} + \frac{\partial \widetilde{u_j}\left(\widetilde{\tau_{ij}} - \overline{\rho u_i'' u_j''}\right)}{\partial x_i} + \frac{\partial\left(\overline{u_j''\widetilde{\tau_{ij}}} - \overline{\rho u_j'' u_j'' u_i''}\right)}{\partial x_i}, \tag{3.16}$$

$$\bar{p} = \bar{\rho} R \tilde{T}. \tag{3.17}$$

The additional $\overline{\rho u_i'' u_j''}$ term in Eqn. (3.15) and Eqn. (3.16) is the Reynolds stress tensor and the term $-\overline{\rho e'' u_i''}$ in Eqn. (3.16) represents the turbulent heat flux. They are modeled respectively as

$$-\overline{\rho u_i'' u_j''} = 2\mu_t \left[\frac{1}{2}\left(\frac{\partial \widetilde{u_i}}{\partial x_j} + \frac{\partial \widetilde{u_j}}{\partial x_i}\right) - \frac{1}{3}\frac{\partial \widetilde{u_k}}{\partial x_k}\delta_{ij}\right] \tag{3.18}$$

$$-\overline{\rho e'' u_i''} = \frac{1}{\gamma - 1}\frac{\mu_t}{Pr_T}\frac{\partial \tilde{T}}{\partial x_i}, \tag{3.19}$$

where μ_t represents the turbulent viscosity and Pr_T is the turbulent Prandtl number. In STAR-CCM+, the turbulent viscosity depends on the user-chosen turbulence model and the Prandtl number is also user-specified. The additional terms $\overline{u_j'' \widetilde{\tau_{ij}}}$ and $\overline{\rho u_j'' u_j'' u_i''}$ are neglected for ideal gases.

3.2.1 Finite Volume Discretization

The finite-volume method of spatial discretization transforms the mathematical model into a system of algebraic equations. The governing equations are discretized in both space and time, and the resulting linear equations are solved with an algebraic multigrid solver.

3.2.1.1 General Transport Equation

All of the conservation relations obtained from the appropriate constitutive relations can be written in terms of a generic transport equation. By integrating the generic transport equation over a control volume V and applying Gauss's divergence theorem, the following integral form of the transport equation is obtained:

$$\frac{d}{dt}\int_V \rho\phi dV + \int_A \rho \mathbf{v}\phi \cdot d\mathbf{a} = \int_A \Gamma \nabla\phi d\mathbf{a} + \int_V S_\phi dV \tag{3.20}$$

where ϕ represents a scalar property, A is the surface area of the control volume, $d\mathbf{a}$ denotes the surface vector, and Γ is the diffusion coefficient.

Equation (3.20) has four distinct terms. The first term is the transient term, which signifies the time rate of change of the fluid property ϕ inside the control volume. The second term is the

convective flux, which expresses the net rate of decrease of the fluid property ϕ across the control volume boundaries due to convection. The third term is the diffusive flux, which corresponds to the net rate of increase of the fluid property ϕ across the control volume boundaries due to diffusion. The last term is the source term, which expresses the generation or destruction of fluid property ϕ inside the control volume. Figure 3.1 illustrates the discretization of the generic transport equation for two polyhedral cells with centroids 0 and 1 at distances $\boldsymbol{x_0}$ and $\boldsymbol{x_1}$ from the origin. The vector $\boldsymbol{ds}$ indicates the distance between the two centroids, while vectors $\boldsymbol{s_0}$ and $\boldsymbol{s_1}$ are the source terms for each cell. Vector $\boldsymbol{a_f}$ indicates the normal to face f.

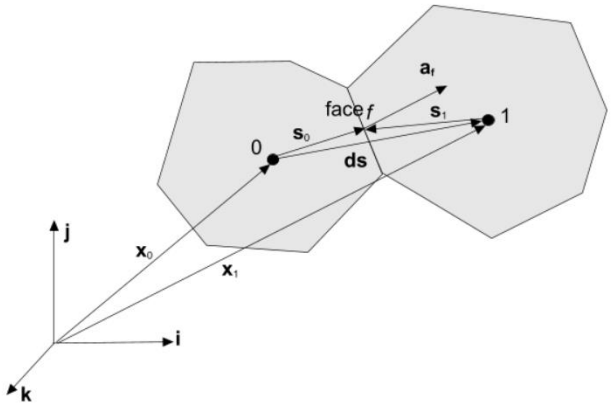

Figure 3.1: Discretization of the generic transport equation

3.2.1.2 The Normalized Variable Diagram

STAR-CCM+ uses the normalized variable diagram proposed by Leonard [120] to analyze the boundedness properties of its convective discretization schemes. Figure 3.2 shows three cells in the vicinity of a cell face f, across which velocity v_f is known. The nodal variables α_D, α_C, and α_U represent the downwind, central, and upwind positions relative to each other.

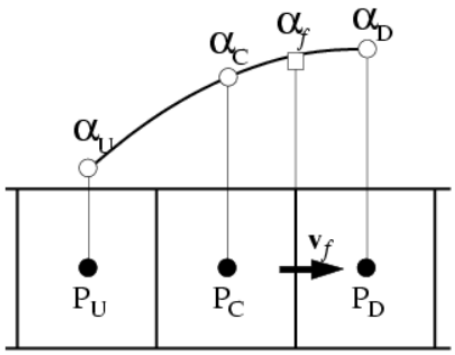

Figure 3.2: Three cells used in the normalized variable diagram

A normalized variable ζ in the vicinity of face f is defined as:

$$\zeta_f = \frac{\alpha_f - \alpha_U}{\alpha_D - \alpha_U} \tag{3.21}$$

where the normalized face value can be calculated by any differencing scheme that uses only nodal values of α at points U, C, and D. To avoid non-physical oscillations in the solution, α_f must be locally bounded between α_U and α_D, meaning $\alpha_U \leq \alpha_f \leq \alpha_D$ or $\alpha_D \leq \alpha_f \leq \alpha_U$. Therefore, when $0 \leq \zeta \leq 1$, the solution is free of oscillations. If ζ does not satisfy this criterion, the program switches to a dissipative scheme to damp the oscillations in those regions.

3.2.1.3 Second-Order Upwind Discretization Scheme

The second-order upwind differencing scheme approximates the cell face value ϕ_f in the form of a step function. Depending on the flow direction, the convective flux is computed as:

$$(\dot{m}\phi)_f = \begin{cases} \dot{m}_f \phi_{f,0} & for \ \ \dot{m}_f \geq 0 \\ \dot{m}_f \phi_{f,1} & for \ \ \dot{m}_f < 0 \end{cases} \tag{3.22}$$

where the face values $\phi_{f,0}$ and $\phi_{f,1}$ are linearly interpolated from the cell center values on each side of the face.

3.2.1.4 Steady-State Solution

For steady simulations such as a RANS calculation, the solver reduces the unsteady form of the governing equations to a steady state by using a time marching scheme in which a pseudo-transient term replaces the physical time-derivative. As the solution advances in pseudo-time, this term is driven to zero and the solution converges to steady state.

3.2.2 Turbulence Modeling

RANS computations do not directly capture the turbulence inherent in a free jet plume. Therefore, all turbulence statistics must be modeled. There are several different turbulence models available within STAR-CCM+ including Spalart-Allmaras [121], k-ε [122], k-ω [123], Reynolds Stress Transport [124], and Scale-Resolving Hybrid turbulence[125]. The present study uses the k-ω turbulence model.

3.2.2.1 k-ω Turbulence Model

The k-ω turbulence model is a two-equation model that solves transport equations for the turbulent kinetic energy k and the specific dissipation rate ω to determine the turbulent eddy viscosity, where

$$\omega \propto \epsilon/k. \tag{3.23}$$

Unlike other turbulence models such as the k-ε model which is most widely used in industry, the k-ω model can be applied to the viscous-dominated region of the boundary layer without modification. It also does not require the computation of wall distance. While the k-ε model performs well in free shear flows, it requires modifications to be used in viscous layers that the k-ω does not [126,127], making the k-ω model more suitable for modeling the wall-bounded flow inside a jet nozzle.

One challenge inherent in using the k-ω turbulence model is that the boundary layer computations are sensitive to the values of ω in the free-steam. This makes it extremely sensitive to boundary conditions for internal flows, which is a problem that does not exist for the k-ε model.

3.2.2.2 Shear Stress Transport k-ω Model

To mitigate the k-ω model's sensitivity to free-stream and inlet conditions, Menter [128] proposed including an additional non-conservative cross-diffusion term in the SST (shear-stress transport) k-ω model. When this term is included in the ω transport equation, the k-ω model has the potential to give identical results to the k-ε model while maintaining the advantage of its application to wall-bounded flows.

3.3 LES Numerical Schemes

Unlike the RANS equations, which are obtained using an averaging process, the Large-Eddy Simulation (LES) equations are obtained by a process of spatial filtering. Each solution variable ϕ, representing the pressure, velocity components, energy, etc., is decomposed into a filtered value $\tilde{\phi}$ and a sub-filtered (or subgrid) value ϕ':

$$\phi = \tilde{\phi} + \phi'. \tag{3.24}$$

The filtered value of $\phi(t, x)$ is given by

$$\tilde{\phi} = \iiint G(x - x', \Delta)\phi(t, x')dx', \tag{3.25}$$

where the filter function $G(x, \Delta)$ is characterized by a filter width $\Delta = \left(\Delta_x \Delta_y \Delta_z\right)^{1/3}$.

Spatial filtering removes the smaller eddies associated with higher frequencies, reducing the range of scales to be resolved. LES filtering can be either explicit or implicit. STAR-CCM+ uses implicit filtering, in which the computational grid determines the scales of the eddies that are filtered

out. Implicit filtering is generally less computationally expensive than explicit filtering, which applies a filter function to the discretized Navier-Stokes equations.

After inserting the decomposed solution variables into the Navier-Stokes equations, the filtered mass, momentum, and energy transport equations are identical to the URANS equations; however, the turbulent stress tensor now represents the sub-grid scale stresses. These stresses result from the interaction between the larger, resolved eddies and the smaller, unresolved eddies and are modeled as:

$$-\rho\widetilde{u_i'u_j'} = 2\mu_t\overline{S}_{ij} - \left[\frac{2\mu_t}{3}\left(\frac{\partial\widetilde{u_k}}{\partial x_k}\right) + \tilde{\rho}k\right]\delta_{ij} \tag{3.26}$$

where $\overline{S}_{ij}$ is the strain rate tensor computed from the resolved velocity field:

$$\overline{S}_{ij} = \frac{1}{2}\left(\frac{\partial\widetilde{u_i}}{\partial x_j} + \frac{\partial\widetilde{u_j}}{\partial x_i}\right). \tag{3.27}$$

The sub-grid scale turbulent viscosity μ_t is described by a subgrid scale model that accounts for the effects of smaller eddies on the resolved flow.

3.3.1 Subgrid Scale Turbulence Model

Large Eddy Simulations require closure of the filtered Navier-Stokes equations, which is achieved by modeling the sub-grid scale stress tensor. The sub-grid scale model provides a formula for μ_t in Eqn. (3.26). These models are typically based on an eddy-viscosity assumption.

The most common sub-grid scale model is Smagorinsky's model, which takes the eddy viscosity to be proportional to a characteristic turbulent velocity based on the local strain rate [106]. As such, the Smagorinsky model gives a non-zero value for the eddy viscosity everywhere a velocity gradient exists. Near a wall, however, the eddy viscosity should be zero. This means the Smagorinsky model requires a separate damping function to handle turbulent fluctuations near walls.

The sub-grid scale model used for the simulations described in this thesis is the Wall-Adapting Local-Eddy Viscosity (WALE) Subgrid Scale Model proposed by Nicoud and Ducros [107]. Unlike the Smagorinsky model, which is based on the second invariant of the symmetric part of the velocity gradient tensor, the WALE model is built on the symmetric part of the square of the velocity gradient tensor. It is written as follows:

$$\mu_t = (C_w \Delta)^2 \frac{\left(\mathcal{S}_{ij}^d \mathcal{S}_{ij}^d\right)^{3/2}}{\left(\overline{S}_{ij}^d \overline{S}_{ij}^d\right)^{5/2} + \left(\mathcal{S}_{ij}^d \mathcal{S}_{ij}^d\right)^{5/4}} \tag{3.28}$$

where $\overline{S}_{ij}$ is the deformation tensor of the resolved field, $\mathcal{S}_{ij}^d$ is the traceless symmetric part of the square of the velocity gradient tensor, Δ is the subgrid characteristic length scale, and C_w is a constant model coefficient.

Like the Smagorinsky model and other subgrid scale models, this model depends on local flow conditions and is therefore not universal; however, the WALE model is less sensitive to the value of the model coefficient than other subgrid scale models. It also does not require the additional near-wall damping. Where the Smagorinsky model gives the non-physical behavior of $\mu_t = O(1)$ at the wall, the WALE model gives the proper scaling of $\mu_t = O(y^3)$.

3.3.2 Finite Volume Discretization

As for the RANS simulation, the LES simulation uses the finite-volume discretization method. This discretization method does not change from how it is described in sections 3.2.1.1 and 3.2.1.2.

3.3.2.1 Bounded Central-Differencing Scheme

The LES calculation uses a bounded central-differencing scheme. In a central-differencing scheme, the cell face center value is approximated by linear interpolation between the two nearest

neighboring cell values. For a standard central-differencing scheme, the convective flux is computed as

$$(\dot{m}\phi)_f = \dot{m}_f[f\phi_0 + (1-f)\phi_1] \tag{3.29}$$

where the linear interpolation factor is defined as

$$f = \frac{V_1}{V_0 + V_1} \tag{3.30}$$

and where V_0 is is the flux value across the cell face and V_1 is the flux value across the neighboring cell face. The variable f is related to mesh stretching and has a value of 0.5 for a uniform mesh.

An advantage of a central-differencing scheme over a second-order upwind scheme is that it preserves turbulent kinetic energy when used to discretize velocity. This makes it more suited to Large Eddy Simulations, where upwind schemes cause turbulent kinetic energy to decay rapidly. The central-differencing scheme used in this calculation is a bounded central-differencing scheme, in which the convective flux is computed as

$$(\dot{m}\phi)_f = \begin{cases} \dot{m}\phi_{FOU} & for\ \zeta < 0\ or\ 1 < \zeta \\ \dot{m}(\sigma\phi_{CD} + (1-\sigma)\phi_{SOU} & for\ 0 \le \zeta \le 1 \end{cases} \tag{3.31}$$

where ϕ_{FOU} is the cell-face center value obtained through first-order upwind interpolation, ϕ_{SOU} is the cell-face center value obtained through second-order upwind interpolation, ϕ_{CD} is the cell-face center value obtained through standard central-differencing interpolation, and ζ is the Normalized-Variable Diagram (NVD) value detailed in section 3.2.1.2.

The bounded central-differencing scheme turns into a first-order upwind scheme when the boundedness criterion is not satisfied, so this scheme can be more dissipative than the standard central-differencing scheme, especially on coarser meshes. However, the bounded central-differencing scheme provides a good compromise between accuracy and robustness and is the recommended scheme for LES of complex turbulent flows.

3.3.2.2 Implicit Time Integration

For transient simulations such as an LES, time is discretized in addition to a spatial discretization. This means that the total time integral is divided into smaller time-steps. For an implicit calculation, each physical time-step is then broken into a number of inner iterations to converge the solution for that instant in time.

The solution of the governing equations is calculated at different time-steps, and each calculation requires the solutions from previous time-steps. Time integration schemes are distinguished by the number of time-steps they use for integration as well as on which time-step the fluxes and sources are integrated.

The simulations carried out in this study use a basic implicit second-order temporal discretization scheme. This discretization scheme uses the solution at the current time-step, $n+1$ as well as the solutions from the two previous time-steps, n and $n-1$. The resulting backward differentiation formula is

$$\frac{d}{dt}(\rho\chi\phi V) \approx \left(\frac{3}{2}(\rho\chi\phi V)_{n+1} - 2(\rho\chi\phi V)_n + \frac{1}{2}(\rho\chi\phi V)_{n-1}\right)\frac{1}{\Delta t}. \tag{3.32}$$

For the first time-step of a second-order temporal simulation, a first-order discretization is used because the solutions at only two time-steps are available.

3.3.3 Noise Prediction

Chapter 2 discussed how resolving the far-field noise directly using LES was prohibitively time- and computationally expensive. Four different hybrid approaches were mentioned, but of those four, the FW-H method is presently the most widely implemented and thus is the method this work continues with. This section discusses the full numerical formulation of the FW-H analogy.

3.3.3.1 FW-H Analogy

The noise prediction for the LES was calculated using the Ffowcs Williams - Hawkings (FW-H) integral formulation discussed in chapter 2. This method calculates the far-field sound that is radiated from near-field flow data from the CFD solution.

Ffowcs Williams and Hawkings [99] extended the work of Lighthill [4] and Curle [48] to the formulation of aerodynamic sound generated by a surface in motion. Similar to the Lighthill equation, they recast the equations of fluid motion in the form of an inhomogeneous wave equation, but they cast certain flow variables as generalized functions.

The present work uses Farassat's Formulation 1A solution of the FW-H analogy. Pressure, density, and velocity are sampled on a conical permeable surface that extends X diameters beyond the nozzle exit and encloses the turbulent jet flow. Using the equation derived by Brentner and Farassat [129], the acoustic pressure for an observer located outside the FW-H surface can be calculated as

$$\begin{aligned} 4\pi p(x,t) = &\int_S \left[\frac{\rho_0\left(\dot{U}_n + U_{\dot{n}}\right)}{r(1-M_r)^2} + \frac{\rho_0 U_n\left(r\dot{M}_r + a_\infty M_r - a_\infty M^2\right)}{r^2(1-M_r)^3}\right]_{ret} dS \\ &+ \frac{1}{a_\infty}\int_S \left[\frac{\dot{L}_r}{r(1-M_r)^2} + \frac{L_r\left(r\dot{M}_r + a_\infty M_r - a_\infty M^2\right)}{r^2(1-M_r)^3}\right]_{ret} dS \\ &+ \int_S \left[\frac{L_r - L_M}{r^2(1-M_r)^2}\right] dS. \end{aligned} \tag{3.33}$$

Here, ρ_0 is taken to be the ambient density, v_i is the velocity of the FW-H surface, and $M_i = a_\infty v_i$ is the surface Mach number based on the ambient speed of sound a_∞. U_i is defined by Eqn. (3.34) and L_i is defined by Eqn. (3.35). Quantities with dots represent time derivatives with respect to the source time t, and the subscripts denote scalar dot products with the surface unit normal $\hat{n}_i$, the unit radiation vector $\hat{r}_i$, or the Mach number M_i.

$$U_i = \rho u_i/\rho_0 + v_i(1-\rho/\rho_0) \tag{3.34}$$

$$L_i = P_{ij}n_i + \rho u_i(u_n - v_n) \tag{3.35}$$

where $P_{ij} = (p - p_0)\delta_{ij} - \sigma_{ij}$ is the compressive stress tensor and σ_{ij} is the viscous stress tensor.

The first term on the right-hand side of Eqn. (3.33) represents the monopole source. This is analogous to the thickness noise, which is determined by the geometry of the body (3.34). The second and third terms on the right-hand side represent the dipole source. The dipole source is analogous to the loading noise, which is generated by the force that acts on the fluid due to the presence of the body (3.35).

STAR-CCM+ contains its own built-in FW-H solver, which is used in Chapter 5 to make noise predictions.

In the next chapter, the process of selecting the time and space discretization is discussed. A brief overview of the energy spectrum is given before describing its application to the grid generation for a Large-Eddy Simulation.

Chapter 4

Selection of the Space and Time Discretization

Due to the inherent CFD solver dependencies on space- and time discretization discussed in Chapter 3, one of the major questions that arises when developing a LES simulation is that of the appropriate size for both the grid and the time step. If the discretization is too coarse, the solvers will not converge to give accurate data; however, there is a point at which further refinement of the grid and time steps results in increased computation times that do not reflect an adequate improvement in the solution. The challenge is finding that point without participating in costly trial and error exercises. To this end, this thesis investigates grounding the grid discretization, and thus also the time discretization, within the concept of the turbulent energy cascade.

4.1 Turbulent Energy Cascade

The turbulent energy cascade can refer either to a direct cascade, in which energy transfers from large scales of motion to small scales; or an inverse cascade, in which energy transfers from small scales of motion to large scales. The idea of this cascade was first introduced by Richardson [130] in 1922 in the context of weather prediction. He noted that, although it was customary to separate circulatory motions in the atmosphere into either "convection" (heating of the air) or "dynamical instability" (kinetic energy of the wind), there were numerous forms which derived their energy from both sources. He also found that convective motions were hindered by small eddies that resulted from dynamic instability. He summarized his findings as follows:

"Big whirls have little whirls
that feed on their velocity,
and little whirls have lesser whirls
and so on, to viscosity
- in the molecular sense." [130]

The turbulent energy cascade was later improved upon by Kolmogorov [131] in 1941. Kolmogorov argued that the directionality of the large-scale eddies in a flow is lost when the energy is transferred to successively smaller eddies, and thus the small-scale turbulence is isotropic at a sufficiently high Reynolds number. All geometrical information about the eddies is also lost, so he concluded that the statistics of small-scale motions are universal [132].

Kolmogorov developed two 'similarity hypotheses' stemming from the universal nature of the small-scale motions at sufficiently high Reynolds numbers. The first hypothesis states that the universal form of the small-scale motions is determined by the kinematic viscosity ν and the dissipation rate ϵ. This smallest length scale, at which kinetic energy is dissipated into heat, is called the Kolmogorov length scale and is defined as

$$\eta \equiv \left(\frac{\nu^3}{\epsilon}\right)^{\frac{1}{4}}. \tag{4.1}$$

Kolmogorov's second similarity hypothesis states that there is a range in which motions of a scale larger than the Kolmogorov length scale have a universal form that is uniquely determined by ϵ, independent of ν [132]. If we take L to be the flow scale, l_0 to be the length scale of the largest eddies in the flow, l_{EI} to be the demarcation between the anisotropic large eddies and the isotropic small eddies, l_{DI} to be the demarcation between negligibility and significance of viscous effects, and η to be the Kolmogorov length scale, then the various eddy sizes l can be visualized in Figure 4.1.

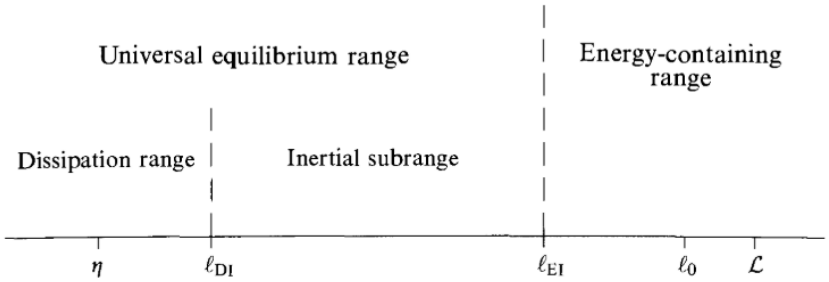

Figure 4.1: Length scales and ranges of eddy sizes l on a logarithmic scale [132]

There are two additional length scales of concern in this thesis: the Taylor microscale and the turbulent mixing length. The Taylor microscale is the intermediate length scale between the dissipation range and the inertial subrange at which fluid viscosity affects the turbulence in the flow, but the kinetic energy is not dissipated into heat. The Taylor microscale is defined as

$$\lambda \equiv \sqrt{10\nu\frac{\kappa}{\epsilon}} \tag{4.2}$$

where κ indicates the turbulent kinetic energy. The turbulent mixing length represents a mean eddy size larger than a fluid's mean path and lies in the inertial subrange, where the flow is not strongly affected by viscosity. In an unbounded flow the eddy viscosity can be taken as a constant. In a boundary layer flow, the mixing length is specified as

$$l_m \equiv \kappa y \tag{4.3}$$

where y is a Cartesian coordinate. In a wall-bounded flow the mixing length is damped near the wall using the van Driest damping function [133]. Taking y^+ to be the distance from the wall normalized by the viscous length scale and A to be a dimensionless damping constant, then the turbulent mixing length becomes

$$l_m \equiv \kappa y\left[1 - e^{\left(\frac{-y^+}{A}\right)}\right]. \tag{4.4}$$

The approximate range of these three length scales are given in Figure 4.2.

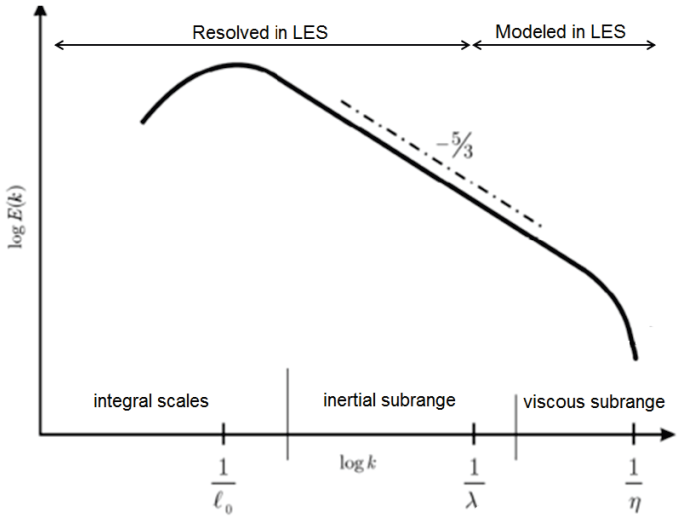

Figure 4.2: Approximate ranges of the mixing length, Taylor microscale, and Kolmogorov length scale against a plot of energy vs wavenumber [134]

4.1 Spatial Discretization

The nozzle geometry focused on in this thesis is the Georgia Tech GTRI nozzle created for the FAA ASCENT 59 project. It is a dual-stream concentric nozzle with a short mixing duct. The geometry is shown in Figure 4.3. It has an exit diameter D_j of 1.6 inches.

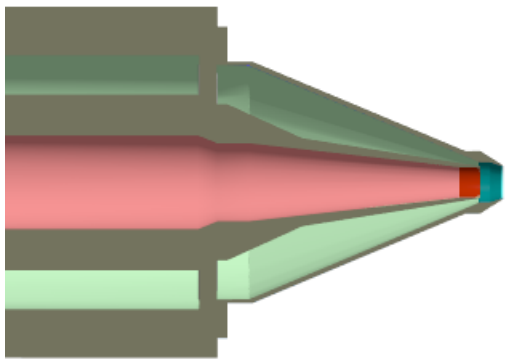

Figure 4.3: Nozzle geometry

4.1.1 Initial Grid Development

To begin, a polyhedral grid of arbitrary grid size was generated. in STAR-CCM+. This grid contained twelve levels of grid refinement that fanned out from the nozzle exit, with the finest

refinement near the nozzle exit and growing coarser with each subsequent level. The refinement regions chosen were arbitrary, with the denser regions kept smaller to conserve grid and file size. Figure 4.4 shows the grid near the nozzle exit, and the refinement cones are shown in Figure 4.5.

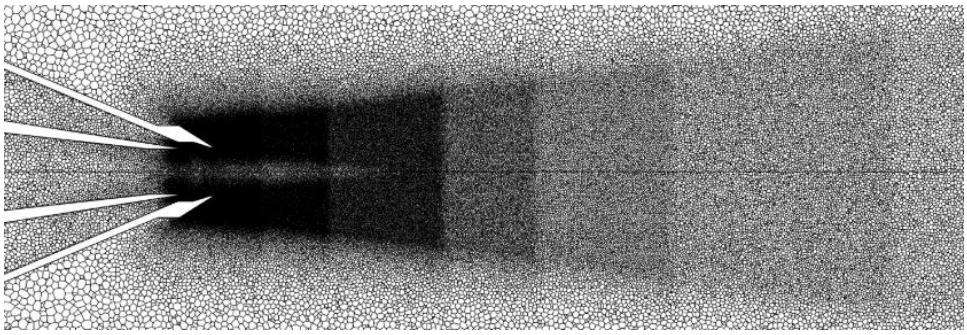

Figure 4.4: Grid refinement to 15 D_j downstream

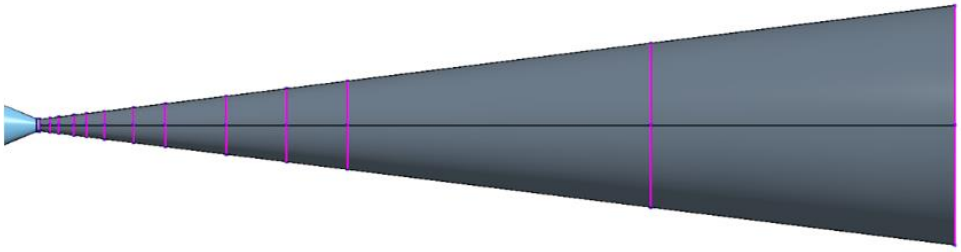

Figure 4.5: Grid refinement cones extending to 2.5, 5, 7,5, 10, 20, 30, 40, 50, 100, and 150 D_j downstream

The smallest arbitrary grid refinement used at the nozzle exit was 0.01 inches, or 0.625% of Dj. The largest grid refinement at 150 Dj downstream was 1.5 inches, or 93.75% of Dj.

4.1.2 Grid Refinement Using the Energy Cascade

A RANS calculation was performed on the initial, arbitrary grid, running out to 5,000 iterations. The mixing length and the Taylor microscale were extracted from the data field in each volumetric refinement and normalized by the corresponding grid length, which was obtained by taking the cube root of the polyhedral cell volume. The Kolmogorov length scale was largely disregarded due to it being smaller than the Taylor microscale.

Using the grid length Δ at $x/D_j = 0$, the target grid sizes to resolve both the Taylor microscale λ and the mixing length l were calculated and are shown in Table 4.1.

Table 4.1: Grid size calculations

x/D	Δ	λ/Δ	l/Δ	Target Δλ	Target Δl
0	0.0100	0.6227	14.9534	0.0108	0.0108
2.5	0.0200	0.4721	15.4397	0.0191	0.0260
5	0.0300	0.4411	20.7239	0.0290	0.0567
7.5	0.0475	0.3681	21.0645	0.0353	0.0842
10	0.0650	0.3328	21.6496	0.0426	0.1154
15	0.0825	0.3423	26.0989	0.0512	0.1624
20	0.1000	0.3498	31.4355	0.0650	0.2431
30	0.1500	0.3290	34.5223	0.0888	0.3881
40	0.2000	0.3543	41.3448	0.1246	0.6054
50	0.5000	0.2016	24.9880	0.1664	0.8592
100	1.0000	0.2125	44.4880	0.3609	3.1460
150	1.5000	0.1909	47.8373	0.5050	5. 2708

The initial grid shown in the first row of Table 4.1 is coarser than it needs to be to resolve the Taylor microscale but finer than it should be to resolve the turbulent mixing length, as λ/Δ (the Taylor microscale length divided by the local grid length) is less than 1, while l/Δ (the turbulent mixing length divided by the grid length) is greater than one. The target Δλ indicates the target grid length for resolution of the Taylor microscale, calculated as

$$\frac{(\lambda/\Delta)/\Delta}{\Delta_0} \tag{4.5}$$

where Δ is the local grid length and Δ_0 is the grid length at x/D=0. The target grid length for the resolution of the mixing length Δl is calculated using the same equation with l/Δ in place of λ/Δ. The final grid length used in the simulation should fall between these two values. The Taylor microscale, turbulent mixing length, and the grid length are plotted in Figure 4.6.

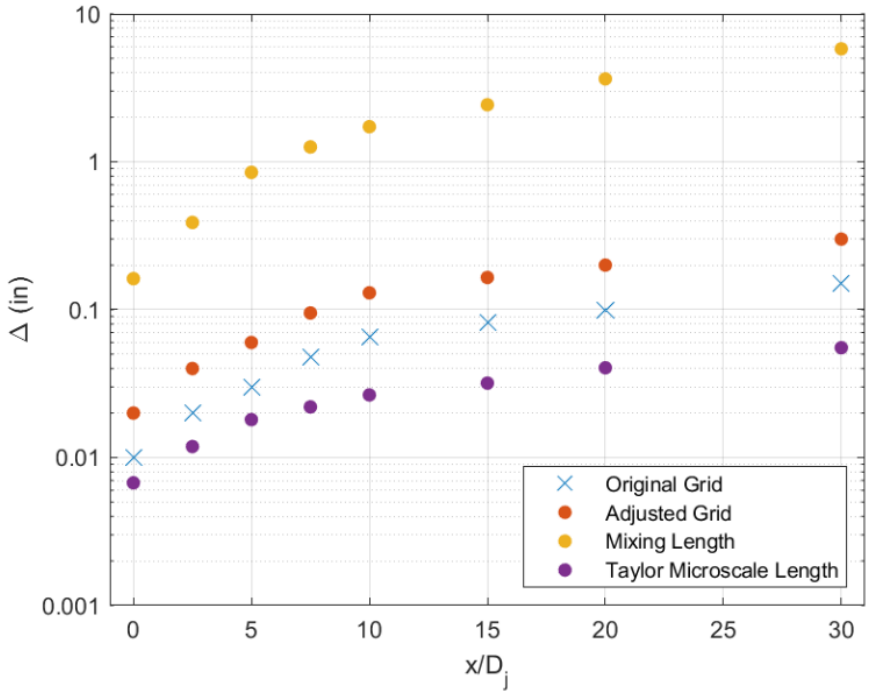

Figure 4.6: Grid length Δ in relation to Taylor microscale λ and mixing length l up to 30 D_j

Figure 4.6 shows the Taylor microscale, turbulent mixing length, and grid length extracted from a RANS calculation at each x/D location. The initial grid created for this simulation ("Original Grid") was biased close to the Taylor microscale, so the grid length was increased to fall more evenly between the two length scales ("Adjusted Grid").

4.1.3 Model Energy Spectrum

The wavenumber used in Figure 4.2 was calculated by dividing 2π by the wavelength λ. For these calculations, the grid cell lengths are used for the wavelength. In viewing grid generation through the lens of the energy spectrum, one can take the integral of the energy spectrum shown in Figure 4.2 with respect to the wavenumber and define a critical wavenumber which resolves a targeted ratio of total kinetic energy. This critical wavenumber then defines the grid cell lengths. Biasing the grid closer to the Taylor microscale means resolving more small-scale structures and a larger fraction of the total kinetic energy, while biasing the grid closer to the mixing length means modeling more of the energy

spectrum via the subgrid scale model discussed in Chapter 3. The goal of the present research is to resolve up to 80% of the total kinetic energy.

A MATLAB script was written to calculate a sample Pao energy spectrum using the mixing length, Taylor microscale, and Kolmogorov length scales extracted from STAR-CCM+. The energy spectrum function was modeled as

$$E(\kappa) = C\epsilon^{2/3}\kappa^{-5/3} f_L(\kappa L) f_\eta(\kappa\eta). \tag{4.6}$$

with $C = 1.5$ and $\epsilon = 1$. Within the energy spectrum function, f_L determines the shape of the energy-containing range and f_η determines the shape of the dissipation range. f_L tends to unity for large κL while f_η tends to unity for small $\kappa\eta$. The nondimensional function f_L is specified as

$$f_L(\kappa L) = \left(\frac{\kappa L}{[(\kappa L)^2 + c_L]^{1/2}}\right)^{5/3+p_0} \tag{4.7}$$

where c_L is a positive constant and $p_0 = 2$. The nondimensional function f_η is specified as

$$f_\eta(\kappa\eta) = exp\{-\beta\{[(\kappa\eta)^4 + c_n^4]^{1/4} - c_\eta\}\} \tag{4.8}$$

where c_η is a positive constant and $\beta = 5.2$.

Within the MATLAB script, κ was defined as a range of wavenumbers from $\kappa = 10^{-2}$ to $\kappa = 10^4$ with an incremental step size of 0.1, L was taken to be the jet diameter, and η was the Kolmogorov length scale extracted from STAR-CCM+. Assuming a high Reynolds number, the constants c_L and c_η were taken to be 6.78 and 0.4, respectively, as given by Pope [132].

Figure 4.7 and Figure 4.8 show where the wavenumbers associated with the extracted mixing length, Taylor microscale, and Kolmogorov length scales fall on the calculated energy spectrum, along with the location of the wavenumber associated with the targeted 80% resolution of turbulent kinetic energy and the wavenumber associated with the grid length at an x/D of 4.89 and 9.89.

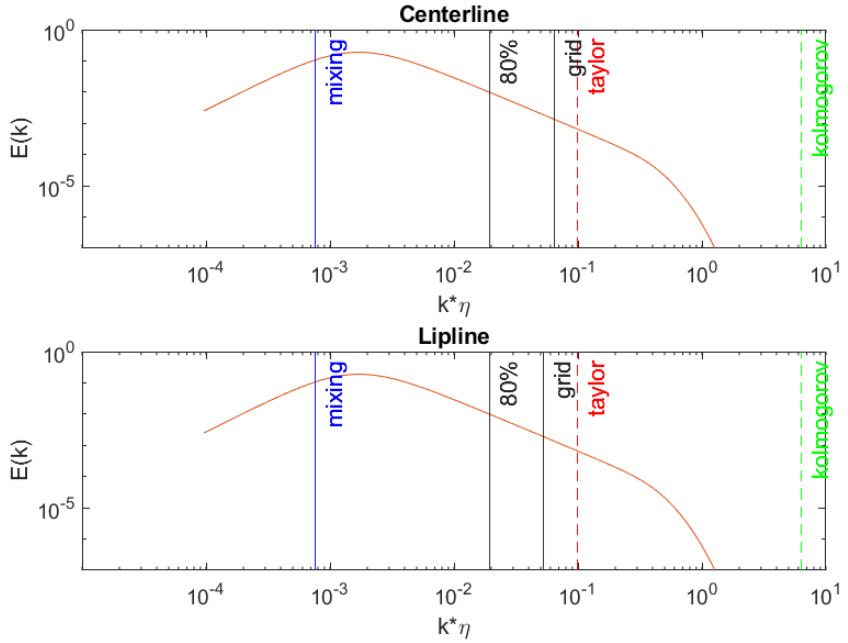

Figure 4.7: Pao energy spectrum at x/D_j = 4.89 for the centerline (top) and lipline (bottom)

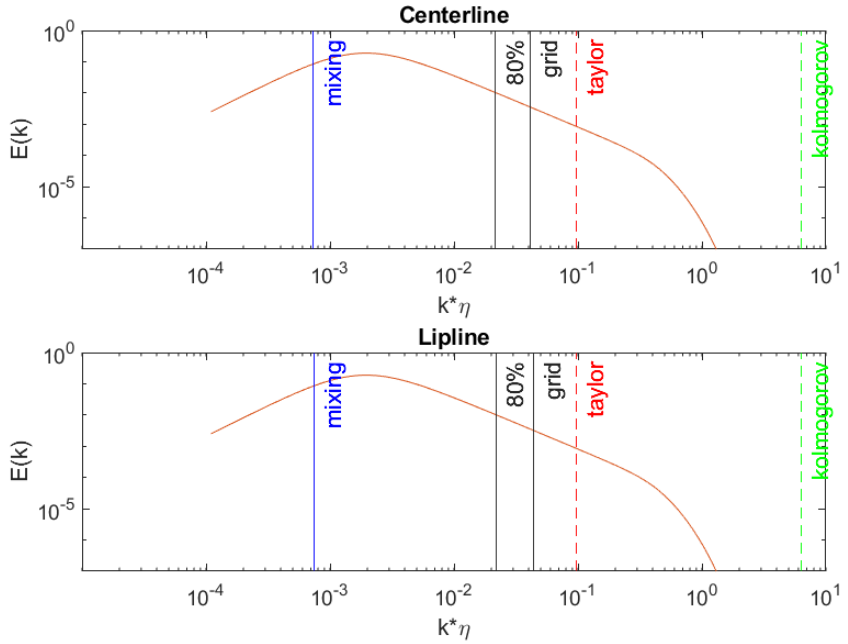

Figure 4.8: Pao energy spectrum at x/D_j = 9.89 for the centerline (top) and lipline (bottom)

For both the centerline and the lipline at each location, the grid length fell between the 80% mark and the Taylor microscale length. Therefore, the grid was technically over-resolved, and should

have had a smaller cell size than necessary to resolve 80% of the turbulent kinetic energy. Still, to better capture the turbulence intensity, further grid refinement was added to the free shear layer.

4.1.4 Further Refinement of the Free Shear Layer

To further refine the grid around the free shear layer without making the grid prohibitively large, the grid refinement cones shown in Figure 4.4 and Figure 4.5 had to be adjusted. The cones were given a smaller radius, shown in Figure 4.9, and hollowed out in the middle of the potential core where the refinement wasn't necessary, shown in Figure 4.10. This refined grid contained 62.7 million cells.

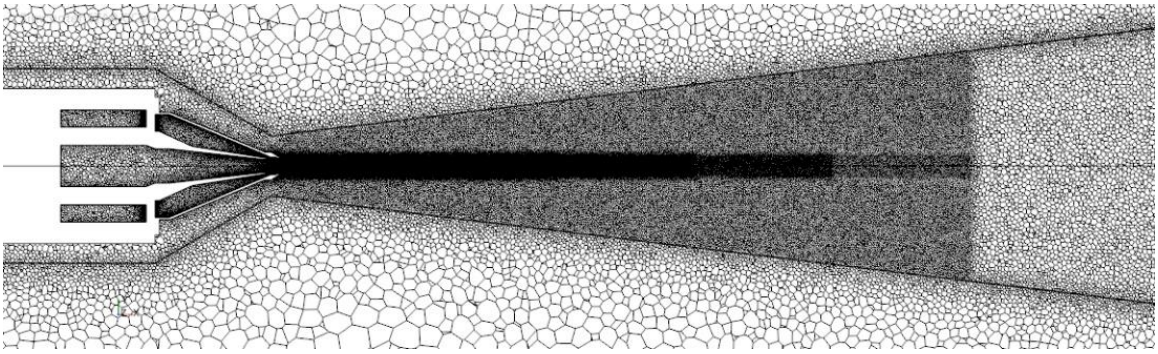

Figure 4.9: New grid refinement to 65 D_j downstream

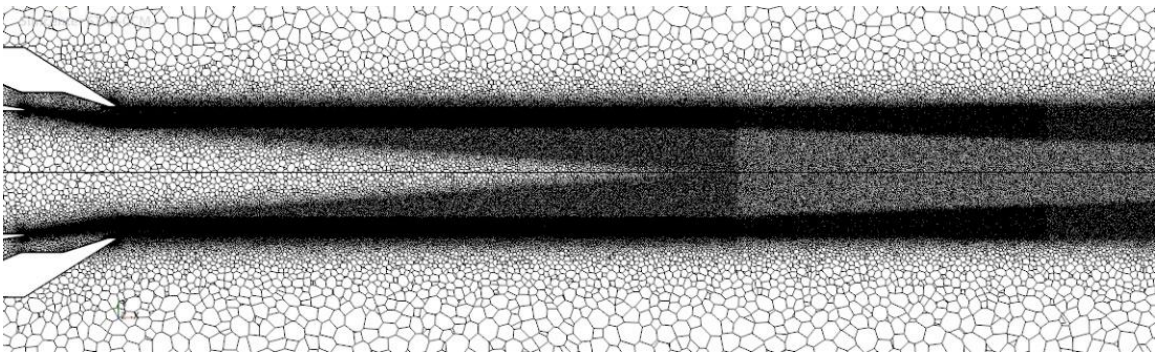

Figure 4.10: New grid refinement to 8 D_j downstream

The smallest grid length, located around the nozzle exit, was reduced from 0.01 inches to 0.0075 inches, or 0.469% of Dj. This grid refinement was also extended inside the nozzle to capture the turbulence from the lip of the nozzle core. The largest grid length at 150 Dj downstream was reduced from 1.5 inches to 0.6609 inches, or 41.3% of Dj. This new grid included two "buffer layers"

leading out to and across the FW-H surface. The buffer layer closest to the potential core had a grid length of 1.6 inches and extended across the FW-H surface. The buffer layer that lay beyond the FW-H surface had a grid length of 1.7 inches. The far-field mesh was very coarse, with a base grid length of 5 inches, or 312.5% of Dj.

This was the final mesh that was settled upon for this thesis. All results discussed in Chapter 5 were taken from this configuration.

4.2 Temporal Discretization

After establishing the spatial discretization, the temporal discretization could be calculated. A RANS simulation was performed on the grid discussed in Section 4.1 to obtain the flow velocity. Then the length of a convective time unit could be calculated using the equation

$$\tau = \frac{\Delta * \Delta t}{u} \tag{4.9}$$

where Δ is the grid length, Δt is the time step, and u is the flow velocity. In setting the length of the convective time unit to 1, the size of the time step could be calculated. This was achieved in STAR-CCM+ using a field function. For this Large-Eddy Simulation, the time step was established as 1 microsecond.

The next chapter provides the results of the Large-Eddy Simulation. The velocity and turbulent flow statistics are discussed and compared to experimental data. The acoustic results are also compared to experimental data, and remarks are made toward the viability of STAR-CCM+ for these problems.

Chapter 5

Large-Eddy Simulation Verification

The Large-Eddy Simulation for the two-stream jet was run with NPR = 1.39 and TTR = 1.0 for both the core and bypass flow. The simulation ran for 12 days, with a total CPU time of 546,288 hours. 40,000-time steps were collected, with a time step length of 1 microsecond. This chapter first compares the LES velocity and turbulence statistics for both the outer jet lipline and centerline to the experimental values obtained by Georgia Tech. Then, the rms and autocorrelation values of the velocity taken along the lipline as well as the spectra of the velocity fluctuations are shown. The Power Spectral Density (PSD) of the pressure fluctuations at multiple azimuthal angles and radial distances were calculated and compared to experiments, as well as the Overall Sound-Pressure Level (OASPL).

5.1 Velocity and Turbulence Statistics

Before showing any acoustic data obtained from the LES, the flow field was validated against experimental values obtained by Georgia Tech. The experiments were conducted at conditions equivalent to those used in the simulation. Figures Figure 5.1 and Figure 5.2 show the centerline and lipline mean axial velocity profiles, respectively, shown as U/U_j where U_j is the jet exit velocity. Figure 5.1 shows that the potential core of the LES flow was slightly shorter than that for the experimental flow. These results are similar to the velocity profiles obtained by Brès *et al.* [96] with the LES solver CharLES that was discussed in Chapter 2. Additional work has shown that the modeled potential core length for a fixed Mach number can be affected by variables such as temperature [53,82], shear layer thickness [82,135], mesh size [96,136], and subgrid scale model [136,137]. For the current study, the LES slightly underpredicts the axial velocity for both the centerline and the lipline but shows good overall agreement.

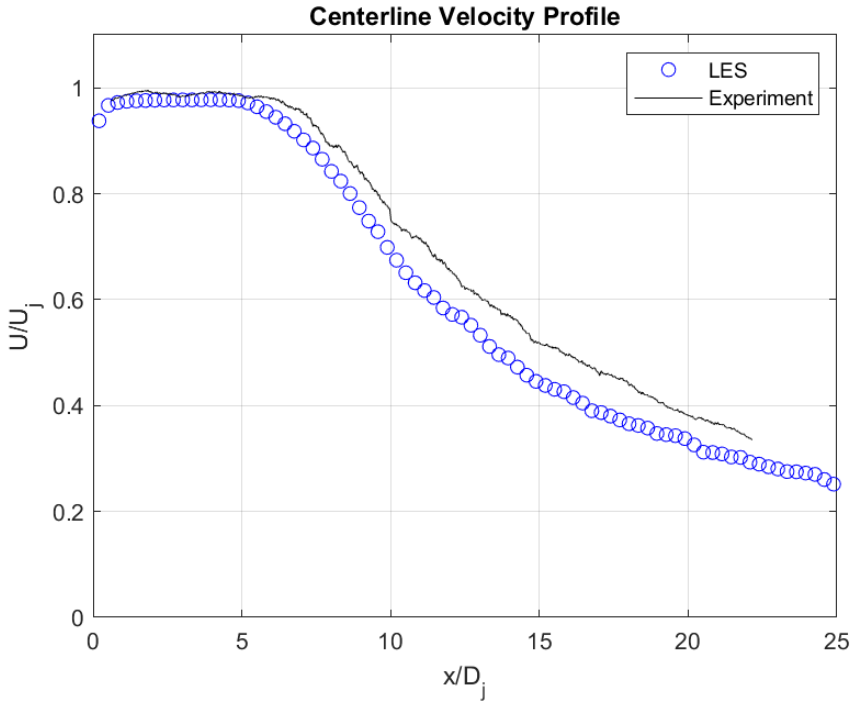

Figure 5.1: Centerline velocity profiles

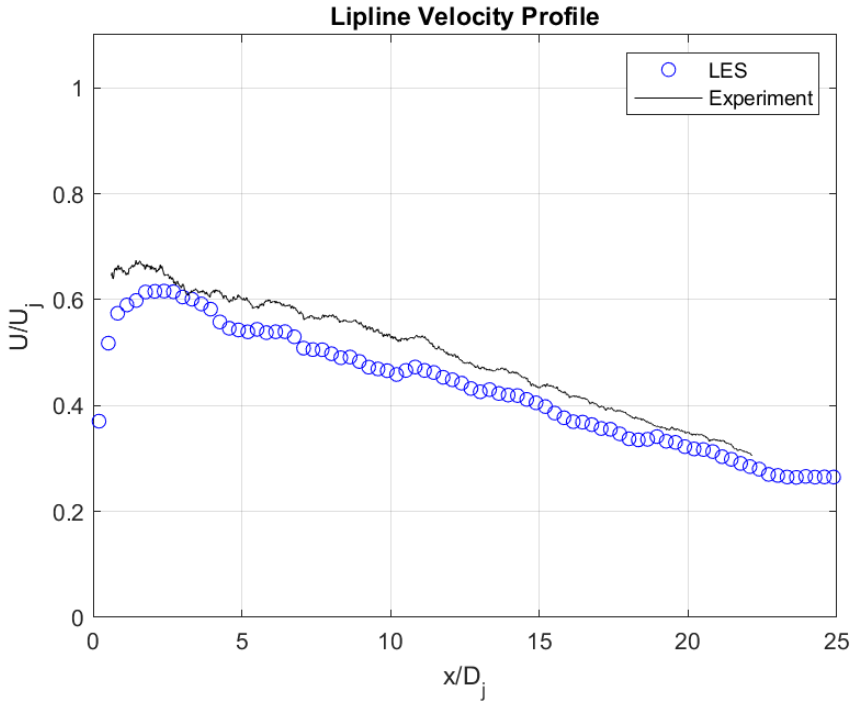

Figure 5.2: Lipline velocity profiles

The turbulence intensities shown in Figures Figure 5.3 and Figure 5.4 were calculated by finding the standard deviation of the axial velocity fluctuations divided by the jet exit velocity, or

$$TI = \frac{U'}{U_j} \tag{5.1}$$

where

$$U' = \frac{1}{n}\sqrt{\sum (U - \bar{U})^2}, \tag{5.2}$$

in which n is the number of samples, U is the instantaneous velocity, and $\bar{U}$ is the mean value of the velocity. Figure 5.3 shows that the LES misses the peak value and slightly underpredicts the turbulence intensity but shows good overall agreement with experiments. Figure 5.4 indicates that on the liplines the turbulence intensity is overpredicted near the nozzle exit in the LES. The boundary layer at the jet exit in this simulation was not fully turbulent, resulting in lower frequencies further downstream and an increase in the time necessary to capture the statistic. Brès *et al.* [96] introduced synthetic turbulence [138–140] inside the nozzle exit to obtain a better match with experimental turbulence statistics. This was not included in the present simulations.

Overall, the LES showed good agreement with the experimental values, indicating that the developed grid was refined enough for this problem.

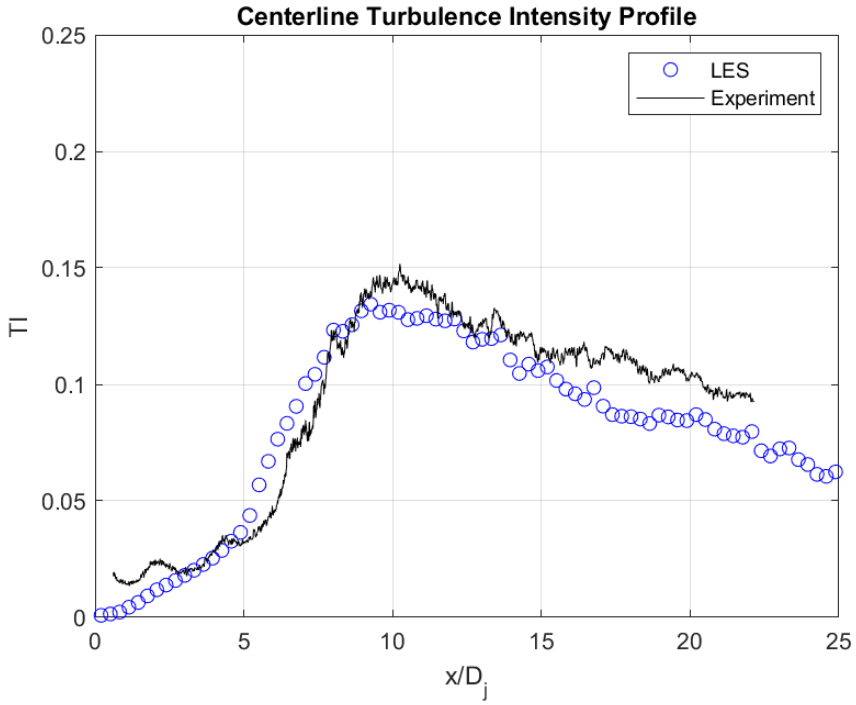

Figure 5.3: Centerline turbulence intensity profiles

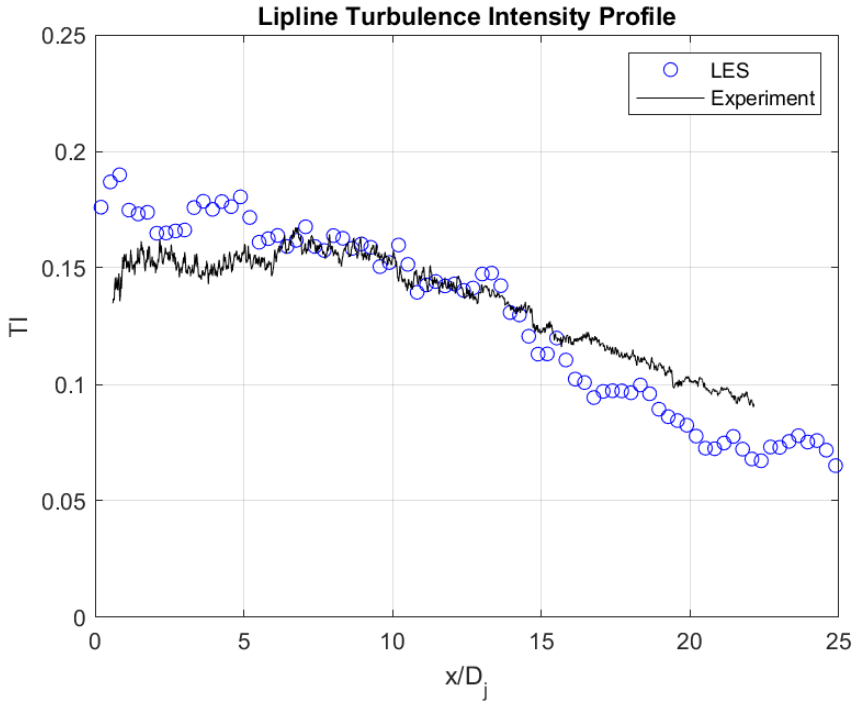

Figure 5.4: Lipline turbulence intensity profiles

5.2 Velocity Spectra

In addition to the acoustic data, the time history data on the lipline were analyzed. The autocorrelation coefficient was found for the downstream location of x/D = 5, from which the peak frequency was estimated and the integral timescale was determined. The root mean square (rms) of the velocity fluctuation was calculated and compared to expected values, and the spectra of the velocity fluctuations were found for increasing distances downstream of the nozzle exit.

5.2.1 Autocorrelation

An important statistic that can be considered for the time history of the velocity collected along the nozzle lipline (y = 0.5Dj) is the velocity autocovariance

$$R(s) \equiv \langle u(t)u(t+s)\rangle. \tag{5.3}$$

When normalized by the variance of the velocity, the autocovariance becomes the autocorrelation coefficient,

$$\rho(s) \equiv \langle u(t)u(t+s)\rangle / \langle u(t)^2\rangle, \tag{5.4}$$

where $\langle u^2\rangle$ is the variance and $u(t) \equiv U(t) - \langle U\rangle$ is the fluctuation about the mean velocity $\langle U\rangle$. The autocorrelation function gives the correlation coefficient between the velocity fluctuations obtained at time t and time $t + s$. The correlation diminishes as the lag delay s increases.

The autocorrelation function can also be found by taking the inverse transform of the two-sided Spectral Density Function. It is then normalized by the autocorrelation value at zero time delay, giving the autocorrelation coefficient, shown in Figure 5.5. The value at zero time delay is the mean square value of the signal, which is equal to the integral of the autocorrelation spectrum with respect to frequency. The mean square value obtained from this problem was 0.0202 m/s. Additionally, the integral of the time delay, which is also referred to as the integral timescale $\bar{\tau}$, can also be calculated as

$$\bar{\tau} \equiv \int_0^\infty \rho(s)ds, \tag{5.5}$$

and its inverse gives an estimate of the peak frequency of the signal. The integral timescale for this problem at x/D = 0.5 was approximately 0.095ms, giving an estimated peak frequency of 10.5 kHz.

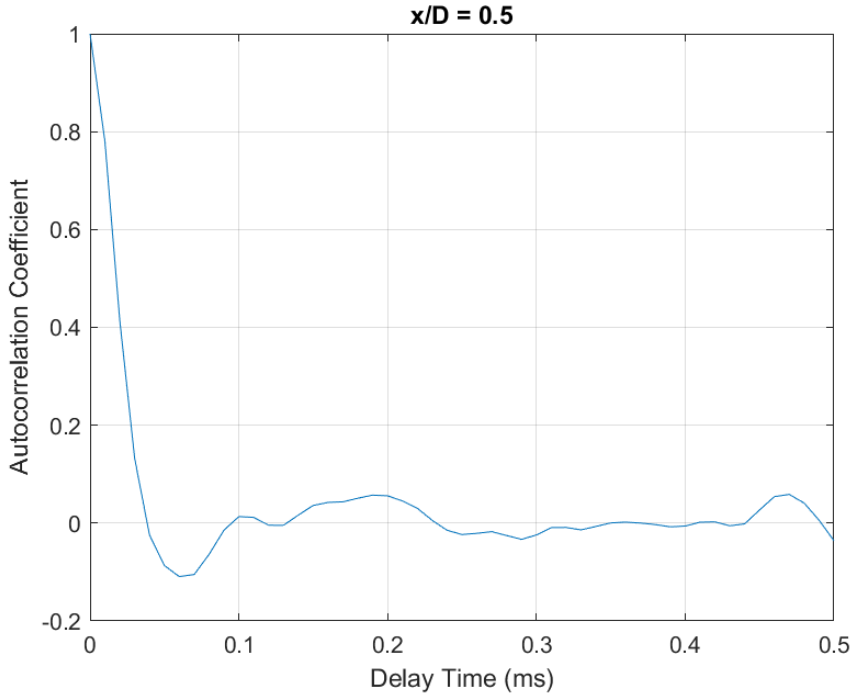

Figure 5.5: Autocorrelation Coefficient at x/D = 0.5

5.2.2 RMS and Power Spectral Density

The rms of the velocity fluctuations in a turbulent flow gives the turbulence intensity: the same quantity shown in Figure 5.3 and Figure 5.4. The rms just downstream of the exit of a free jet (normalized by jet exit velocity) is nominally expected to be 0.15 percent of the jet exit velocity [141]. The value obtained from the simulation showed good agreement at ~0.18, as shown in Figure 5.6.

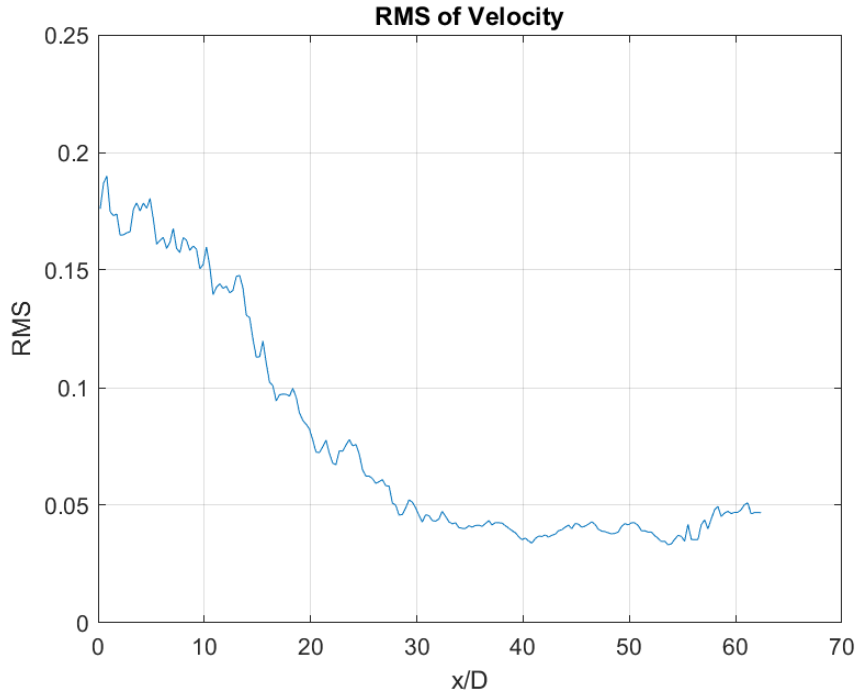

Figure 5.6: Root mean square of velocity fluctuations

Figure 5.6 extends Figure 5.4 to show the turbulence intensity farther downstream. The turbulence intensity decay levels off at approximately x/D = 30. These values align with the velocity spectra shown in Figure 5.7, where the shape of the PSD changes between x/D = 20 and x/D = 30. At axial locations closer to the jet nozzle, where the turbulence intensity is higher, there is more energy in the higher frequencies. As x/D increases and the turbulence intensity decreases, this energy shifts toward the lower frequencies and drops off at higher frequencies. This behavior follows that observed by Laurence [12].

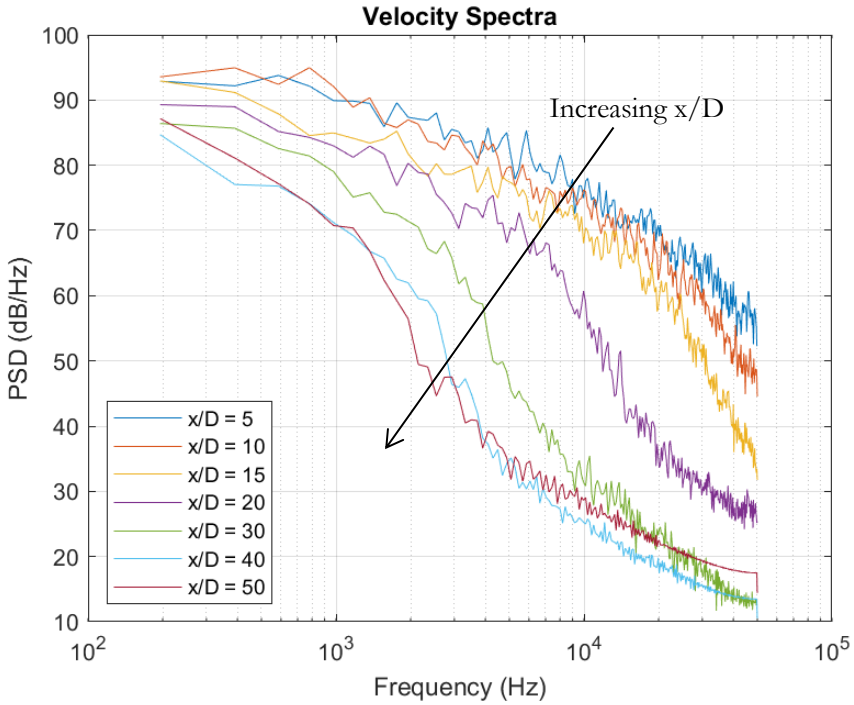

Figure 5.7: Spectra of velocity fluctuations

5.3 Acoustic Data

Acoustic data was extracted from STAR-CCM+ using the built-in FWH solver at radial distances of 50, 75, 100, 125, 150, 175, 180, and 200 jet radii. The distance of 180 radii corresponds to the radial distance at which experimental data was taken at Georgia Tech. Data was recorded at azimuthal angles of 20, 30, 40, 50, 60, 70, 80, 90, 100, and 110 degrees from the downstream, with 100 and 110 degrees being sideline angles. Due to the shape and size of the domain, sideline angle data for larger radial distances was unavailable. Table 5.1 shows the azimuthal angles that data was collected for each radial distance. Throughout this section, distances from the jet exit are referred to in units of the jet radius r.

Table 5.1: Acoustic data collected

Radial Distance	Azimuthal Angles
50-100r	$10\text{-}110^0$
125r	$10\text{-}60^0$
150r	$10\text{-}50^0$
175r & 180r	$10\text{-}40^0$
200r	$10\text{-}30^0$

This section shows the acoustic data obtained from STAR-CCM+. The simulation data is compared to the data obtained from experiments for assessment of the model. The acoustic data field is also examined in relation to itself to determine if its behavior follows the appropriate scaling laws for both the PSD and OASPL.

5.3.1 PSD Comparison with Experiments

Welch's power spectral density estimate was used to calculate the PSD for the data points taken at 180r, the distance equivalent to that at which experimental data was taken. The azimuthal angles available at this distance were only 30 and 40 degrees; therefore, the data used in the comparison at 90 degrees were extrapolated from the data taken at 100r by using the equation

$$PSD = 10\log\left(\frac{P_{xx}}{{p_0}^2}\right) - 20\log\left(\frac{r}{r_0}\right) \tag{5.6}$$

where P_{xx} is the power spectral density estimate given by Welch's method, p_0 is 2×10^{-5} Pa, and r/r_0 is the ratio of the desired radius to the radius being extrapolated from, in this case 180r and 100r, respectively. Figure 5.8–Figure 5.10 show these comparisons to experiments.

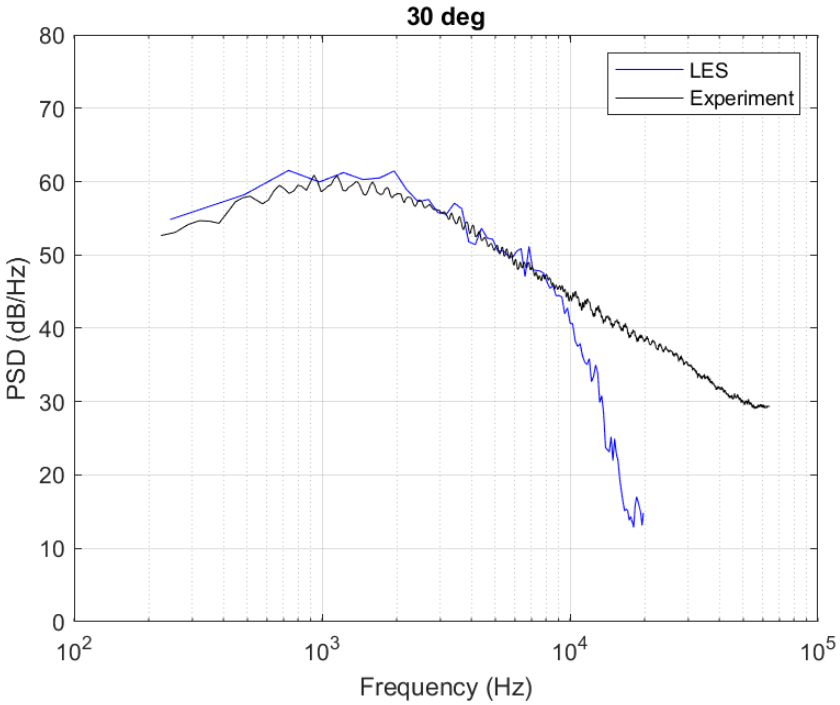

Figure 5.8: PSD comparison with experiments for 180r at 30^0

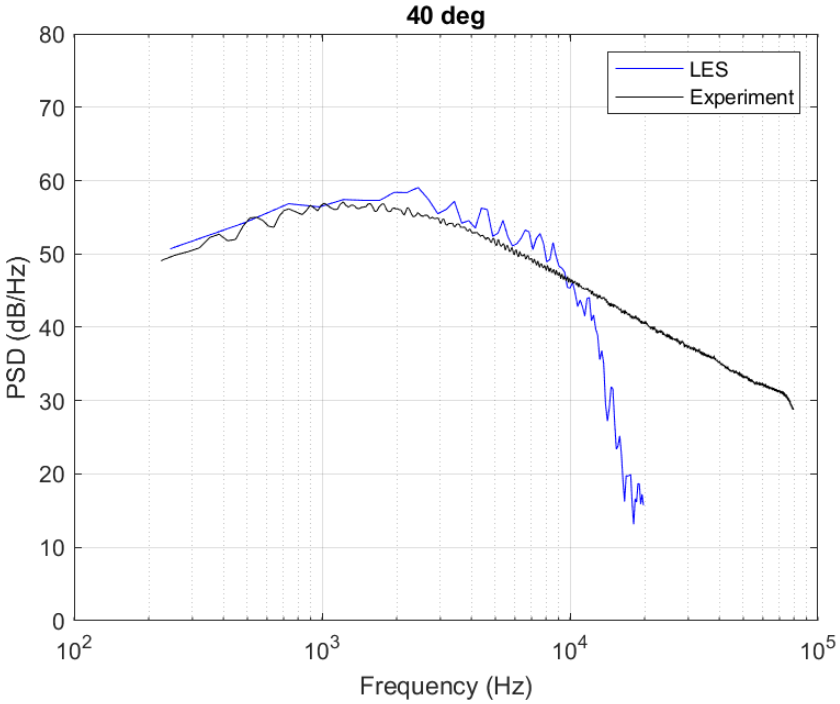

Figure 5.9: PSD comparison with experiments for 180r at 40^0

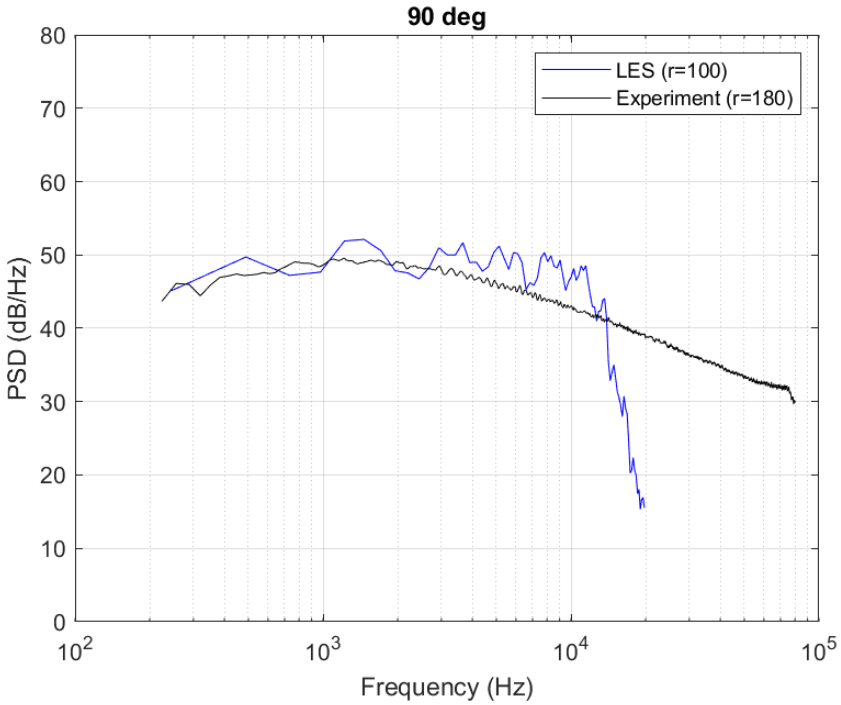

Figure 5.10: PSD comparison with experiments for 180r at 90^0

The results obtained from the LES show good agreement with the experimental data at all angles, but show better agreement at small angles, with the data taken at 30 degrees being the closest match. The LES captured lower frequencies better than higher frequencies, as expected. At each azimuthal angle, the PSD for the LES drops off sharply after 10,000 Hz due to limitations in the grid resolution, a behavior common to all LES simulations [8,77,96,138]. A longer period of data collection would minimize the large fluctuations in the PSD most visible in Figure 5.10.

5.3.2 Additional PSD Results

Welch's power spectral density estimate was then used to calculate the PSD for each data point listed in Table 5.1. All data points can be found in Appendices A.1 and A.2. Figure 5.11 shows the PSD for 50r, 100r, and 200r at 30 degrees. Figure 5.12 shows the PSD for 50r and 100r at 90 degrees.

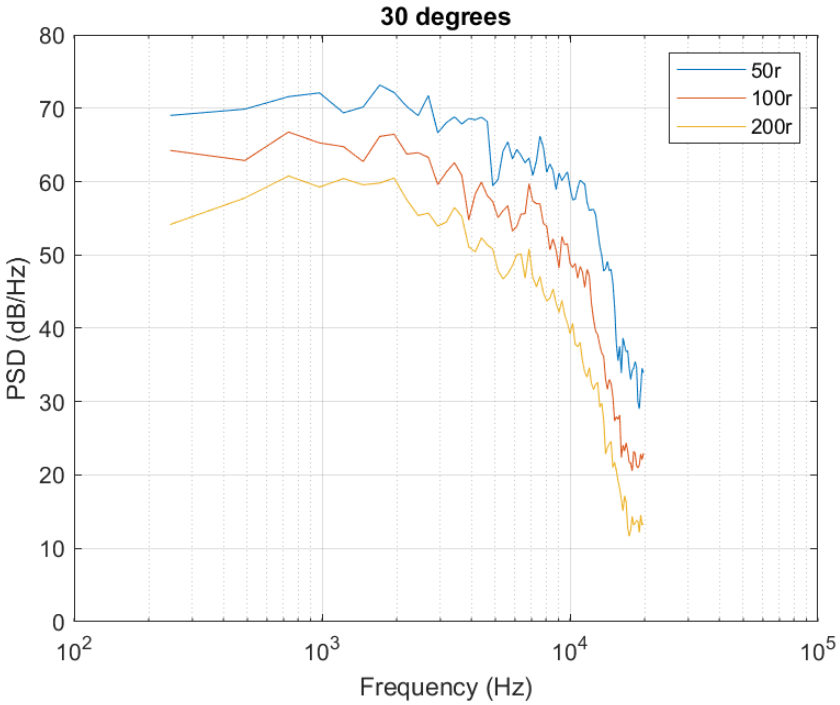

Figure 5.11: PSD for 50r, 100r, and 200r at 30^0

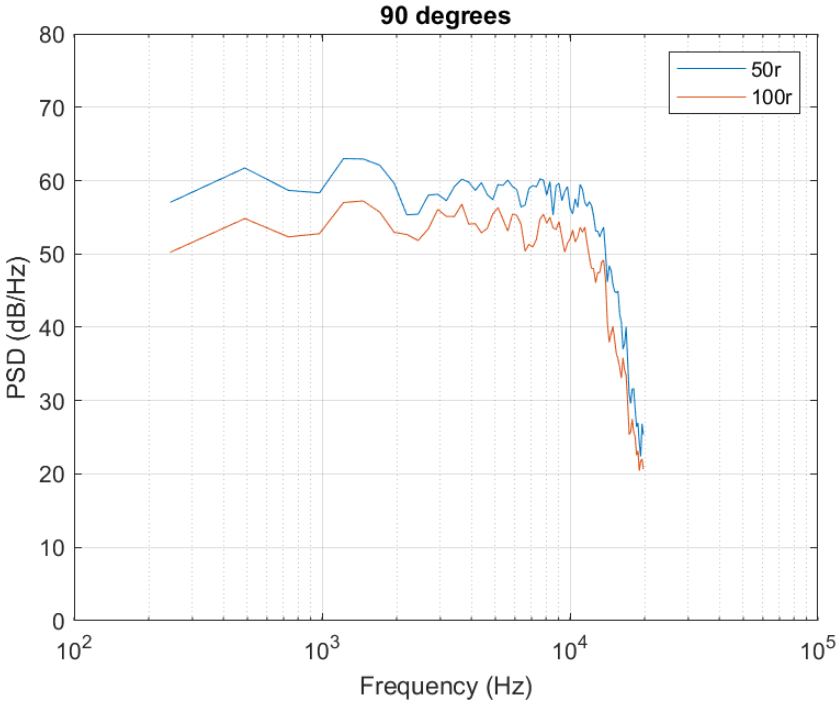

Figure 5.12: PSD for 50r and 100r at 90^0

The power spectral densities at different radii for both 30 and 90 degrees follow approximately the same shape as each other, with a reduction in magnitude as the radius increases. The average reduction in the power spectral density at 30 degrees up to approximately 13,500 Hz was 8.7 dB between 50r and 100r, and 8.13 dB between 100r and 200r. This follows the expected behavior of an equivalent reduction with the doubling of distance discussed in the next section. The average reduction at 90 degrees was 5.2 dB. As with the figures shown in Section 5.3.1, these PSD curves drop off sharply at frequencies above 10,000 Hz; however, the curves in Figure 5.12: PSD for 50r and 100r at 900 show a stronger presence of higher frequencies than those in Figure 5.11, which follows the observation that higher frequencies dominate at sideline angles [55]

5.3.3 OASPL

The OASPL provides a measure of the overall acoustic noise intensity across all frequencies. It is expressed in units of decibels (dB), which is defined as

$$dB = 20\log\left(\frac{p}{p_0}\right) \tag{5.7}$$

where p is pressure measured in Pascals (Pa) and p_o is the audible limit of the human ear, defined as 2×10^{-5} Pa [142]. The OASPL was calculated by taking the integral of the PSD at each downstream location to obtain the pressure value p to be used in Eqn. (5.7)

5.3.3.1 OASPL Comparison with Experiments

The overall sound-pressure level was calculated and compared with experiments, shown in Figure 5.13. Only three data points were available at 180r, two of which overlapped with the experimental dataset. The OASPL obtained from the LES showed good agreement with the experimental points, overpredicting by only 1 dB. There was a slight increase in OASPL at 180r

between 20 and 30 degrees, an increase that is also visible in Figure 5.14 for 200r as well as additional radial distances in Appendix A.3.

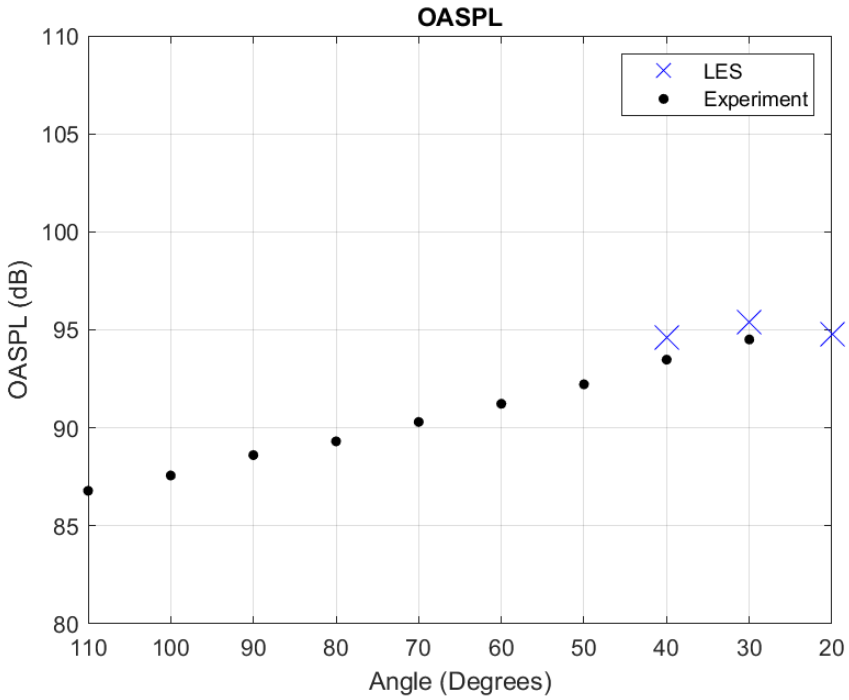

Figure 5.13: OASPL comparison to experiments: ×, LES; ●, experiment

5.3.3.2 Additional OASPL Results

The source of jet noise is often assumed to be a spherical source located at the nozzle exit [4]. Therefore, as mentioned previously, a 6 dB reduction in the OASPL is expected per doubling of the distance from the nozzle exit. Figure 5.14 shows the OASPL obtained from the LES at each azimuthal angle for 50, 100, and 200 radii.

Between 50 and 100 radii, an average noise reduction of 5.8 dB was found, which shows good agreement with the expected 6 dB reduction. The largest decrease was 6.75 dB at 30 degrees, and the smallest reduction was 4.97 dB at 50 degrees. Only two data points were obtained at 200 radii. For these two points, there was a difference in OASPL of 9.75 dB at 20 degrees and of 6.5 dB at 30 degrees. At 200 radii, the OASPL increased from 20 degrees to 30 degrees, which can also be seen at radial

distances of 75r, 125r, 175r, and 180r in Appendix A.3. This increase in the OASPL at angles close to the jet flow can also be seen in the work of Bodony and Lele [77] and Brès *et al.* [89,96], and is not an erroneous result.

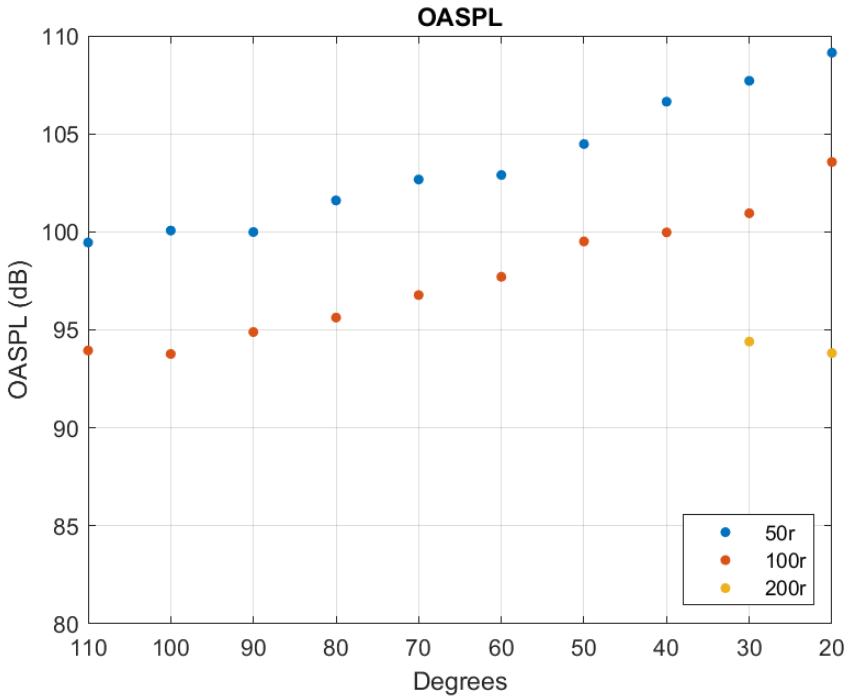

Figure 5.14: OASPL for 50r, 100r, and 200r

The next chapter will discuss the application of the procedure described in Chapter 4 and the results presented in Chapter 5 to a method of normalizing two different jets to the same thrust basis for comparison of acoustic analysis.

Chapter 6

Thrust Normalization and Acoustic Adjustment

In the quest for developing a quieter jet nozzle, the most common method of noise mitigation is changing the geometry. These changes include the addition of chevrons [143], fluid inserts [144], and mixers [145], or the alteration of the nozzle exit geometry to be square, oblong, or other arbitrary shapes [146], to name a few. These studies focus primarily on the acoustic change these alterations create; however, by changing the nozzle geometry, one also changes the amount of thrust a nozzle produces.

When it comes to applying these noise-reduction techniques in industry, a corresponding reduction in thrust is undesirable. A quieter engine that produces less thrust will be disregarded. Therefore, it is necessary to analyze the acoustic output of two engine designs on the same thrust basis. This chapter describes a method with which to normalize two acoustic datasets to the same thrust basis after data collection so a better comparison between the two can be performed. First, the method of control volume theory for thrust calculation is discussed. The thrust is then calculated for RANS simulations of two different nozzles before a second LES is performed. The raw acoustic data for both Large-Eddy Simulations is compared before the data obtained from the second LES is adjusted and compared again.

6.1 Control Volume Theory

To calculate the amount of thrust produced by an engine nozzle, the nozzle is considered as a control volume, or an arbitrary region of volume through which a fluid flows and each conservation principle is applied to an integral over said volume. The control volume follows the contours of the exhaust walls and is normal to the flow at the charging plane and the nozzle exit. The principle of conservation of momentum is considered for the calculation of the thrust.

6.1.1 Theory

The law of conservation of momentum states that within some problem domain, momentum is neither created nor destroyed, only changed by the action of forces. In the case of the nozzle, this means that the force of the thrust exiting the nozzle is equal to the force present on the charging planes minus the sum of all the pressure and viscous forces acting on the nozzle walls. This is illustrated in Eqn. (6.1):

$$F_{TH} = \int_{Charging\ Planes} \rho(\vec{V} \cdot \overrightarrow{u_x})(\vec{V} \cdot \vec{n}) + (Ps - Ps_\infty)(\overrightarrow{u_x} \cdot \vec{n})dA + \int_{Exh.\ Walls} [(\tau\vec{n})\overrightarrow{u_x}]dA \tag{6.1}$$

More simply, the thrust across the nozzle control volume can be calculated as

$$F_{TH} = (\dot{m}_6 V_6 + (P_6 - P_\infty)A_6) + (\dot{m}_{16} V_{16} + (P_{16} - P_\infty)A_{16}) + \int (P - P_\infty)\vec{n}\, dA + \int \tau\vec{n}\, dA \tag{6.2}$$

where $\dot{m}$ is the mass flow rate, V is the velocity, P is the pressure, P_∞ is the ambient pressure, A is the cross-sectional area, and τ is the viscous forces. The subscripts 6 and 16 refer to the core and bypass streams, respectively, as shown in Figure 6.1.

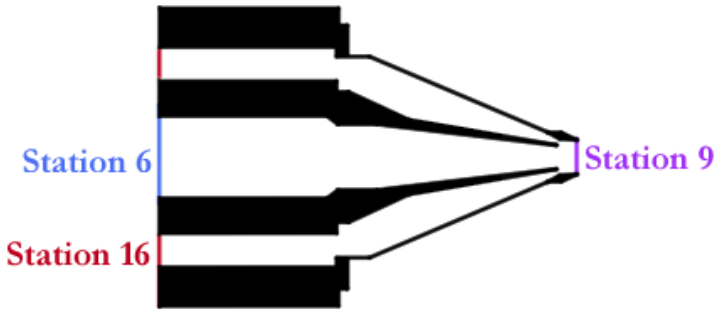

Figure 6.1: Nozzle control volume

The ideal thrust value is given as

$$F_{TH,ideal} = \dot{m}V_9 \tag{6.3}$$

where $\dot{m}$ is the combined mass flow rate of both streams. Analytically, $\dot{m}$ can be calculated as

$$\dot{m} = P_6 A M \sqrt{\frac{\gamma}{RT_6}} \left[1 + \frac{\gamma - 1}{2} M^2\right]^{-\left(\frac{\gamma+1}{2(\gamma-1)}\right)} \tag{6.4}$$

and V_9 is the fully-expanded velocity value taken just downstream of the nozzle exit or calculated as

$$V_9 = (\gamma RT) M^2. \tag{6.5}$$

The Mach number M is related to the ratio of the ambient pressure to the nozzle pressure on the charging plane (the inverse of the NPR) by the isentropic equation

$$\frac{P_0}{P_6} = \left[1 + \frac{\gamma - 1}{2} M^2\right]^{\frac{-\gamma}{\gamma-1}}. \tag{6.6}$$

6.1.2 Application

Using the same geometry and mesh described in Chapter 4, two Reynolds-Averaged Navier-Stokes (RANS) simulations were conducted in STAR-CCM+. The first RANS was run at NPR = 1.39 with TTR = 1 to match the conditions of the LES described in Chapter 5. The second RANS was run at NPR = 1.35 with TTR = 1 to simulate losses in the nozzle such as those resulting from the addition of a mixer. The exit velocity and the thrust value obtained for each nozzle are shown in Table 6.1.

Table 6.1: Mass flow rate, exit velocity, and thrust values

NPR	Mass flow rate (kg/s)	Exit velocity (m/s)	Thrust (N)
1.39	0.4195	208.75	87.57
1.35	0.3974	200.13	79.53

The mass flow rate obtained from experimental data for a nozzle with NPR = 1.39, TTR = 1 was 0.4057 kg/s, so the mass flow rates given by the simulation show good agreement with physical values. As expected, the nozzle run at NPR = 1.35 has a lower mass flow rate and exit velocity, resulting

in a 9.18% decrease in thrust compared to the nozzle run at NPR = 1.39. This nozzle (assuming the two were initially run at the same NPR and the change in thrust was due to the addition of a mixer) would need to be run at a higher NPR to increase the velocity and match the thrust value of the nozzle without the mixer. Doing so would also affect its acoustic output. Instead of running a second large-eddy simulation to obtain the new acoustic data, the acoustic data on hand can be normalized to match the necessary thrust basis.

6.2 Acoustic Normalization

This section describes the procedure with which one can normalize two nozzles to the same thrust basis and adjust the acoustic data to match. First, the acoustic results for an LES run at NPR = 1.35 are compared to those seen in Chapter 5. Then, the method of adjusting the thrust basis and normalizing the acoustic data is discussed. Finally, the adjusted acoustic data are then compared to the data collected at NPR = 1.39.

6.2.1 Results for Comparison

The unadjusted results from the NPR = 1.35 LES are compared to the original NPR = 1.39 LES below. The power spectral density (PSD) is given first, then the overall sound pressure level (OASPL).

6.2.1.2 Power Spectral Density

The PSD at a receiver distance of 100 jet radii at 30^0 and 90^0 is shown in Figure 6.2 and Figure 6.3, respectively. As expected, the PSD value for the NPR = 1.35 nozzle is lower on average than the PSD value for the NPR = 1.39 nozzle at both azimuthal angles but shows the same behavioral trends at the downstream and sideline angles.

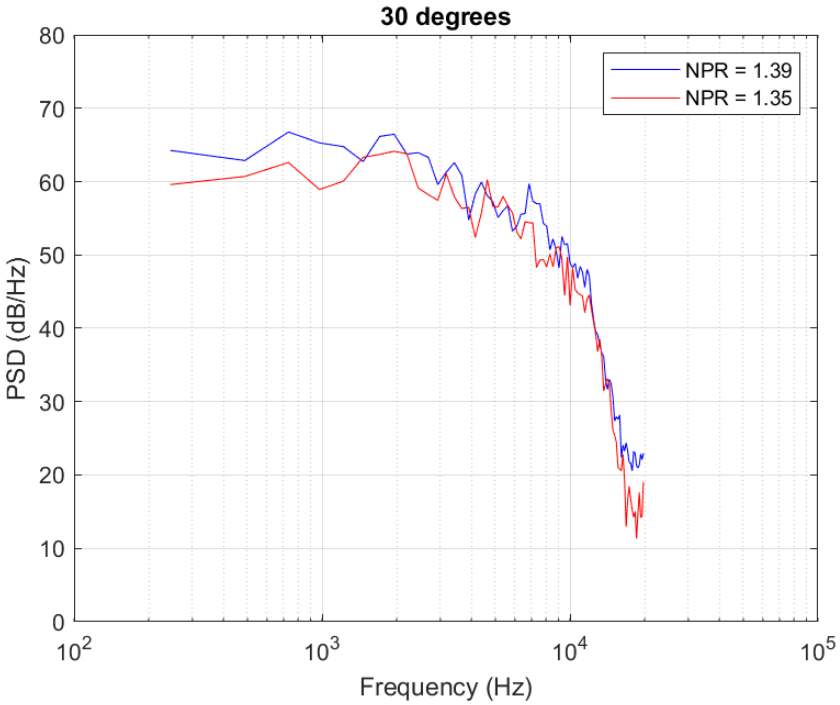

Figure 6.2: PSD at 100r, 30^0 for NPR = 1.39 and NPR = 1.35

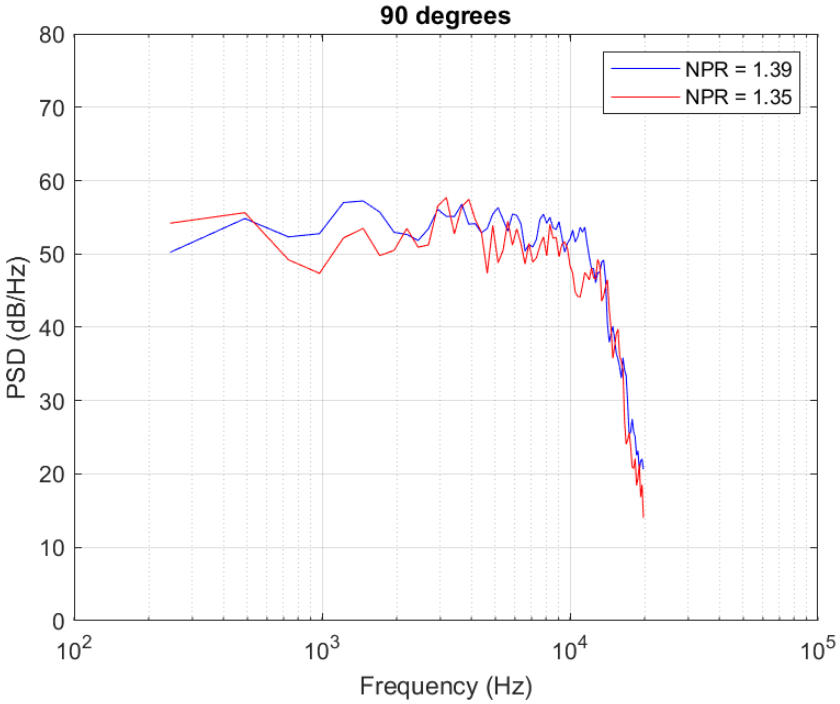

Figure 6.3: PSD at 100r, 90^0 for NPR = 1.39 and NPR = 1.35

6.2.1.2 Overall Sound Pressure Level (OASPL)

Figure 6.4 shows the OASPL at receiver locations 50 and 100 jet radii away from the nozzle exit for both NPR = 1.39 and NPR = 1.35. The average difference in the OASPL at 50r was 1.45 dB. The average difference in the OASPL at 100r was 2.04 dB, but that difference is weighted due to the increase in the difference observed in the downstream angles closer to the jet flow. Between the azimuthal angles of 110^0 and 60^0, the difference in the OASPL at 100r was 1.43 dB.

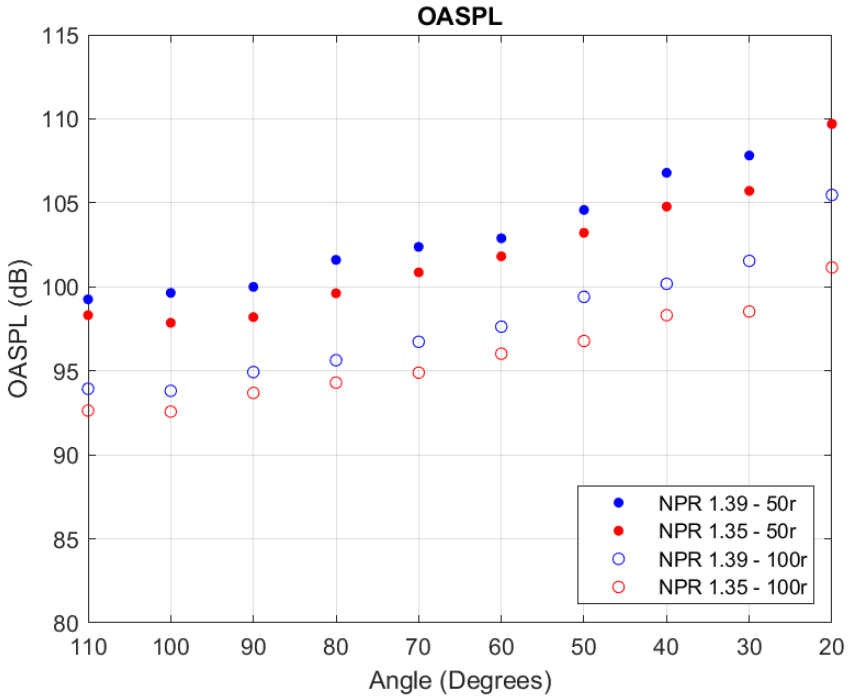

Figure 6.4: OASPL at 50r and 100r for NPR = 1.39 and NPR = 1.35

6.2.2 Procedure

The process of adjusting the acoustic data to a similar thrust basis is threefold. First, the increase in velocity needed to recover the thrust value obtained from a nozzle with a higher mass flow rate must be found. Then, an acoustic scaling law developed by Viswanathan [147] is applied to the sound pressure level (SPL) at the original velocity and the calculated increased velocity. Finally, the difference between the SPLs obtained from the scaling law is applied to the original SPL to recover the losses.

6.2.2.1 Solving for Velocity

For the NPR = 1.35 nozzle to achieve an equal thrust value to the NPR = 1.39 nozzle, the nozzle must be given a higher exit velocity. The equation for thrust with respect to mass flow rate and velocity is

$$F_{TH} = \dot{m}V \tag{6.7}$$

where $\dot{m}$ is the mass flow rate and V is the velocity at the nozzle exit, not the full-expanded velocity. However, one must keep in mind that

$$\dot{m} = \rho V A \tag{6.8}$$

so the full equation to calculate the thrust is

$$F_{TH} = \rho V^2 A \tag{6.9}$$

where ρ is the fluid density and A is the nozzle exit area. Using the mass flow rate and velocity extracted from the NPR = 1.35 simulation, the density of the air can be found and held constant. The velocity value needed to match the thrust given by the NPR = 1.39 is then calculated, along with the new, resulting mass flow rate. Substituting the values from Table 6.*1* into Eqn. (6.9) gives an adjusted velocity value of 210 m/s for the NPR = 1.35 nozzle, with a corresponding mass flow rate of 0.4167 kg/s. These values are shown alongside the original values in Table 6.2.

Table 6.2: Adjusted mass flow rate and exit velocity values

NPR	Mass flow rate (kg/s)	Exit velocity (m/s)	Thrust (N)
1.39	0.4195	208.75	87.57
1.35	0.3974	200.13	79.53
ADJ	**0.4167**	**210.00**	**87.57**

6.2.2.2 Acoustic Scaling Law

Jet noise has historically been normalized to constant area, as that relationship has been known for some time [148,149]. Normalizing jet noise to thrust, however, requires a relationship between the noise and the exit velocity. In the 2000s, Viswanathan developed acoustic scaling laws that identified jet temperature ratio and acoustic Mach number as independent parameters [147,150–152]. From experiments, it was determined that the sound pressure level (SPL) is given by the product of a spectrum function and the velocity ratio raised to the velocity exponent n. For narrowband spectra, the scaling formulation is given as

$$SPL - 10\log_{10}\left(\frac{A}{A_{ref}}\right) - 10n\log_{10}\left(\frac{V_j}{a}\right) - 10\log_{10}\left(\frac{D_j}{V_j}\right) \tag{6.10}$$

where A is the nozzle exit area, A_{ref} is a reference area (taken here to be one square meter), V_j is the jet exit velocity, a is the speed of sound, D_j is the jet exit diameter, and n is the velocity exponent. Viswanathan took the velocity exponent n to be a unique value calculated as a function of angle and jet temperature ratio, but here n is simply taken to be a value of 8, from the eighth-power velocity scaling law also seen in Eqn. (1.10).

6.2.2.3 Scaling Law Application

To adjust the acoustic data from the NPR = 1.35 simulation, the SPL (in dB) is substituted into Eqn. (6.10) twice. V_j is first taken to be the jet exit velocity obtained from the NPR = 1.35 simulation, then taken to be the value calculated in Section 6.2.2.1. The difference between the two results is then added to the original (NPR = 1.35) SPL to calculate the adjusted SPL for the calculated velocity. The results of this procedure are shown in the next section.

6.2.3 Normalized Results

The results obtained from the application of the scaling law given in Eqn. (6.10) are shown below. The sound pressure level (SPL) is given first, followed by the power spectral density (PSD).

6.2.3.1 Sound Pressure Level (SPL)

The scaling law increased the SPL by 1.46 dB across all azimuthal angles. The overall sound pressure level (OASPL) for both 50r and 100r from the nozzle exit are given in Figure 6.5. At 50r, there was an average 1.45 dB difference between the NPR = 1.39 and the NPR 1.35 simulations. At 100r, the average difference was 2.04 dB, with a larger difference at downstream angles than at the sideline angles. The OASPL, like the SPL given in Section 6.2.3.1, was increased by 1.46 dB across all azimuthal angles with the application of the scaling law. The average difference between the NPR = 1.39 OASPL and the adjusted NPR = 1.35 OASPL was 0.00625 dB and 0.57 dB for 50r and 100r, respectively. These adjusted values show good agreement with the original OASPL.

This demonstrates that, though the lower NPR case—which simulates the presence of an internal mixer—gives a lower OASPL, this benefit is eliminated when an adjustment is made for equal thrust.

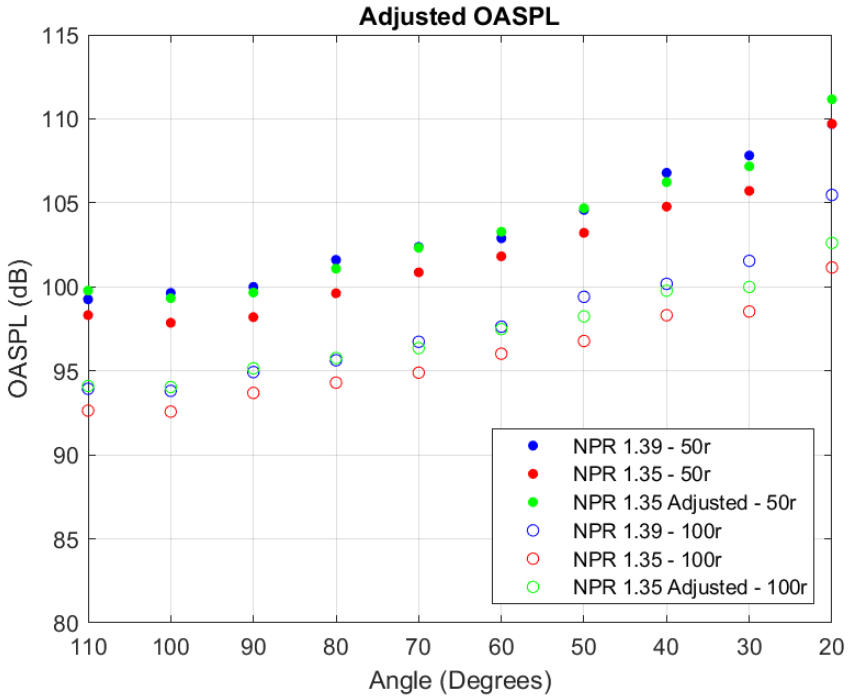

Figure 6.5: OASPL at 50r and 100r from nozzle exit

6.2.3.2 Power Spectral Density (PSD)

The 1.46 dB increase in SPL gained by the application of the scaling law can also be seen in the PSD. The Power Spectral Densities for 100r at 30^0 and 90^0 are shown in Figure 6.6 and Figure 6.7, respectively. The adjusted NPR = 1.35 PSD recovers some of the difference between the NPR = 1.39 PSD and the original NPR = 1.35 PSD. As in the case of the OASPL, there is no noise benefit from the 'mixer nozzle' when the noise is adjusted for equal thrust.

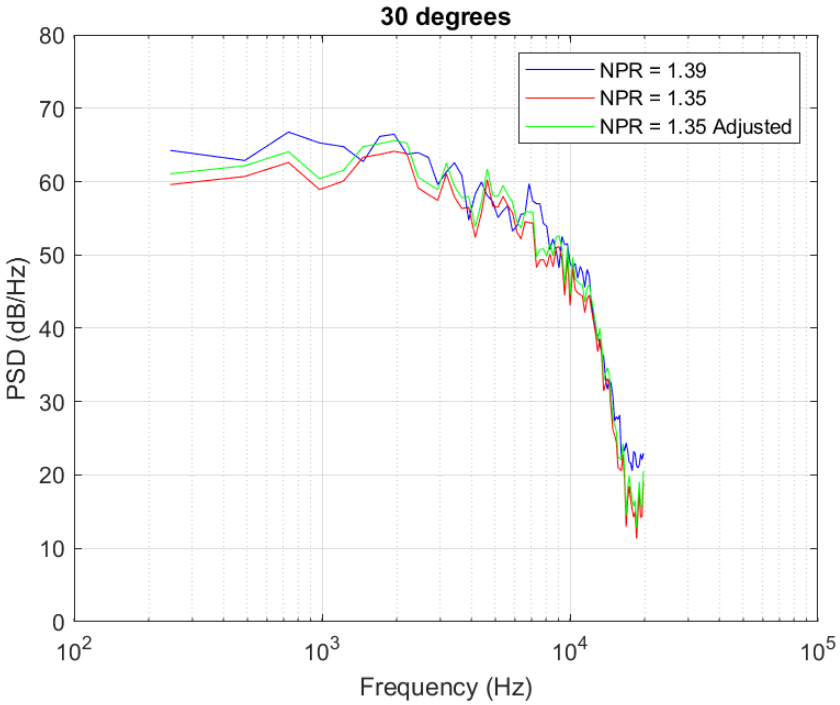

Figure 6.6: PSD for 30^0 at 100r from nozzle exit

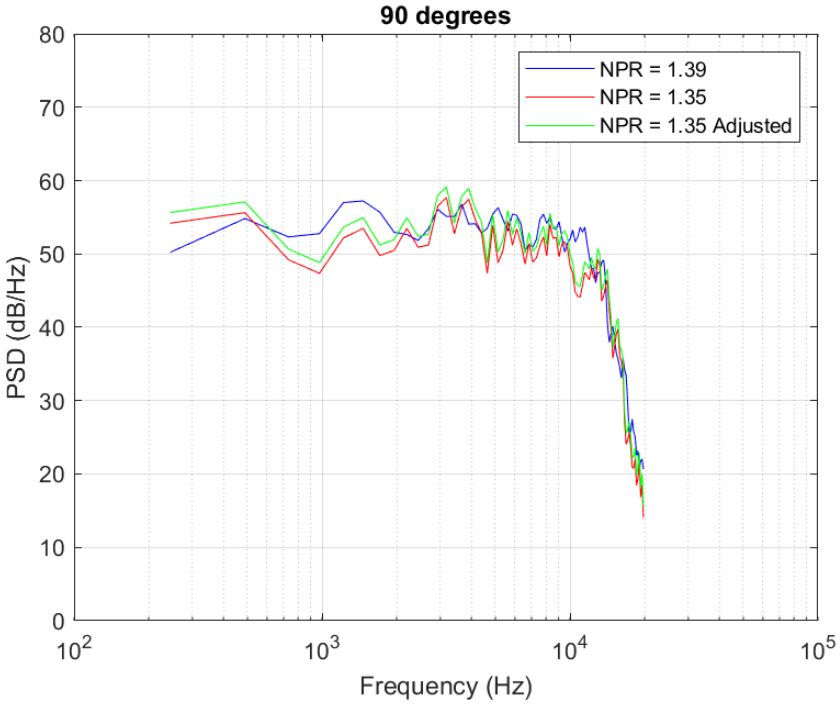

Figure 6.7: PSD for 90^0 at 100r from nozzle exit

Chapter 7 will review the findings from this thesis and discuss recommendations for future studies. Appendix A contains all the acoustic data obtained and discussed in Chapter 5, followed by the references.

Chapter 7

Conclusions and Future Work

Although the use of Large-Eddy Simulation (LES) for jet noise problems has been studied since the late 1990s, it's only been within the last ten years that the use of LES has been brought into the realm of industry studies. Improvements in areas such as geometry modeling, spatial discretization, turbulence modeling, and far-field noise propagation, along with improvements in high-performance computing such as the introduction of GPU acceleration, have made computationally intensive problems both more manageable and more accurate.

The goal of this thesis was three-fold. The first goal was to further reduce computation expense by developing a method of grid generation grounded in the turbulent energy spectrum that minimized guesswork and trial and error. The second goal was to establish a method of normalizing two nozzles with different thrust outputs to the same thrust basis to achieve more relevant acoustic comparisons. The third, overarching goal of this thesis was to assess the capability of a commercial CFD package for LES jet noise problems.

7.1 Jet Noise Simulations and Findings

The commercially-available CFD package STAR-CCM+ by Siemens was used throughout this thesis. The grid contained 62.7 million cells, with the greatest cell density concentrated around the shear layer. The simulation was run at NPR = 1.39, TTR = 1.0 for an exit Mach number of approximately 0.7. The velocity and turbulence intensity statistics obtained on the lipline and centerline were slightly underpredicted in a manner consistent with previous literature. Acoustic results were extended to the far-field using Farassat's formulation 1-A of the FW-H analogy. Noise prediction locations were limited due to the size and shape of the domain but showed good agreement with experimental measurements where obtained. Application of an acoustic scaling law to a simulation run

at NPR = 1.35, TTR = 1.0 to simulate losses in the nozzle, such as those resulting from the addition of a mixer, successfully recovered those losses to show good agreement with the data obtained from the NPR = 1.39 simulation.

7.1.1 Use of the Energy Cascade to Determine Grid Resolution

A RANS calculation was performed on an initial, arbitrary grid, from which the mixing length and the Taylor microscale length were extracted along the shear layer. These length scales were normalized by the corresponding local grid length, which was obtained by taking the cube root of the polyhedral cell volume. Using the grid length at the nozzle exit as a basis, the grid lengths necessary to resolve the mixing length and the Taylor microscale were calculated, then plotted alongside the grid lengths present in the simulations.

The goal of this research was to resolve up to 80% of the total kinetic energy. The corresponding critical wavenumber that defined the grid cell lengths was found by taking the integral of the energy spectrum with respect to the wavenumber. It was found that the initial grid was biased too close to the Taylor microscale, and thus resolving more small-scale structures and a larger fraction of the total energy, so the grid length was increased to position the grid more evenly between the mixing length and the Taylor microscale length.

A MATLAB script was written to calculate a sample Pao energy spectrum using the mixing, Taylor microscale, and Kolmogorov length scales extracted from STAR-CCM+. The wavenumbers associated with these length scales, along with the wavenumbers associated with the resolution of 80% of the total kinetic energy and the grid lengths, were plotted over top of the sample energy spectrum. At the x/D locations of approximately 5 and 10, the wavenumber for the grid length fell between the 80% wavenumber and the Taylor microscale wave number on both the centerline and the lipline. This indicated that the target of resolving 80% of the total kinetic energy was met and exceeded; however,

the turbulence statistics remained slightly underpredicted to experimental data, likely due to dissipation in the code itself.

7.1.2 Viability of Commercial Software for Jet Noise Problems

Both the flow field and acoustic data obtained from STAR-CCM+ showed good agreement with experimental results. The underprediction of the velocity and turbulence statistics were consistent with previous literature that conducted large-eddy simulations using different CFD codes. The acoustic data followed the scaling laws of a 6 dB reduction per doubling of distance. From a purely statistical point of view, STAR-CCM+ gave acceptable results; however, the amount of time it took to conduct the simulation (12 days, with a total CPU time of 546,288 hours) was significant when compared to GPU-accelerated solvers, and the quality of the acoustic data would have benefited from an even longer run.

7.1.3 Thrust Normalization for Acoustic Analysis

Using the same geometry and mesh that was used for the previous studies, a second simulation was conducted in STAR-CCM+, first as a RANS and then as an LES. This second simulation was run at an NPR of 1.35 to simulate losses in the nozzle such as those resulting from the addition of a mixer. The mass flow rates and thrust values for both the NPR = 1.39 and NPR = 1.35 were obtained, and a calculation was performed to find the velocity at which the NPR = 1.35 nozzle would have needed to be run to recover an equivalent thrust value to the NPR = 1.39 nozzle.

An acoustic scaling law by Viswanathan [147] was then applied to the SPL from the NPR = 1.35 simulation, using first the original velocity, and then the corrected velocity. The 1.46 dB difference between the two SPL values obtained from the formulation was then added to the original SPL values to recover the 'losses.' The adjusted NPR = 1.35 SPL values showed good agreement with the NPR = 1.39 SPL values. The application of the scaling law resulted in an average difference of less than 1 dB

between the NPR = 1.39 and the adjusted NPR = 1.35 OASPL values at radial distances of both 50 jet radii and 100 jet radii, successfully recovering the 'losses' simulated by the lower NPR.

7.2 Review of Original Contributions

The key takeaways of the present work are as follows:

- The turbulent energy spectrum provides an effective benchmark around which to develop a grid for large-eddy simulations, eliminating costly trial-and-error.
- Commercial CFD software is unwieldy and time consuming when used for LES jet noise problems, especially if it is not GPU-accelerated, but provides good agreement with experimental data.
- Viswanathan's [147] scaling law is a potential method for normalizing the acoustic data from two different jets to an equal thrust basis for better practical comparison in industry.

7.3 Recommendations for Future Work

This thesis introduces novel methods for LES grid generation for jet noise and the adjustment of acoustic data to meet a normalized thrust basis with encouraging results for each. However, further work with these methods is required.

The development of the LES grid using the energy cascade showed promising results in STAR-CCM+. The same method should be used in other CFD software to prove its robustness as a grid generation method. This thesis overlaid the wavelengths corresponding to the grid length, 80% resolution, and assorted length scales atop a model Pao spectrum. In the future, unique energy spectrums should be calculated using the length scales extracted from the simulation. Additionally, further investigation should be conducted into the underprediction of the turbulence intensity statistics.

The original scope of this thesis called for the scaling of the grid to be two and four times coarser. LES was to be run at each grid refinement level, and the acoustic data compared to further investigate the relationship between the accuracy of the data and the refinement of the grid. The goal was to, in future work, develop a hybrid method using a coarse grid for the LES that resolved only the large-scale, low-frequency downstream noise and an analytic acoustic analogy method to calculate the high-frequency sideline data. This is an avenue still worth pursuing, as a coarser mesh would result in a further decrease in computational time and may provide better agreement with experimental acoustic data on the sideline.

The method of acoustic adjustment using the scaling laws given by Viswanathan [147] showed promise in recovering the 'losses' between the same nozzle run at different NPRs. The work conducted for this thesis should be repeated for other nozzle geometries at differing NPRs, as well as simulations run at the same NPR with differing geometries. It should also be conducted for simulations run at differing temperature ratios. In Viswanathan's work, the velocity exponent is variable, dependent on the angle and temperature ratio. This work simply took the velocity exponent to be 8, from the 8^{th} power scaling law, so future work should calculate the velocity exponent more accurately. Finally, this adjustment method could also be applied to experimental data, as it does not use data that is obtainable exclusively from simulations.

Appendix

LES Acoustic Data

This appendix contains all the acoustic data obtained from the LES. It is organized first in A.1 by all PSD curves at each radial distance for individual azimuthal angles, then in A.2 by all PSD curves at each azimuthal angle for individual radial distances. Appendix A.3 contains the OASPL for each radial distance. The charts in A.1 and A.2 are zoomed in to better show the area of interest due to the number of curves on each chart.

A.1 By Degree

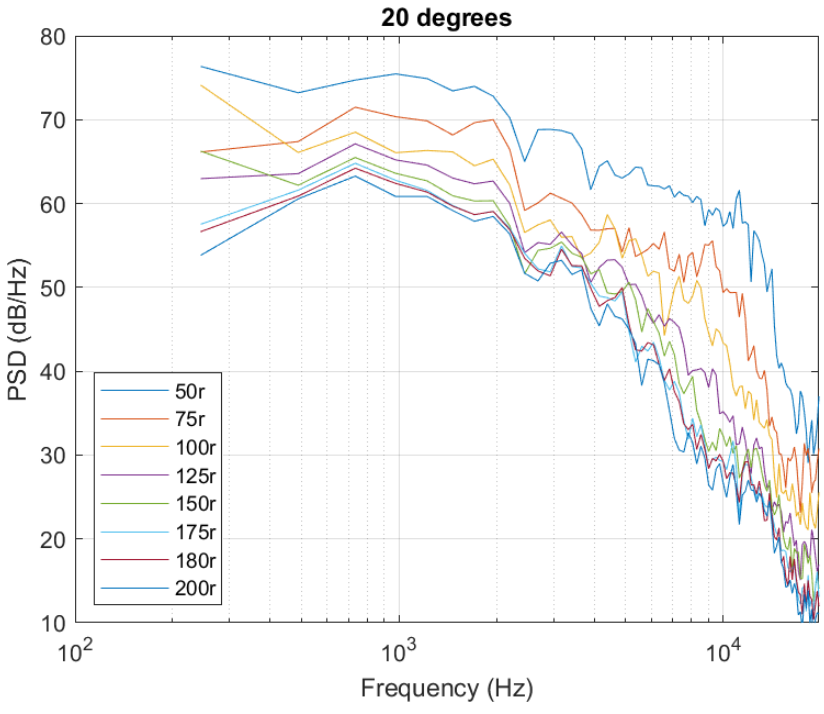

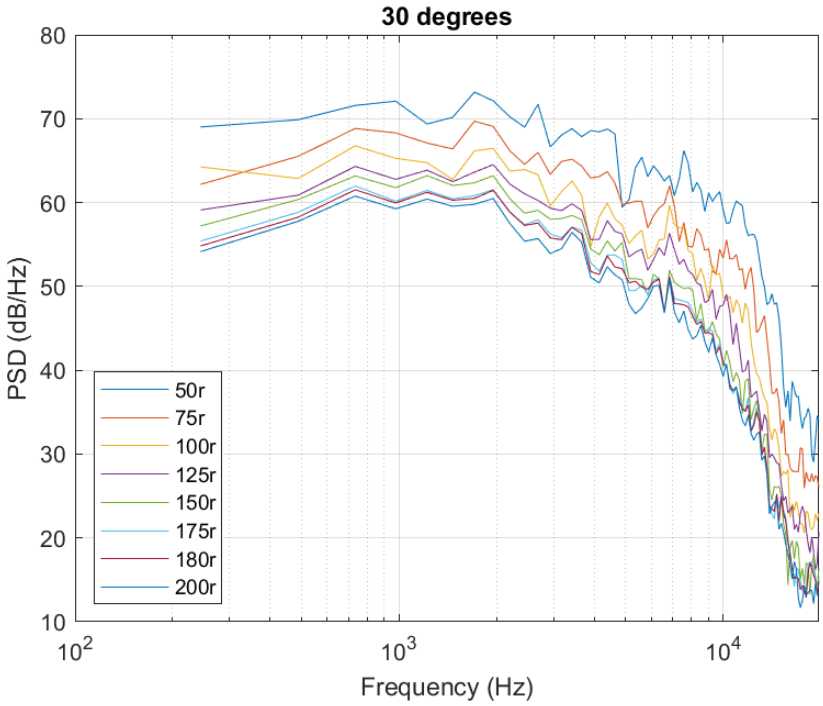
30 degrees
PSD (dB/Hz)
Frequency (Hz)
50r
75r
100r
125r
150r
175r
180r
200r

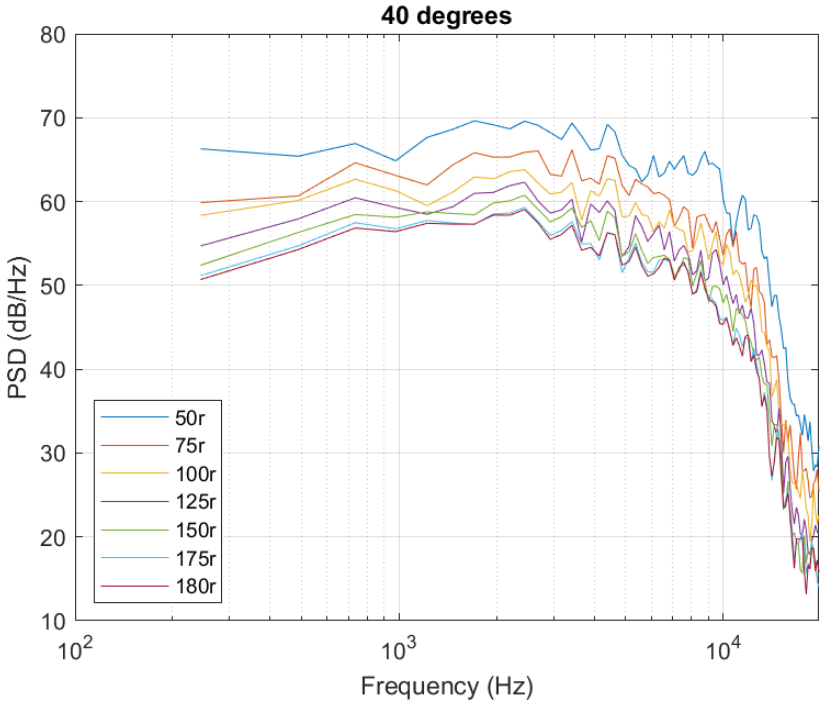
40 degrees
PSD (dB/Hz)
Frequency (Hz)
50r
75r
100r
125r
150r
175r
180r

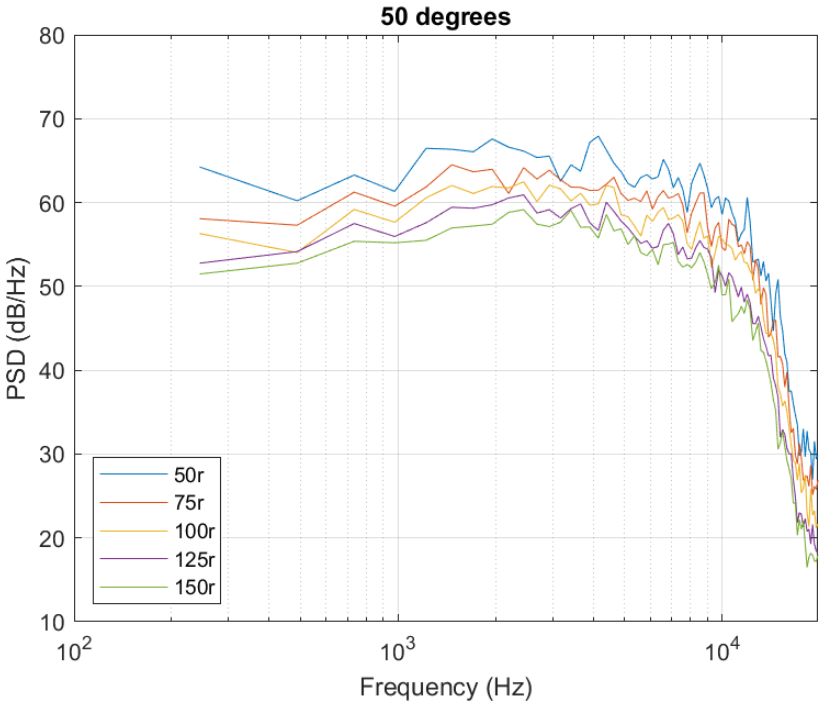
50 degrees
PSD (dB/Hz)
Frequency (Hz)
50r
75r
100r
125r
150r

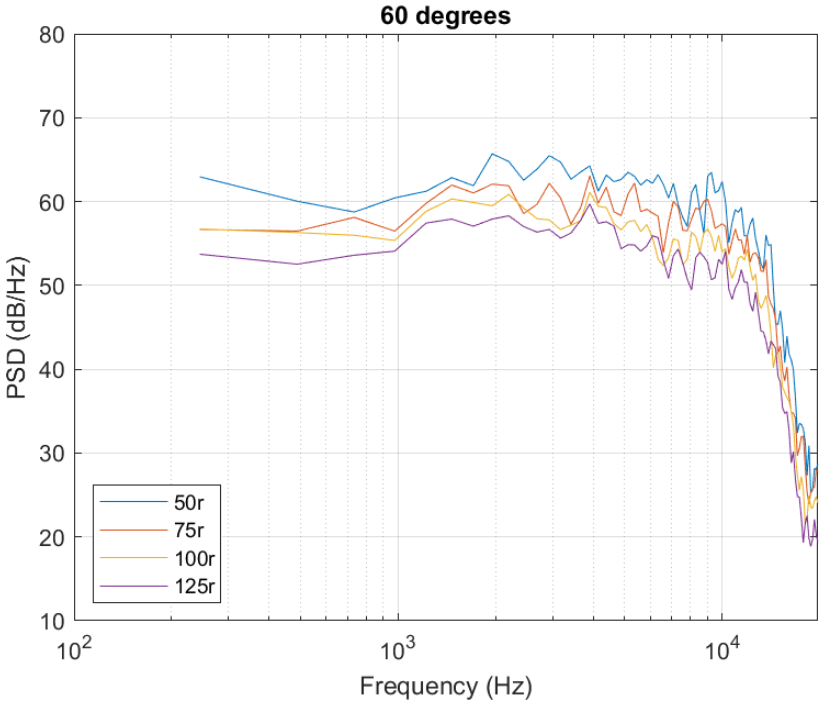
60 degrees
PSD (dB/Hz)
Frequency (Hz)
50r
75r
100r
125r

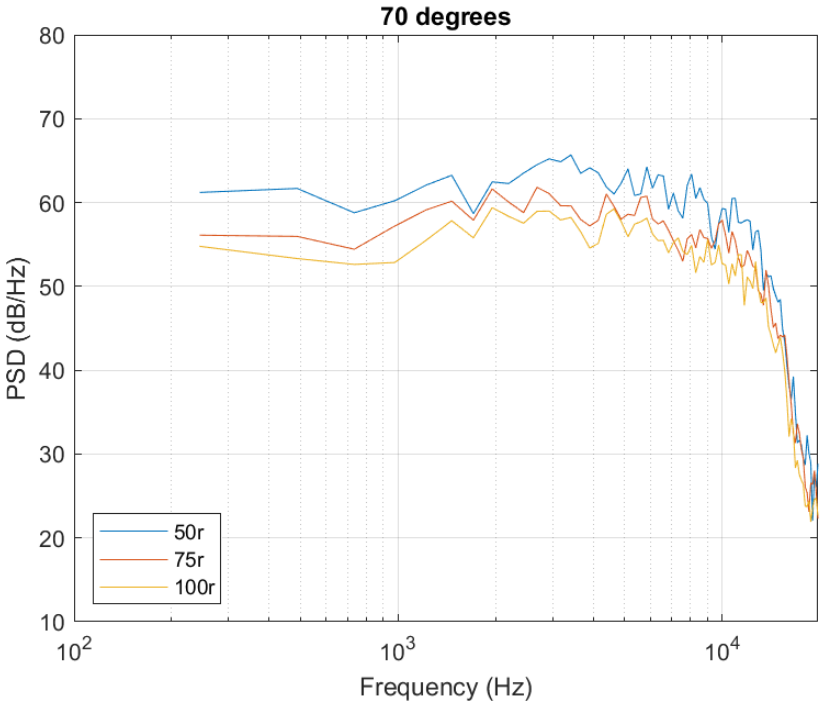
70 degrees
PSD (dB/Hz)
Frequency (Hz)
50r
75r
100r

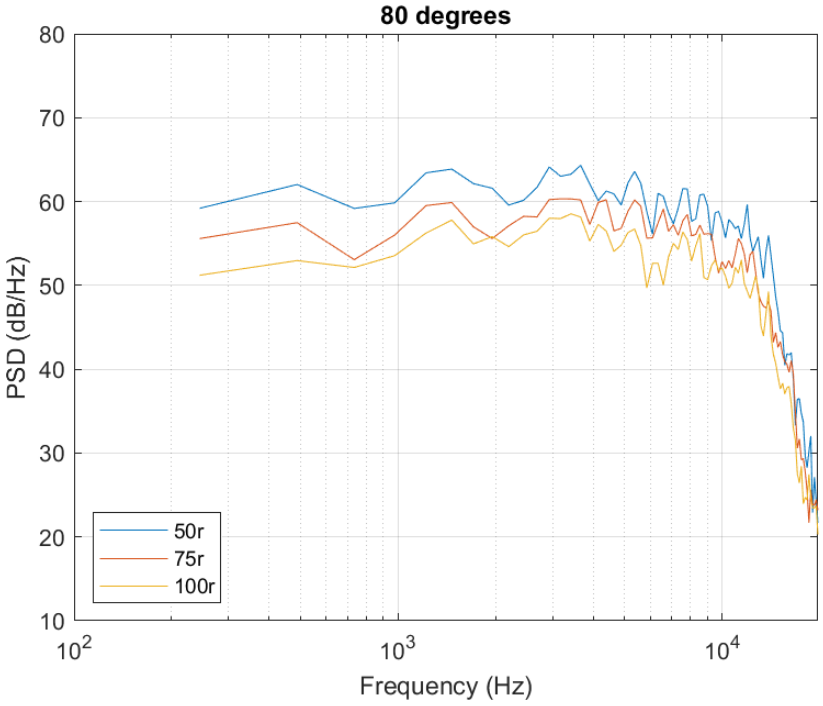
80 degrees
PSD (dB/Hz)
Frequency (Hz)
50r
75r
100r

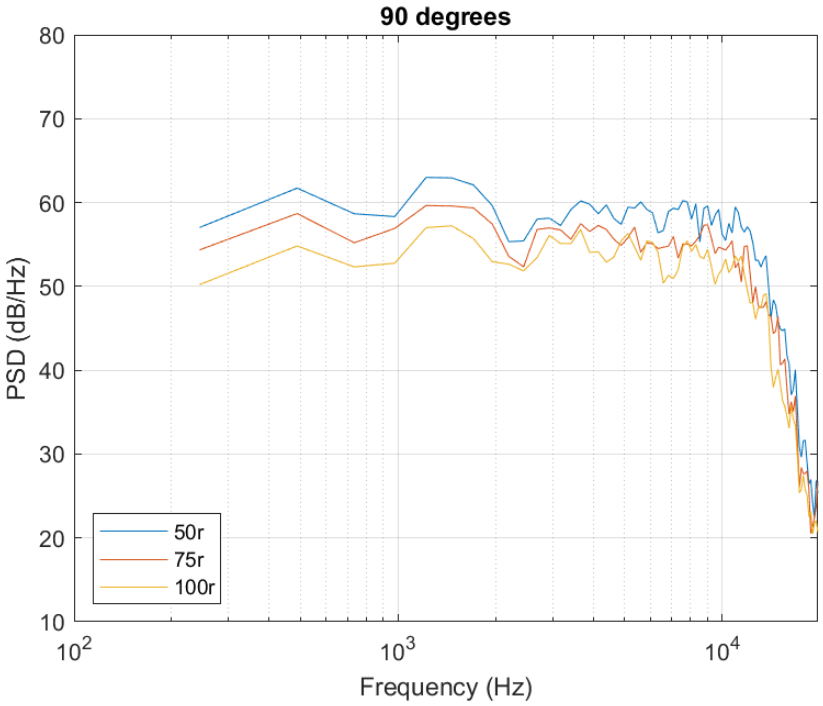
90 degrees
PSD (dB/Hz)
Frequency (Hz)
50r
75r
100r

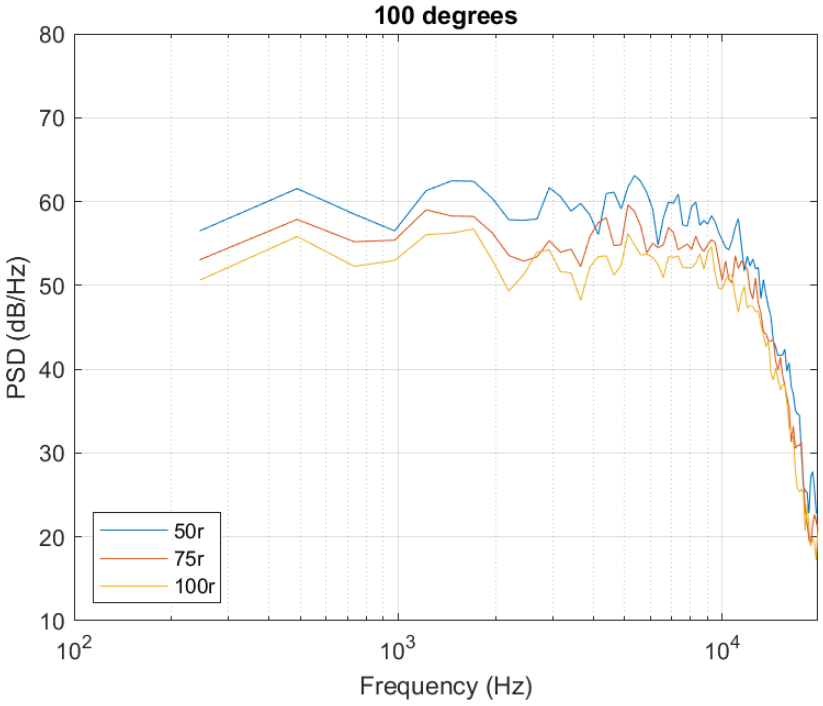
100 degrees
PSD (dB/Hz)
Frequency (Hz)
50r
75r
100r

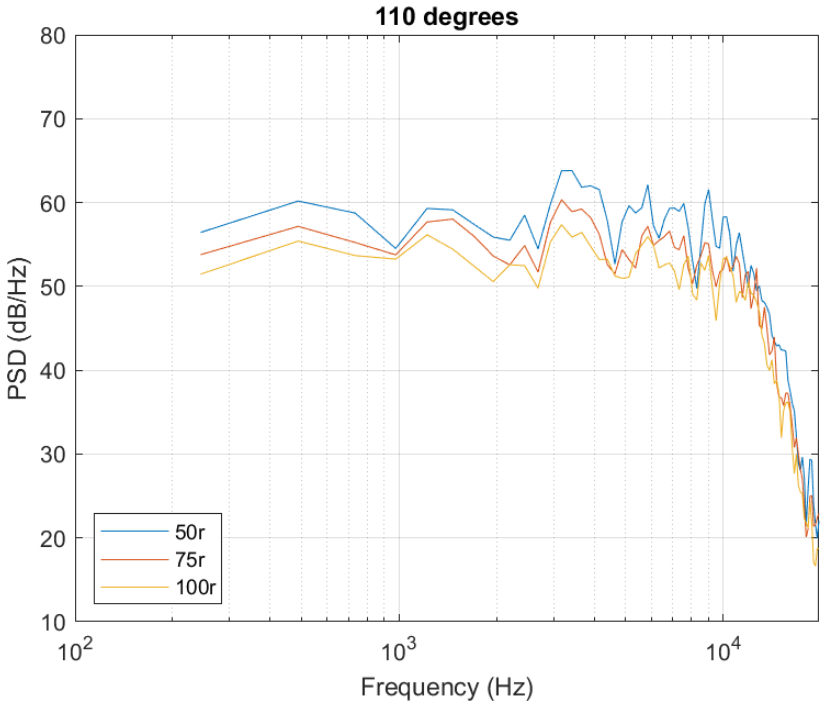
110 degrees
PSD (dB/Hz)
Frequency (Hz)
50r
75r
100r

A.2 By Radius

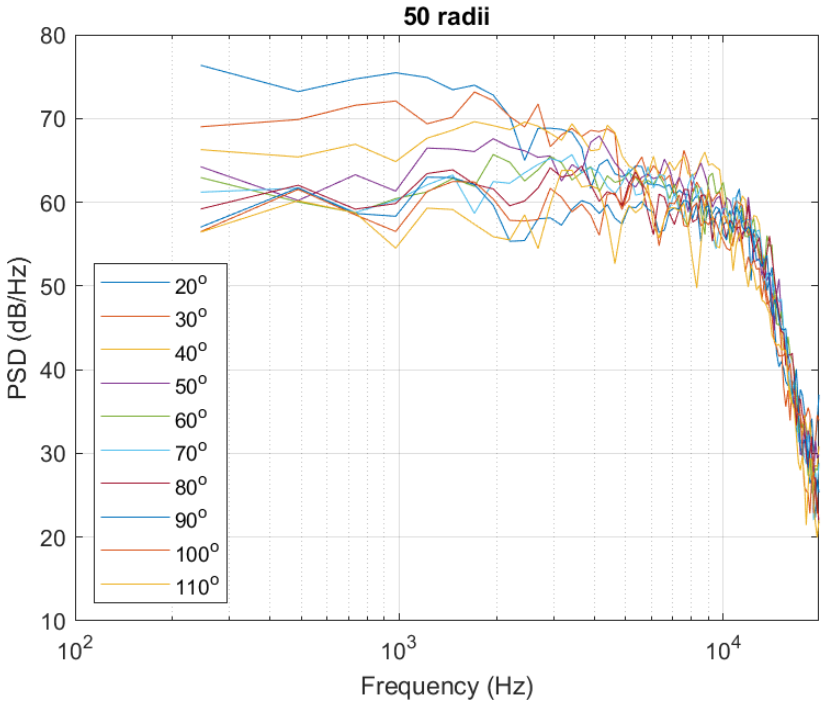
50 radii
PSD (dB/Hz)
Frequency (Hz)
20°
30°
40°
50°
60°
70°
80°
90°
100°
110°

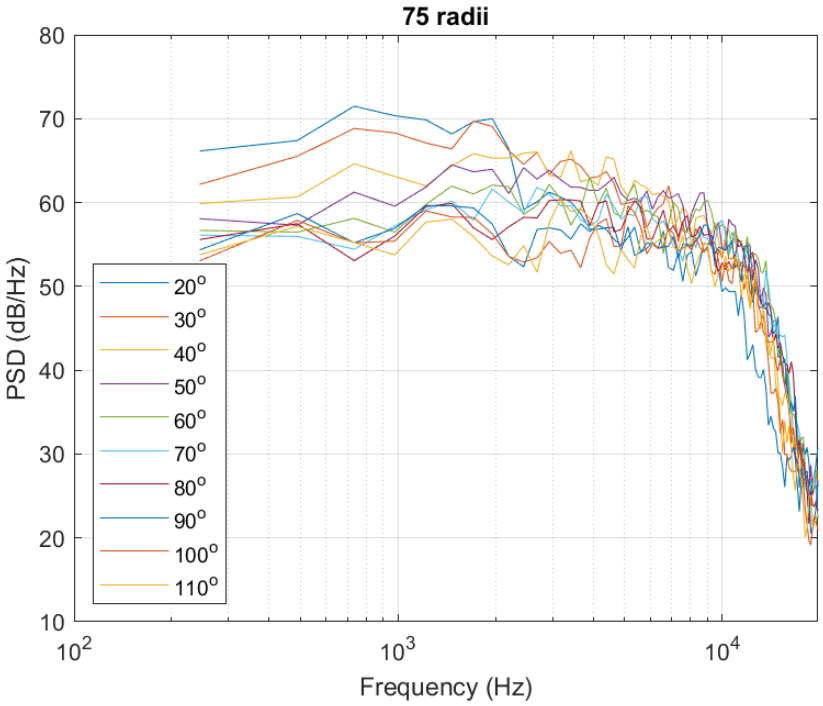
75 radii
PSD (dB/Hz)
Frequency (Hz)
20°
30°
40°
50°
60°
70°
80°
90°
100°
110°

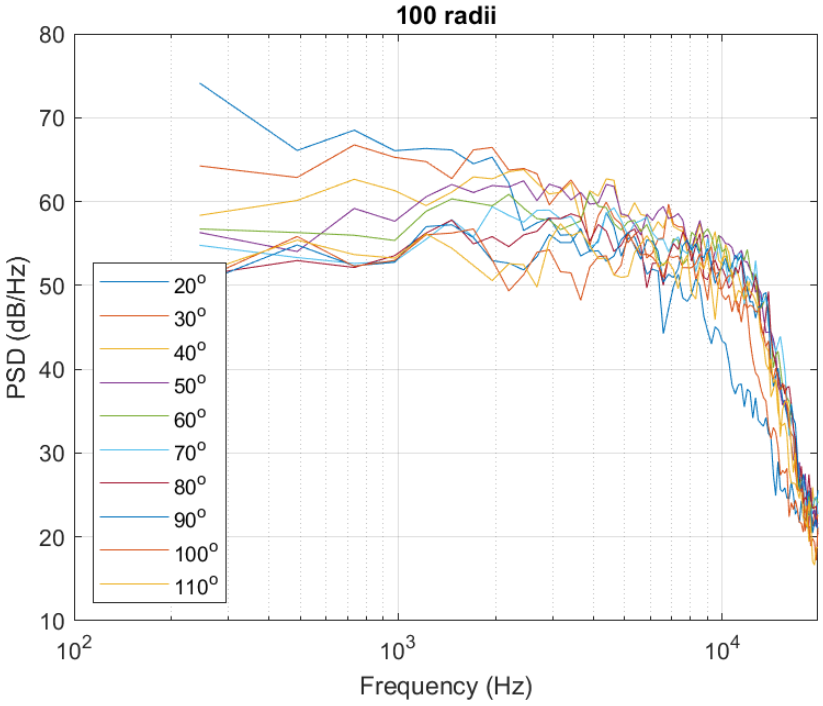
100 radii
PSD (dB/Hz)
Frequency (Hz)
20°
30°
40°
50°
60°
70°
80°
90°
100°
110°

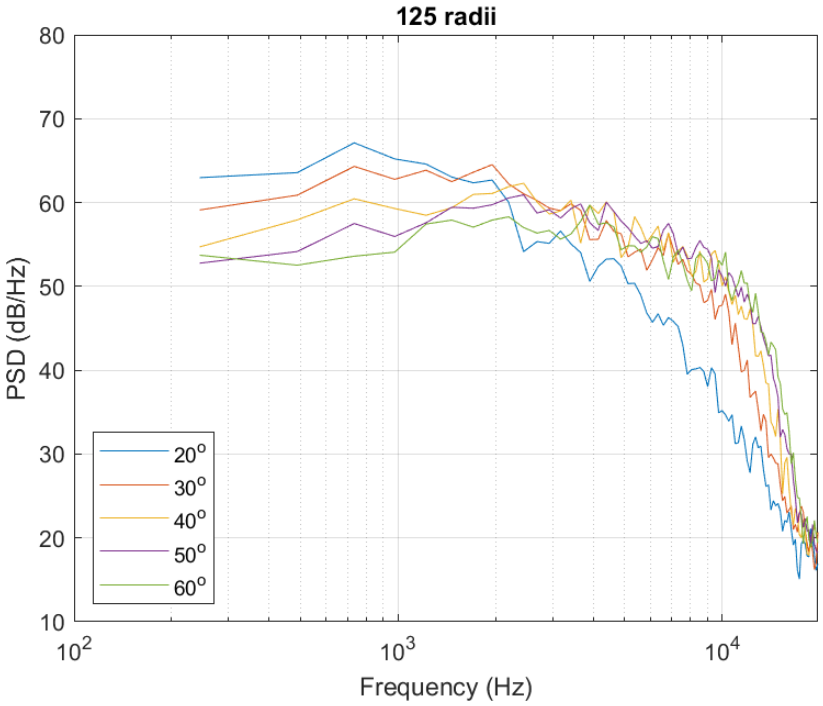
125 radii
PSD (dB/Hz)
Frequency (Hz)
20°
30°
40°
50°
60°

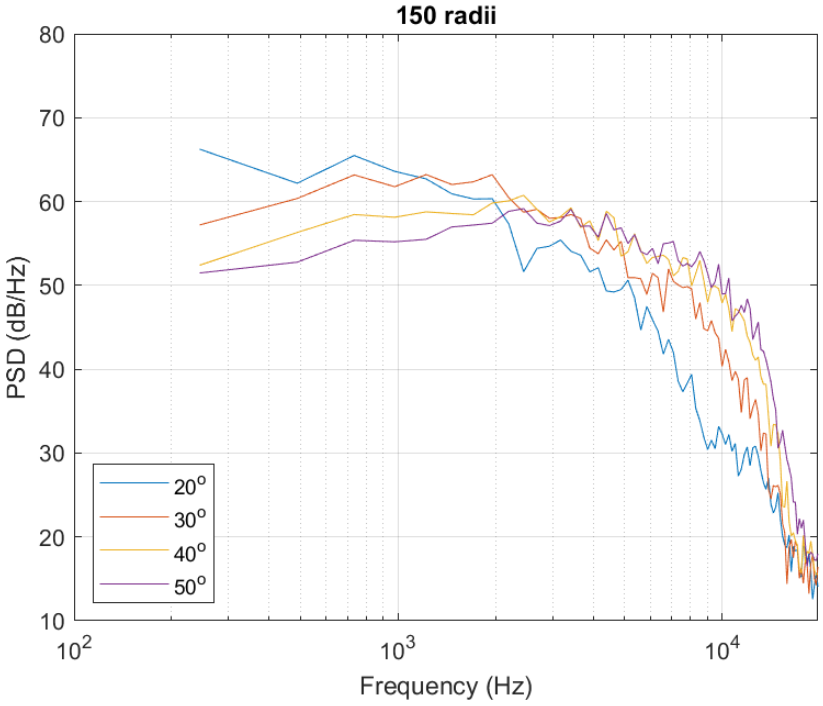
150 radii
PSD (dB/Hz)
Frequency (Hz)
20°
30°
40°
50°

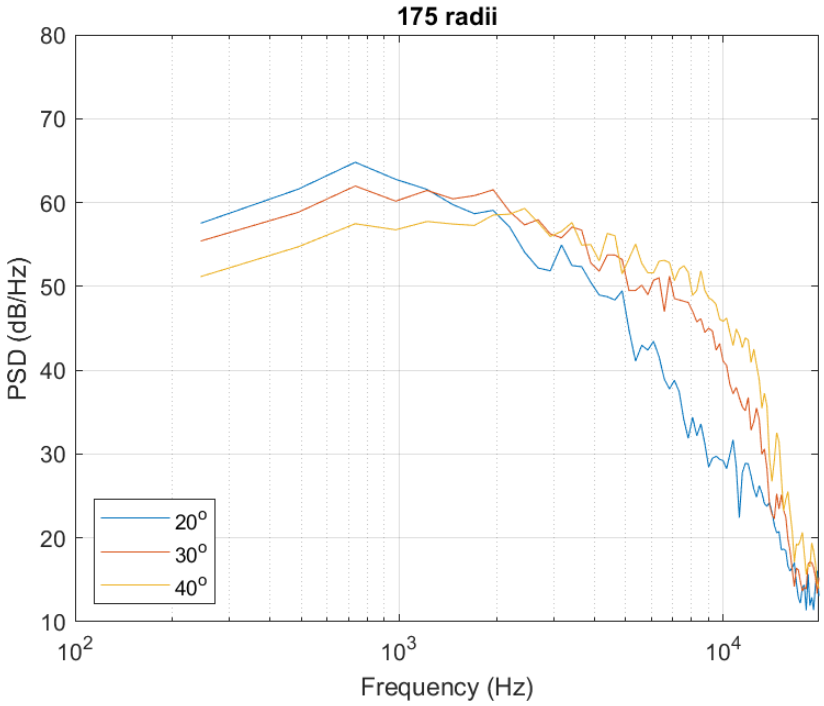
175 radii
PSD (dB/Hz)
Frequency (Hz)
20°
30°
40°

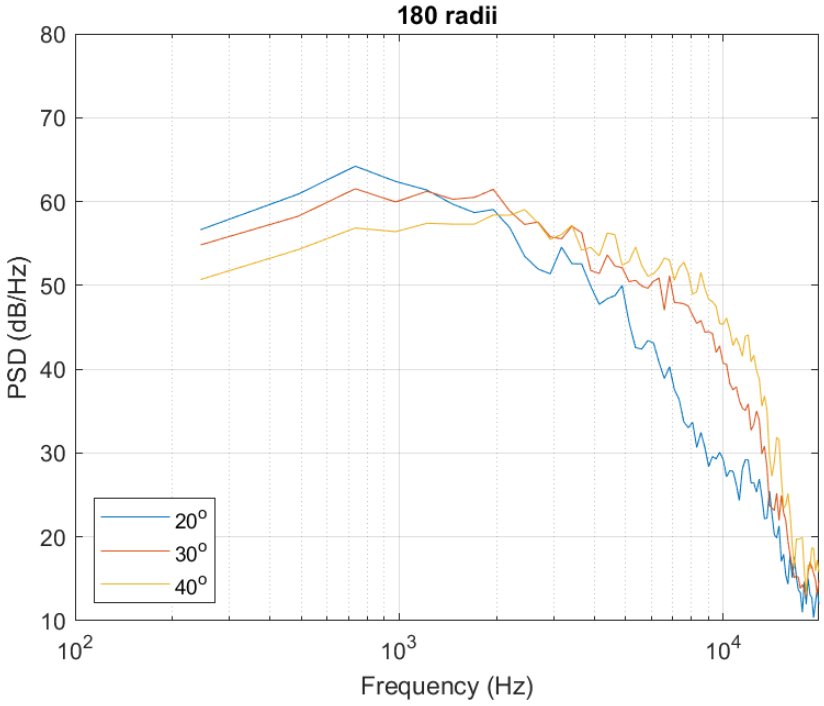
180 radii
PSD (dB/Hz)
Frequency (Hz)
20°
30°
40°

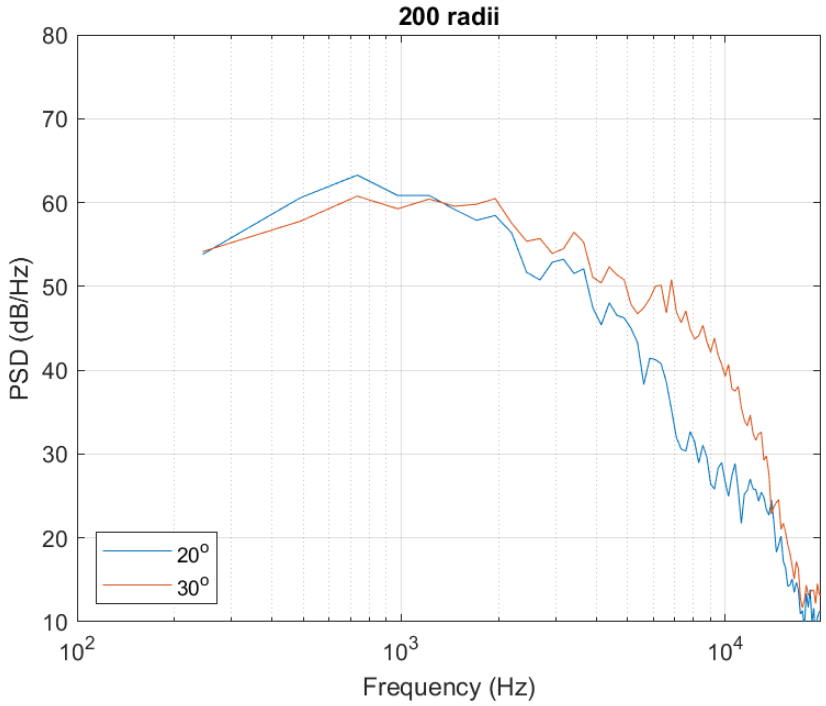

A.3 Over-All Sound Pressure Levels

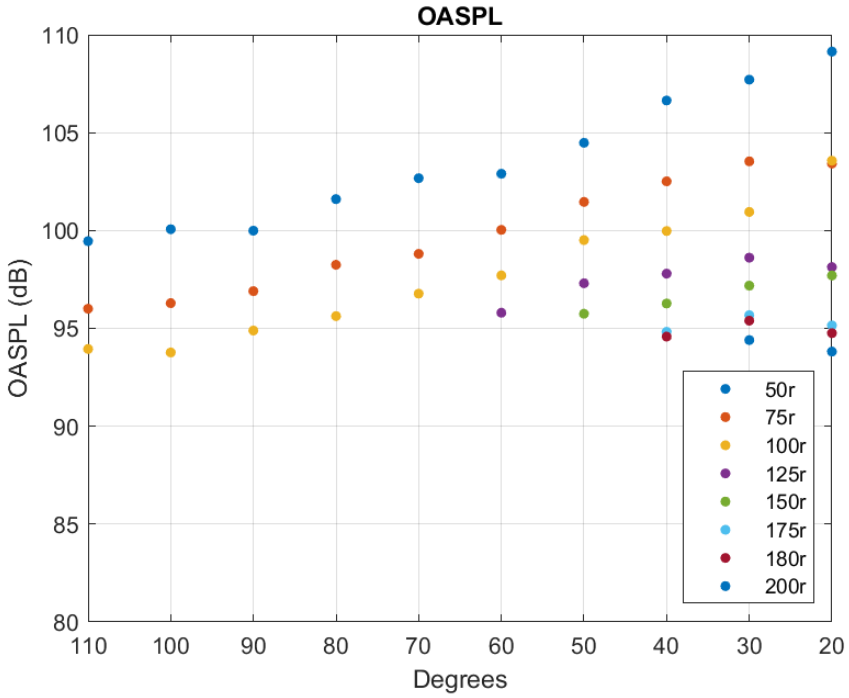

REFERENCES

[1] Westley, R., and Lilley, G. M., "An Investigation of the Noise Field from a Small Jet and Methods for Its Reduction.," College of Aeronautics Report No. 53, 1952.

[2] Lassiter, L. W., and Hubbard, H. H., "Experimental Studies of Noise from Subsonic Jets in Still Air," NACA Technical Note 2757, 1952.

[3] Lassiter, L. W., and Hubbard, H. H., *The Near Noise Field of Static Jets and Some Model Studies of Devices for Noise Reduction*, Vol. 3187, National Advisory Committee for Aeronautics, 1954.

[4] Lighthill, M. J., "On Sound Generated Aerodynamically I. General Theory," *Proceedings of the Royal Society of London. Series A. Mathematical and Physical Sciences*, Vol. 211, No. 1107, 1952, pp. 564–587.

[5] Trost, R. P., and Shaw, G. B., "Statistical Analysis of Hearing Loss among Navy Personnel," *Military Medicine*, Vol. 172, No. 4, 2007, pp. 426–430.

[6] Doychak, J., "Department of Navy Jet Noise Reduction Project Overview," Tech. rep., Office of Naval Research, Arlington VA, 2010.

[7] Prasad, C., "Simulation of Supersonic Jet Noise Reduction Using Fluid Inserts for Low Bypass Ratio Turbofans," PhD Thesis, Pennsylvania State University, 2019.

[8] Bodony, D. J., "Aeroacoustic Prediction of Turbulent Free Shear Flows," PhD Thesis, Stanford University, 2004.

[9] Rayleigh, L., "The Theory of Sound," Vol. 1, Dover Publications, 1894.

[10] Glegg, S., and Devenport, W., "Aeroacoustics of Low Mach Number Flows: Fundamentals, Analysis, and Measurement," 1st Edition, Elsevier Inc., 2017.

[11] Crighton, D. G., "Basic Principles of Aerodynamic Noise Generation," *Progress in Aerospace Sciences*, Vol. 16, No. 1, 1975, pp. 31–96.

[12] Laurence, J. C., "Intensity, Scale, and Spectra of Turbulence in Mixing Region of Free Subsonic Jet," NACA Report No. 1292, 1956.

[13] Davies, P., Fisher, M. J., and Barratt, M. J., "The Characteristics of the Turbulence in the Mixing Region of a Round Jet," *Journal of Fluid Mechanics*, Vol. 15, No. 3, 1963, pp. 337–367.

[14] Bradshaw, P., Ferriss, D. H., and Johnson, R. F., "Turbulence in the Noise-Producing Region of a Circular Jet," *Journal of Fluid Mechanics*, Vol. 19, No. 4, 1964, pp. 591–624.

[15] Lighthill, M. J., "On Sound Generated Aerodynamically: II. Turbulence as a Source of Sound," *Proceedings of the Royal Society of London A*, Vol. 222, No. 1148, 1953, pp. 1–32.

[16] Ffowcs Williams, J. E., "The Noise from Turbulence Convected at High Speed," *Philosophical Transactions of the Royal Society of London. Series A, Mathematical and Physical Sciences*, Vol. 255, No. 1061, 1963, pp. 469–503.

[17] Lush, P. A., "Measurements of Subsonic Jet Noise and Comparison with Theory," *Journal of Fluid Mechanics*, Vol. 46, No. 3, 1971, pp. 477–500.

[18] Ahuja, K. K., "Correlation and Prediction of Jet Noise," *Journal of Sound and Vibration*, Vol. 29, No. 2, 1973, pp. 155–168.

[19] Tanna, H. K., "An Experimental Study of Jet Noise Part I: Turbulent Mixing Noise," *Journal of Sound and Vibration*, Vol. 50, No. 3, 1977, pp. 405–428.

[20] Hoch, R. G., Duponchel, J. P., Cocking, B. J., and Bryce, W. D., "Studies of the Influence of Density on Jet Noise," *Journal of Sound and Vibration*, Vol. 28, No. 4, 1973, pp. 649–668.

[21] Yu, J. C.-Y., "Investigation of the Noise Fields of Supersonic Axisymmetric Jet Flows," PhD Thesis, Syracuse University, 1971.

[22] Yu, J. C., and Dosanjh, D. S., "Noise Field of a Supersonic Mach 1.5 Cold Model Jet," *The Journal of the Acoustical Society of America*, Vol. 51, No. 5A, 1972, pp. 1400–1410.

[23] Norum, T. D., and Seiner, J. M., "Measurements of Mean Static Pressure and Far Field Acoustics of Shock Containing Supersonic Jets," NASA Technical Memorandum 84521, 1982.

[24] Seiner, J. M., Ponton, M. K., Jansen, B. J., and Lagen, N. T., "The Effects of Temperature on Supersonic Jet Noise Emission," Vol. 1, 1992, pp. 295–307.

[25] Harper-Bourne, M., "The Noise from Shock Waves in Supersonic Jets," *Agard-Cp-131*, Vol. 11, 1973, pp. 1–13.

[26] Seiner, J., and Norum, T., "Experiments of Shock Associated Noise of Supersonic Jets," *12th AIAA Fluid and Plasma Dynamics Conference,* 1979, pp. 1526.

[27] Seiner, J., and Norum, T., "Aerodynamic Aspects of Shock Containing Jet Plumes," *6th AIAA Aeroacoustics Conference,* 1980, pp. 965.

[28] Seiner, J. M., and Yu, J. C., "Acoustic Near-Field Properties Associated with Broadband Shock Noise," *AIAA Journal*, Vol. 22, No. 9, 1984, pp. 1207–1215.

[29] Yamamoto, K., Brausch, J. F., Balsa, T. F., Janardan, B. A., and Knott, P. R., "Experimental Investigation of Shock-Cell Noise Reduction for Single Stream Nozzles in Simulated Flight," NASA Contractor Report 3845, 1984.

[30] Powell, A., "The Noise of Choked Jets," *The Journal of the Acoustical Society of America*, Vol. 25, No. 3, 1953, pp. 385–389.

[31] Davies, M. G., and Oldfield, D. E. S., "Tones from a Choked Axisymmetric Jet. II. The Self Excited Loop and Mode of Oscillation," *Acta Acustica united with Acustica*, Vol. 12, No. 4, 1962, pp. 267–277.

[32] Sherman, P. M., Glass, D. R., and Duleep, K. G., "Jet Flow Field during Screech," *Applied Scientific Research*, Vol. 32, 1976, pp. 283–303.

[33] Rosfjord, T. J., and Toms, H. L., "Recent Observations Including Temperature Dependence of Axisymmetric Jet Screech," *AIAA Journal*, Vol. 13, No. 10, 1975, pp. 1384–1386.

[34] Norum, T. D., "Screech Suppression in Supersonic Jets," *AIAA Journal*, Vol. 21, No. 2, 1983, pp. 235–240.

[35] Massey, K., Ahuja, K., Jones Jr, R., and Tam, C., "Screech Tones of Supersonic Heated Free Jets," *32nd AIAA Aerospace Sciences Meeting and Exhibit,* 1994, pp. 141.

[36] Tam, C. K. W., "Supersonic Jet Noise," *Annual Review of Fluid Mechanics*, Vol. 27, No. 1, 1995, pp. 17–43.

[37] Bridges, J., and Wernet, M., "Measurements of Aeroacoustic Sound Sources in Turbulent Jets," *9th AIAA/CEAS Aeroacoustics Conference and Exhibit,* 2003, pp. 3130.

[38] Brown, C. A., and Bridges, J., "Parametric Testing of Chevrons on Single Flow Hot Jets," *10th AIAA/CEAS Aeroacoustics Conference,* 2004, pp. 2824.

[39] Viswanathan, K., "Aeroacoustics of Hot Jets," *Journal of Fluid Mechanics*, Vol. 516, 2004, pp. 39–82.

[40] Fisher, M. J., Lush, P. A., and Harper Bourne, M., "Jet Noise," *Journal of Sound Vibration*, Vol. 28, No. 3, 1973, pp. 563–585.

[41] Bridges, J., and Wernet, M., "Establishing Consensus Turbulence Statistics for Hot Subsonic Jets," *16th AIAA/CEAS Aeroacoustics Conference,* 2010, pp. 3751.

[42] Kuo, C.-W., Veltin, J., and McLaughlin, D. K., "Acoustic Assessment of Small-Scale Military-Style Nozzles with Chevrons," *Noise Control Engineering Journal*, Vol. 60, No. 5, 2012, pp. 559–576.

[43] Powers, R. W., and McLaughlin, D. K., "Acoustics Measurements of Military-Style Supersonic Beveled Nozzle Jets with Interior Corrugations," *International Journal of Aeroacoustics*, Vol. 16, Nos. 1–2, 2017, pp. 21–43.

[44] Hafsteinsson, H. E., Eriksson, L.-E., Andersson, N., Cuppoletti, D. R., and Gutmark, E., "Noise Control of Supersonic Jet with Steady and Flapping Fluidic Injection," *AIAA Journal*, Vol. 53, No. 11, 2015, pp. 3251–3272.

[45] Bennett, S. K., and Shankar, R. N., "Jet Noise Reduction in Co-Flowing Jets with Finite Lip Thickness," *International Journal of Vehicle Structures & Systems*, Vol. 12, No. 4, 2020, pp. 476–480.

[46] Daniel, K., Mayo, D. E., Lowe, K. T., and Ng, W., "Space-Time Description of the Density Near-Field in a Non-Uniformly Heated Jet," *25th AIAA/CEAS Aeroacoustics Conference,* 2019, pp. 2474.

[47] Lyu, B., Dowling, A. P., and Naqavi, I., "Prediction of Installed Jet Noise," *Journal of Fluid Mechanics*, Vol. 811, 2017, pp. 234–268.

[48] Curle, N., "The Influence of Solid Boundaries Upon Aerodynamic Sound," *Proceedings of the Royal Society of London. Series A. Mathematical and Physical Sciences*, Vol. 231, No. 1187, 1955, pp. 505–514.

[49] Phillips, O. M., "On the Generation of Sound by Supersonic Turbulent Shear Layers," *Journal of Fluid Mechanics*, Vol. 9, No. 1, 1960, pp. 1–28.

[50] Lilley, G. M., "On the Noise from Jets," *Noise Mechanism*, AGARD-CP-131, 1974, pp. 13.1-13.12.

[51] Tester, B. J., and Morfey, C. L., "Developments in Jet Noise Modelling—Theoretical Predictions and Comparisons with Measured Data," *Journal of Sound and Vibration*, Vol. 46, No. 1, 1976, pp. 79–103.

[52] Morfey, C. L., Szewczyk, V. M., and Tester, B. J., "New Scaling Laws for Hot and Cold Jet Mixing Noise Based on a Geometric Acoustics Model," *Journal of Sound and Vibration*, Vol. 61, No. 2, 1978, pp. 255–292.

[53] Tam, C. K. W., and Chen, P., "Turbulent Mixing Noise from Supersonic Jets," *AIAA journal*, Vol. 32, No. 9, 1994, pp. 1774–1780.

[54] Laufer, J., Schlinker, R., and Kaplan, R. E., "Experiments on Supersonic Jet Noise," *Aiaa Journal*, Vol. 14, No. 4, 1976, pp. 489–497.

[55] Tam, C. K. W., Viswanathan, K., Ahuja, K. K., and Panda, J., "The Sources of Jet Noise: Experimental Evidence," *Journal of Fluid Mechanics*, Vol. 615, 2008, pp. 253–292.

[56] Tam, C., Golebiowski, M., and Seiner, J., "On the Two Components of Turbulent Mixing Noise from Supersonic Jets," *2nd AIAA/CEAS Aeroacoustics Conference,* 1996, pp. 1716.

[57] Jordan, P., and Colonius, T., "Wave Packets and Turbulent Jet Noise," *Annual review of fluid mechanics*, Vol. 45, 2013, pp. 173–195.

[58] Tam, C. K. W., and Auriault, L., "Jet Mixing Noise from Fine-Scale Turbulence," *AIAA Journal*, Vol. 37, No. 2, 1999, pp. 145–153.

[59] Morris, P. J., and Farassat, F., "Acoustic Analogy and Alternative Theories for Jet Noise Prediction," *AIAA Journal*, Vol. 40, No. 4, 2002, pp. 671–680.

[60] Goldstein, M. E., "A Unified Approach to Some Recent Developments in Jet Noise Theory," *International Journal of Aeroacoustics*, Vol. 1, No. 1, 2002, pp. 1–16.

[61] Goldstein, M. E., "A Generalized Acoustic Analogy," *Journal of Fluid Mechanics*, Vol. 488, 2003, pp. 315–333.

[62] Goldstein, M. E., and Leib, S. J., "The Aeroacoustics of Slowly Diverging Supersonic Jets," *Journal of Fluid Mechanics*, Vol. 600, 2008, pp. 291–337.

[63] Karabasov, S. A., Afsar, M. Z., Hynes, T. P., Dowling, A. P., McMullan, W. A., Pokora, C. D., Page, G. J., and McGuirk, J. J., "Jet Noise: Acoustic Analogy Informed by Large Eddy Simulation," *AIAA journal*, Vol. 48, No. 7, 2010, pp. 1312–1325.

[64] Semiletov, V. A., and Karabasov, S. A., "A Volume Integral Implementation of the Goldstein Generalised Acoustic Analogy for Unsteady Flow Simulations," *Journal of Fluid Mechanics*, Vol. 853, 2018, pp. 461–487.

[65] Gryazev, V., Markesteijn, A. P., and Karabasov, S. A., "Generalized Acoustic Analogy Modeling of Hot Jet Noise," *AIAA Journal*, Vol. 60, No. 4, 2022, pp. 2383–2396.

[66] Balsa, T. F., Gliebe, P. R., Kantola, R. A., Mani, R., Stringas, E. J., and Wang, J. C. F., "High Velocity Jet Noise Source Location and Reduction," *National Technical Information Service*, Report No. R78AEG323, 1978.

[67] Schlichting, H., and Gersten, K., "Boundary-Layer Theory," 9th Edition, Springer, 2016.

[68] Khavaran, A., Krejsa, E. A., and Kim, C. M., "Computation of Supersonic Jet Mixing Noise for an Axisymmetric Convergent-Divergent Nozzle," *Journal of Aircraft*, Vol. 31, No. 3, 1994, pp. 603–609.

[69] Khavaran, A., "Role of Anisotropy in Turbulent Mixing Noise," *AIAA Journal*, Vol. 37, No. 7, 1999, pp. 832–841.

[70] Khavaran, A., and Bridges, J., "Modelling of Turbulence Generated Noise in Jets," *10th AIAA/CEAS Aeroacoustics Conference,* 2004, pp. 2983.

[71] Colonius, T., Moin, P., and Lele, S. K., "Direct Computation of Aerodynamic Sound," PhD Thesis, Stanford University, 1995.

[72] Freund, J. B., Lele, S. K., and Moin, P., "Numerical Simulation of a Mach 1.92 Turbulent Jet and Its Sound Field," *AIAA Journal*, Vol. 38, No. 11, 2000, pp. 2023–2031.

[73] Freund, J. B., "Noise Sources in a Low-Reynolds-Number Turbulent Jet at Mach 0.9," *Journal of Fluid Mechanics*, Vol. 438, 2001, pp. 277–305.

[74] Gamet, L., and Estivalezes, J. L., "Application of Large-Eddy Simulations and Kirchhoff Method to Jet Noise Prediction," *AIAA Journal*, Vol. 36, No. 12, 1998, pp. 2170–2178.

[75] Mankbadi, R. R., Hayer, M. E., and Povinelli, L. A., "Structure of Supersonic Jet Flow and Its Radiated Sound," *AIAA Journal*, Vol. 32, No. 5, 1994, pp. 897–906.

[76] Arunajatesan, S., and Sinha, N., "Hybrid RANS-LES Modeling for Cavity Aeroacoustics Predictions," *International Journal of Aeroacoustics*, Vol. 2, No. 1, 2003, pp. 65–93.

[77] Bodony, D. J., and Lele, K. S., "Current Status of Jet Noise Predictions Using Large-Eddy Simulation," *AIAA Journal*, Vol. 46, No. 2, 2008, pp. 364–380.

[78] Bres, G. A., and Lele, K. S., "Modelling of Jet Noise: A Perspective from Large-Eddy Simulations," *Philosophical Transactions*, Vol. 377, No. 2159, 2019.

[79] Shur, M. L., Spalart, P. R., and Strelets, M. K., "Noise Prediction for Increasingly Complex Jets. Part I: Methods and Tests," *International Journal of Aeroacoustics*, Vol. 4, No. 3, 2005, pp. 213–245.

[80] Shur, M. L., Spalart, P. R., and Strelets, M. K., "Noise Prediction for Increasingly Complex Jets. Part II: Applications," *International Journal of Aeroacoustics*, Vol. 4, No. 3, 2005, pp. 247–266.

[81] Lew, P.-T., Uzun, A., Blaisdell, G., and Lyrintzis, A., "Effects of Inflow Forcing on Jet Noise Using Large Eddy Simulation," *42nd AIAA Aerospace Sciences Meeting and Exhibit,* 2004, pp. 516.

[82] Bodony, D. J., and Lele, S. K., "On Using Large-Eddy Simulation for the Prediction of Noise from Cold and Heated Turbulent Jets," *Physics of Fluids*, Vol. 17, No. 8, 2005.

[83] Crighton, D. G., "Acoustics as a Branch of Fluid Mechanics," *Journal of Fluid Mechanics*, Vol. 106, 1981, pp. 261–298.

[84] Armstrong, C. G., Fogg, H. J., Tierney, C. M., and Robinson, T. T., "Common Themes in Multi-Block Structured Quad/Hex Mesh Generation," *Procedia Engineering*, Vol. 124, 2015, pp. 70–82.

[85] Coirier, W. J., and Powell, K. G., "An Accuracy Assessment of Cartesian-Mesh Approaches for the Euler Equations," *Journal of Computational Physics*, Vol. 117, No. 1, 1995, pp. 121–131.

[86] Chan, W. M., "Overset Grid Technology Development at NASA Ames Research Center," *Computers & Fluids*, Vol. 38, No. 3, 2009, pp. 496–503.

[87] Spekreijse, S., Prananta, B. B., and Kok, J. C., "A Simple, Robust and Fast Algorithm to Compute Deformations of Multi-Block Structured Grids," *National Aerospace Laboratory NLR,* 2002.

[88] Abalakin, I., Bakhvalov, P., and Kozubskaya, T., "Edge-Based Reconstruction Schemes for Unstructured Tetrahedral Meshes," *International Journal for Numerical Methods in Fluids*, Vol. 81, No. 6, 2016, pp. 331–356.

[89] Brès, G. A., Ham, F. E., Nichols, J. W., and Lele, S. K., "Unstructured Large-Eddy Simulations of Supersonic Jets," *AIAA Journal*, Vol. 55, No. 4, 2017, pp. 1164–1184.

[90] Shur, M. L., Spalart, P. R., and Strelets, M. K., "Jet Noise Computation Based on Enhanced DES Formulations Accelerating the RANS-to-LES Transition in Free Shear Layers," *International Journal of Aeroacoustics*, Vol. 15, Nos. 6–7, 2016, pp. 595–613.

[91] Bogey, C., and Bailly, C., "Effects of Inflow Conditions and Forcing on Subsonic Jet Flows and Noise.," *AIAA Journal*, Vol. 43, No. 5, 2005, pp. 1000–1007.

[92] Bogey, C., and Bailly, C., "Influence of Nozzle-Exit Boundary-Layer Conditions on the Flow and Acoustic Fields of Initially Laminar Jets," *Journal of Fluid Mechanics*, Vol. 663, 2010, pp. 507–538.

[93] Bogey, C., Marsden, O., and Bailly, C., "Influence of Initial Turbulence Level on the Flow and Sound Fields of a Subsonic Jet at a Diameter-Based Reynolds Number of 105," *Journal of Fluid Mechanics*, Vol. 701, 2012, pp. 352–385.

[94] Lorteau, M., Cléro, F., and Vuillot, F., "Analysis of Noise Radiation Mechanisms in Hot Subsonic Jet from a Validated Large Eddy Simulation Solution," *Physics of Fluids*, Vol. 27, No. 7, 2015.

[95] Zhu, M., Arroyo, C. P., Pouangué, A. F., Sanjosé, M., and Moreau, S., "Isothermal and Heated Subsonic Jet Noise Using Large Eddy Simulations on Unstructured Grids," *Computers & Fluids*, Vol. 171, 2018, pp. 166–192.

[96] Brès, G. A., Jordan, P., Jaunet, V., Le Rallic, M., Cavalieri, A. V. G., Towne, A., Lele, S. K., Colonius, T., and Schmidt, O. T., "Importance of the Nozzle-Exit Boundary-Layer State in Subsonic Turbulent Jets," *Journal of Fluid Mechanics*, Vol. 851, 2018, pp. 83–124.

[97] Bodart, J., and Larsson, J., "Wall-Modeled Large Eddy Simulation in Complex Geometries with Application to High-Lift Devices," *Annual Research Briefs, Center for Turbulence Research, Stanford University*, 2011, pp. 37–48.

[98] Piomelli, U., and Balaras, E., "Wall-Layer Models for Large-Eddy Simulations," *Annual Review of Fluid Mechanics*, Vol. 34, No. 1, 2002, pp. 349–374.

[99] Ffowcs Williams, J. E., and Hawkings, D. L., "Sound Generation by Turbulence and Surfaces in Arbitrary Motion," *Philosophical Transactions of the Royal Society of London. Series A, Mathematical and Physical Sciences*, Vol. 264, No. 1151, 1969, pp. 321–342.

[100] Langenais, A., Vuillot, F., Troyes, J., and Bailly, C., "Accurate Simulation of the Noise Generated by a Hot Supersonic Jet Including Turbulence Tripping and Nonlinear Acoustic Propagation," *Physics of Fluids*, Vol. 31, No. 1, 2019.

[101] Mendez, S., Shoeybi, M., Lele, S. K., and Moin, P., "On the Use of the Ffowcs Williams-Hawkings Equation to Predict Far-Field Jet Noise from Large-Eddy Simulations," *International Journal of Aeroacoustics*, Vol. 12, No. 1+2, 2013, pp. 1–20.

[102] Goc, K. A., Lehmkuhl, O., Park, G. I., Bose, S. T., and Moin, P., "Large Eddy Simulation of Aircraft at Affordable Cost: A Milestone in Computational Fluid Dynamics," *Flow*, Vol. 1, 2021, p. E14.

[103] Brès, G. A., Bose, S. T., Ivey, C. B., Emory, M., and Ham, F., "GPU-Accelerated Large-Eddy Simulations of Supersonic Jets from Twin Rectangular Nozzle," *28th AIAA/CEAS Aeroacoustics Conference,* 2022, pp. 3001.

[104] Nichols, J. W., Lele, S. K., Ham, F. E., Martens, S., and Spyropoulos, J. T., "Crackle Noise in Heated Supersonic Jets," *Turbo Expo: Power for Land, Sea, and Air,* 2012, pp. 337–345.

[105] Nichols, J. W., Lele, S. K., and Spyropoulos, J. T., "The Source of Crackle Noise in Heated Supersonic Jets," *19th AIAA/CEAS Aeroacoustics Conference,* 2013, pp. 2197.

[106] Smagorinsky, J., "General Circulation Experiments with the Primitive Equations: Part I, The Basic Experiment," *Monthly Weather Review*, Vol. 91, No. 3, 1963, pp. 99–164.

[107] Nicoud, F., and Ducros, F., "Subgrid-Scale Stress Modelling Based on the Square of the Velocity Gradient Tensor," *Flow, Turbulence and Combustion*, Vol. 62, 1999, pp. 183–200.

[108] Bae, H. J., "Investigation of Dynamic Subgrid-Scale and Wall Models for Turbulent Boundary Layers," PhD Thesis, Stanford University, 2018.

[109] Bogey, C., Bailly, C., and Juvé, D., "Computation of Flow Noise Using Source Terms in Linearized Euler's Equations," *AIAA Journal*, Vol. 40, No. 2, 2002, pp. 235–243.

[110] Towne, A., Cavalieri, A. V. G., Jordan, P., Colonius, T., Schmidt, O., Jaunet, V., and Brès, G. A., "Acoustic Resonance in the Potential Core of Subsonic Jets," *Journal of Fluid Mechanics*, Vol. 825, 2017, pp. 1113–1152.

[111] Schmidt, O. T., Towne, A., Colonius, T., Cavalieri, A. V. G., Jordan, P., and Brès, G. A., "Wavepackets and Trapped Acoustic Modes in a Turbulent Jet: Coherent Structure Eduction and Global Stability," *Journal of Fluid Mechanics*, Vol. 825, 2017, pp. 1153–1181.

[112] Bodony, D., and Lele, S., "Spatial Scale Decomposition of Shear Layer Turbulence and the Sound Sources Associated with the Missing Scales in a Large-Eddy Simulation," *8th AIAA/CEAS Aeroacoustics Conference and Exhibit,* 2002, pp. 2454.

[113] Bodony, D., and Lele, S., "A Statistical Subgrid Scale Noise Model: Formulation," *9th AIAA/CEAS Aeroacoustics Conference and Exhibit,* 2003, pp. 3252.

[114] Ghate, A. S., and Lele, S. K., "Subfilter-Scale Enrichment of Planetary Boundary Layer Large Eddy Simulation Using Discrete Fourier--Gabor Modes," *Journal of Fluid Mechanics*, Vol. 819, 2017, pp. 494–539.

[115] Bechara, W., Bailly, C., Lafon, P., and Candel, S. M., "Stochastic Approach to Noise Modeling for Free Turbulent Flows," *AIAA Journal*, Vol. 32, No. 3, 1994, pp. 455–463.

[116] Ewert, R., Dierke, J., Siebert, J., Neifeld, A., Appel, C., Siefert, M., and Kornow, O., "CAA Broadband Noise Prediction for Aeroacoustic Design," *Journal of Sound and Vibration*, Vol. 330, No. 17, 2011, pp. 4139–4160.

[117] Favre, A. J., *The Equations of Compressible Turbulent Gases*, PN, 1965.

[118] Favre, A. J., "Statistical Equations of Turbulent Gases," *Problems of Hydrodynamics and Continuum Mechanics*, 1969, pp. 231–266.

[119] Alfonsi, G., "Reynolds-Averaged Navier--Stokes Equations for Turbulence Modeling," *Applied Mechanics Reviews*, Vol. 62, No. 4, 2009.

[120] Leonard, B. P., "Simple High-Accuracy Resolution Program for Convective Modelling of Discontinuities," *International Journal for Numerical Methods in Fluids*, Vol. 8, No. 10, 1988, pp. 1291–1318.

[121] Spalart, P., and Allmaras, S., "A One-Equation Turbulence Model for Aerodynamic Flows," *30th Aerospace Sciences Meeting and Exhibit,* 1992, pp. 439.

[122] Launder, B. E., and Spalding, D. B., "The Numerical Computation of Turbulent Flows," *Numerical Prediction of Flow, Heat Transfer, Turbulence and Combustion*, Pergamon, 1983, pp. 96–116.

[123] Wilcox, D. C., and others, "Turbulence Modeling for CFD," *DCW industries, La Canada*, 1998.

[124] Gibson, M. M., and Launder, B. E., "Ground Effects on Pressure Fluctuations in the Atmospheric Boundary Layer," *Journal of Fluid Mechanics*, Vol. 86, No. 3, 1978, pp. 491–511.

[125] Duffal, V., de Laage de Meux, B., and Manceau, R., "Development and Validation of a Hybrid RANS-LES Approach Based on Temporal Filtering," Vol. 59032, 2019, pp. V002T02A053.

[126] Rodi, W., "Experience with Two-Layer Models Combining the k-Epsilon Model with a One-Equation Model near the Wall," 1991.

[127] Davidson, L., Nielsen, P. V., and Sveningsson, A., "Modifications of the V2 Model for Computing the Flow in a 3D Wall Jet," *International Symposium on Turbulence, Heat and Mass Transfer,* 2003, pp. 577-584.

[128] Menter, F. R., "Two-Equation Eddy-Viscosity Turbulence Modeling for Engineering Applications," *AIAA Journal*, Vol. 32, No. 8, 1994, pp. 1598–1605.

[129] Brentner, K. S., and Farassat, F., "Analytical Comparison of the Acoustic Analogy and Kirchhoff Formulation for Moving Surfaces," *AIAA journal*, Vol. 36, No. 8, 1998, pp. 1379–1386.

[130] Richardson, L. F., "Weather Prediction by Numerical Process," University Press, 1922.

[131] Kolmogorov, A. N., "The Local Structure of Turbulence in Incompressible Viscous Fluid for Very Large Reynolds," *Numbers. In Dokl. Akad. Nauk SSSR*, Vol. 30, 1941, p. 301.

[132] Pope, S. B., "Turbulent Flows," Cambridge University Press, 2001.

[133] Van Driest, E. R., "On Turbulent Flow near a Wall," *Journal of the Aeronautical Sceinces*, Vol. 23, No. 11, 1956, pp. 1007–1011.

[134] Husted, B., "Turbulent Mixing in the Lower Part of the Smoke Layer Using the Fire Dynamic Simulator," *1st International Symposium Knowledge for Resilient Society K-FORCE,* 2017, pp. 213-310.

[135] Kim, J., and Choi, H., "Effect of the Initial Momentum Thickness on the Acoustic Source in an Incompressible Round Jet," *10th AIAA/CEAS Aeroacoustics Conference,* 2004, pp. 2949.

[136] Junqueira-Junior, C., Yamouni, S., Azevedo, J. L. F., and Wolf, W. R., "Influence of Different Subgrid-Scale Models in Low-Order LES of Supersonic Jet Flows," *Journal of the Brazilian Society of Mechanical Sciences and Engineering*, Vol. 40, 2018, pp. 1–29.

[137] Tkatchenko, I., Kornev, N., Jahnke, S., Steffen, G., and Hassel, E., "Performances of LES and RANS Models for Simulation of Complex Flows in a Coaxial Jet Mixer," *Flow, turbulence and combustion*, Vol. 78, 2007, pp. 111–127.

[138] Brès, G. A., Ham, F., Nichols, J. W., and Lele, S. K., "Nozzle Wall Modeling in Unstructured Large Eddy Simulations for Hot Supersonic Jet Predictions," *19th AIAA/CEAS Aeroacoustics Conference*, 2013, pp. 2142.

[139] Wu, X., "Inflow Turbulence Generation Methods," *Annual Review of Fluid Mechanics*, Vol. 49, No. 1, 2017, pp. 23–49.

[140] Jarrin, N., Prosser, R., Uribe, J.-C., Benhamadouche, S., and Laurence, D., "Reconstruction of Turbulent Fluctuations for Hybrid RANS/LES Simulations Using a Synthetic-Eddy Method," *International Journal of Heat and Fluid Flow*, Vol. 30, No. 3, 2009, pp. 435–442.

[141] Boldman, D. R., and Brinich, P. F., "Mean Velocity, Turbulence Intensity, and Scale in a Subsonic Turbulent Jet Impinging Normal to a Large Flat Plate," NASA Technical Paper 1037, 1977.

[142] JPL, "Acoustic Noise Requirement," Lesson No. 787, based on NASA Technical Memorandum 4322A, 1999.

[143] Henderson, B., and Bridges, J., "An MDOE Investigation of Chevrons for Supersonic Jet Noise Reduction," *16th AIAA/CEAS Aeroacoustics Conference,* 2010, pp. 3926.

[144] Greska, B., Krothapalli, A., Seiner, J., Jansen, B., and Ukeiley, L., "The Effects of Microjet Injection on an F404 Jet Engine," *11th AIAA/CEAS Aeroacoustics Conference,* 2005, pp. 3047.

[145] Mengle, V., "Optimization of Lobe Mixer Geometry and Nozzle Length for Minimum Jet Noise," *6th AIAA/CEAS Aeroacoustics Conference and Exhibit,* 2000, pp. 1963.

[146] Tam, C. K. W., and Zaman, K., "Subsonic Jet Noise from Nonaxisymmetric and Tabbed Nozzles," *AIAA Journal*, Vol. 38, No. 4, 2000, pp. 592–599.

[147] Viswanathan, K., and Czech, M. J., "Role of Jet Temperature in Correlating Jet Noise," *AIAA Journal*, Vol. 47, No. 5, 2009, pp. 1090–1106.

[148] Crouch, R. W., Coughlin, C. L., and Paynter, G. C., "Nozzle Exit Flow Profile Shaping for Jet Noise Reduction," *Journal of Aircraft*, Vol. 14, No. 9, 1977, pp. 860–867.

[149] Tanna, H. K., "Coannular Jets—Are They Really Quiet and Why?," *Journal of Sound and Vibration*, Vol. 72, No. 1, 1980, pp. 97–118.

[150] Viswanathan, K., "Aeroacoustics of Hot Jets," *Journal of Fluid Mechanics*, Vol. 516, 2004, pp. 39–82.

[151] Viswanathan, K., "Scaling Laws and a Method for Identifying Components of Jet Noise," *AIAA Journal*, Vol. 44, No. 10, 2006, pp. 2274–2285.

[152] Viswanathan, K., "Does a Model-Scale Nozzle Emit the Same Jet Noise as a Jet Engine?," *AIAA Journal*, Vol. 46, No. 2, 2008, pp. 336–355.